Imperial College London

The Imperial College of Science, Technology and Medicine
Department of Physics

Buffer gas cooling of YbF molecules

Sarah Margaretha Skoff

Submitted in partial fulfilment of the requirements for the degree of
Doctor of Philosophy in Physics of Imperial College, London,
September 2011

Declaration

I declare that this thesis is my own work. Where I have used the work of others the sources are appropriately referenced and acknowledged.

Citations to previously published work

Parts of this thesis have been published in the following articles:

S. M. Skoff, R. J. Hendricks, C. D. J. Sinclair, M. R. Tarbutt, J. J. Hudson, D. M. Segal, B. E. Sauer and E. A. Hinds, Doppler-free laser spectroscopy of buffer-gas-cooled molecular radicals, *New Journal of Physics*, **11**, 12302, (2009)

S. M. Skoff, R. J. Hendricks, C. D. J. Sinclair, J. J. Hudson, D. M. Segal, B. E. Sauer, E. A. Hinds and M. R. Tarbutt, Diffusion, thermalization, and optical pumping of YbF molecules in a cold buffer-gas cell, *Physical Review A*, **83**, 023418, (2011)

Abstract

This thesis reports on the production and characterisation of the first slow and cold beam of YbF molecules using buffer gas cooling. These molecules are being used to measure the electron's electric dipole moment, and an intense source of slow-moving molecules is desirable for this experiment. The molecules are loaded into a buffer gas cell via laser ablation where they thermalise with cold helium buffer gas. They are then detected inside the cell using laser absorption imaging and spectroscopy on the $X^2\Sigma^+ \rightarrow A^2\Pi_{1/2}$ transition. The formation, diffusion and thermalisation dynamics of the molecules inside the cell are studied. Measurements of laser absorption versus intensity reveal that saturation of the absorption is due to a competition between optical pumping into dark states and repopulation of the addressed level by inelastic and velocity-changing collisions.

A beam of YbF molecules is extracted through an aperture in the buffer gas cell and characterised using laser induced fluorescence detection. Peak fluxes of 10^{10} molecules per steradian per pulse, in the rotational and vibrational ground state, are obtained. The translational and rotational temperatures are in equilibrium with the cell temperature of 4 K. The forward velocity of the pulses can be varied between 130 m/s and 200 m/s by changing the buffer gas pressure. This source is an order of magnitude brighter and more than three times slower than a supersonic source of YbF molecules and provides an excellent starting point for improving the measurement of the electron's electric dipole moment and for deceleration and trapping experiments.

In order to reduce the helium load on the vacuum system and to shorten the molecular pulses, a second set-up, delivering the buffer gas into an open copper cylinder in pulses rather than in a continuous flow,is characterised and shows promising first results.

Acknowledgements

The work described in this thesis would not have been possible without the support and help of many people. First of all I want to thank Ed Hinds, Mike Tarbutt, Ben Sauer and Danny Segal for their guidance during my PhD and for making it the fulfilling and fun experience that it was. They have been great teachers and I have learned a lot from them. I especially want to thank Mike for his support and for his time and patience in explaining yet another thing to me. I shall thank Chris for introducing me to the buffer gas project and the bay 3 gang for a great one and a half years in a lab with very good music and sometimes bad jokes. None of this work would have been possible without the combined forces of the buffer gas team (Go Bg go!). I want to thank Rich for being my post-doc and Rich and Nick for many fruitful discussions. They have been great colleagues to work with and have become good friends.

At this point I want to thank all members of CCM and of course the Ion Trapping gang for being such an interesting bunch of people, be it discussing physics or talking just about anything else.

I want to thank Jon Dyne and Steve Maine from the workshop for all their work on the molecular beam apparatus and a lot of other things essential to the experiment. Thanks also to Sanja Maricic.

I want to thank my parents for their encouragement and for supporting me in what I do. I also want to say a huge thank you to my friends back home, especially to Min, who although sometimes a bit far away, have always shown me that I can count on them and have played a big part in keeping me sane whilst writing. Thanks to my flatmates in West Ken for never minding my nightly writing and for making a horrible flat enjoyable to live in. Among many things, I want to thank Bernhard especially for his support and for taking so much interest in what I do.

Contents

1 Introduction **9**

1.1 Cold molecules . . . 9

1.1.1 From hot to cold . . . 10

1.2 A short history of molecular beams . . . 11

1.3 Buffer gas cooling of YbF molecules . . . 14

2 Experimental Set-up I **16**

2.1 The Buffer Gas Apparatus . . . 16

2.2 The YbF Source . . . 18

2.2.1 Helium pressure inside the buffer gas cell . . . 19

2.3 Absorption detection set-up . . . 22

2.3.1 Computer Control . . . 24

2.3.2 Frequency Monitoring . . . 24

3 Absorption spectroscopy of YbF **26**

3.1 YbF energy-level structure . . . 26

3.2 Absorption Spectroscopy . . . 29

3.3 Absorption and saturated absorption spectroscopy of YbF . . . 32

3.3.1 Results . . . 33

3.4 Saturation of absorption in a buffer gas cell . . . 35

3.5 Collisional cross-section measurements of YbF . . . 39

3.5.1 Results . . . 39

3.6 Conclusion . . . 42

4 Buffer Gas Cooling of YbF **44**

4.1 Cooling in a buffer gas cell . . . 44

4.2 Diffusion in a buffer gas cell . . . 46

4.3 The diffusion cross-section . . . 47

4.3.1 Calculation of Li-He diffusion cross-section . . . 50

4.3.2 Calculation of YbF-He diffusion cross-section . . . 51

4.4 Measurements of the YbF-He diffusion cross-section . . . 52

4.4.1 Results . . . 53

4.5 Absorption Images . . . 56
4.5.1 Results . . . 56
4.6 Simulating diffusion in our buffer gas cell . . . 57
4.6.1 Results . . . 58
4.7 Temperature Measurements . . . 61
4.7.1 Results . . . 62
4.8 Summary and conclusions . . . 67

5 Experimental Set-up II **70**
5.1 The Buffer Gas Molecular Beam Apparatus . . . 70
5.1.1 The buffer gas cell . . . 72
5.1.2 Helium pressure and maintaining good guard vacuum . . . 73
5.2 The Probe Laser Systems . . . 74
5.2.1 Frequency Doubling . . . 74
5.2.2 Doubling Cavity . . . 76
5.2.3 Periodically poled crystal set-up . . . 77
5.3 Absorption Detection and Fluorescence Detection Set-up . . . 77
5.3.1 Fluorescence detection efficiency . . . 78

6 A cold and slow beam of YbF molecules **82**
6.1 Flow and extraction efficiency of a buffer gas cell . . . 82
6.2 Measuring beam parameters of a YbF buffer gas beam . . . 85
6.2.1 Optimisation and measurements of beam flux . . . 85
6.2.2 Centre of mass velocity and translational temperature . . . 89
6.2.3 Rotational Temperature Measurements . . . 92
6.2.4 Optical pumping measurements . . . 94
6.2.5 Beam flux with and without a skimmer . . . 97
6.3 Characterising a YbF buffer gas beam with a pulsed helium source . . . 98
6.3.1 Calibrating the amount of helium emitted by the pulsed valve . . . 100
6.3.2 Optimising the beam flux . . . 101
6.4 Conclusion . . . 104

7 Conclusion and Outlook **106**
7.1 Measurements inside a closed buffer gas cell . . . 106
7.2 Producing a cold beam of YbF molecules . . . 107
7.3 Outlook . . . 108
7.3.1 Improvements to and variations of the source of cold molecules . . . 108
7.3.2 Guiding and trapping of molecules . . . 110

A Rotational line strengths **113**

B Flow Regimes **117**

B.1 Effusive Regime 118

B.2 Supersonic Regime 120

B.2.1 The effect of gas reservoir to background pressure ratio on the flow . 126

Bibliography **133**

List of Figures **143**

List of Tables **147**

Chapter 1

Introduction

1.1 Cold molecules

As the cooling and trapping of atoms has led to the exploration of quantum gases , e.g. Bose Einstein condensates (BEC) [1], similar goals have been sought for molecules. Molecules are a lot harder to cool than atoms, for which laser cooling is used. Laser cooling only works for atoms that have a closed absorption and emission cycle and therefore is generally not applicable for molecules that usually have a much more complicated internal structure. This richer internal structure is also what makes them more interesting than atoms. They have additional rotational and vibrational degrees of freedom that atoms do not have and can also carry electric dipole moments. Because of these large dipole moments, molecules interact far more strongly with applied electric fields than atoms, and electric fields can be used to manipulate molecular motion.

By cooling molecules to lower temperatures, they move more slowly allowing the observation time to be increased. An example of this was shown by van Veldhoven et al.[2], where ND_3 molecules were slowed down making it possible to resolve its hyperfine structure. Some molecules such as ND_3 [3] and some diatomic hydrides [4] are good candidates for measuring a possible change in the electron to proton mass ratio. A longer observation time leads to increased sensitivity for such precision measurements. Slow molecules present a perfect system to test physics beyond the standard model. Time reversal symmetry can be tested by searching for the electron's electric dipole moment and the most precise measurement of this quantity is now given by an experiment using a beam of fast moving YbF molecules [5]. A slower beam of these molecules would allow for great increase in the precision of this measurement. This experiment as well as molecular beam experiments for measuring parity violation in chiral molecules [6] and in nuclei [7] provide a table top alternative to collision experiments in huge particle accelerators.

As molecules are cooled to lower temperatures, it becomes possible to load them into traps. Taking advantage of their magnetic and electric dipole moments these can be magnetic traps [8],[9] or electric traps [10], [11], [12] but it is also possible to trap them in optical lattices [13] and microwave traps have been proposed[14]. Having molecules in traps

provides a variety of exciting fields of research. For the first time it was possible to measure radiative decay times of long-lived vibrational states [15], [16] and other metastable states. Being able to trap molecules provides the opportunity to cool them down further by means of sympathetic cooling [17, 18, 19, 20] or if a high enough density is achieved even evaporative cooling. This makes it possible to investigate the field of ultracold chemistry, where quantum mechanical tunneling becomes an important reaction mechanism [21]. At very low temperatures and high densities, the deBroglie wavelength becomes comparable or bigger than the interparticle separation, and then new behaviour of matter such as Bose Einstein condensates structured by electric dipole-dipole interaction [22], [23] can be studied. Molecules in traps have also been proposed as candidates for the implementation of quantum computation,e.g. [24]and [25]. Recent reviews on the formation and applications of cold molecules can be found in [26], [27].

1.1.1 From hot to cold

The features that make molecules more interesting also make it more difficult to cool them to the required temperatures to study any of the phenomena described above. The first breakthroughs were made in 1998, when CaH was cooled by a helium buffer gas and subsequently magnetically trapped [8], [9]. After that the first bi-alkali molecules were produced from laser cooled atoms via photoassociation [28]. While the first method is termed "direct" as hot molecules are slowed and cooled, the latter is known as an "indirect" method, where pre-cooled atoms are used to form cold molecules. In photoassociation two colliding atoms are excited to a bound molecular state by using a laser with an appropriate wavelength. Another indirect way to create ultracold molecules is by using a Feshbach resonance [29]. This is an enhancement in the scattering amplitude if two colliding particles have a total energy similar to that needed to create a quasi-bound state. If two ultracold atoms collide in that way, they can form a molecule for some time. If the constituents have different magnetic moments, their relative energies can be tuned by applying a magnetic field, making it possible to traverse the Feshbach resonance [30]. These indirect methods are not only restricted to certain molecules but also create them in vibrationally excited states. Still by using Feshbach resonances, it has been possible to observe the first molecular BECs[31],[32],[33]. Recently, several groups have shown how ultracold molecules produced in states near the dissociation limit by photoassociation or through a Feshbach resonance can be transfered to strongly-bound states using laser-stimulated state transfer processes [34], [35], [36].

Direct methods can be applied to a larger variety of molecules. For example buffer gas cooling is applicable to any molecule of interest as it works by cooling the molecular species through collisions with a cold buffer gas. It was pioneered by Jon Doyle's group in Harvard [8], [37], and has since been used to cool and trap a wide variety of species, e.g. [38], [39]. As it works in a cryogenic environment it can be naturally combined with magnetic trapping using superconducting magnets.

Another way of decelerating molecules from a cold source is Stark deceleration [40]. Molecules, usually from supersonic sources, which leave them cold but fast, are sent through time dependent inhomogeneous electric fields. The energy levels of polar molecules get shifted up or down when experiencing an electric field, depending on whether they are low or high field seeking. In the case of low field seeking molecules as they enter a region of high field, their potential energy is raised and thus the kinetic energy decreased. If the field is switched off quickly at that point, the molecules cannot regain the kinetic energy and are slowed. If this process is repeated sufficiently often, the molecule's forward velocity can be appreciably decreased and it is possible to load them into a trap [11, 15, 41]. A way to increase the electric dipole moment and thereby decrease the number of cooling stages needed is to prepare molecules in a Rydberg state [42]. Similarly pulsed magnetic fields [43] can be used to decelerate molecules that have a magnetic moment. However the stopping distance for these methods is usually between 10 cm and several meters. By using the polarisability of molecules rather than the electric or magnetic dipole moment, the stopping distance can be reduced to a few μm by using optical Stark deceleration. For this purpose the molecules are confined in a travelling optical lattice, the velocity of which is chirped and provides a decelerating force for the particles [44, 45, 46, 47].
As supersonic sources provide cold but fast molecules, the molecules can be brought to rest in the lab frame by a rotating nozzle [48]. Low velocities in the laboratory frame can also be achieved by collisions between two crossed beams, as demonstrated by Elioff et al. [49] using a NO and an Argon beam. If instead of using a supersonic source, an effusive beam of molecules is used, the distribution can be described by a Maxwell-Boltzmann distribution. This means that there are always some slow molecules and hence this slow tail can be filtered out by using electric or magnetic guides [50]. It has been proposed [51] that molecules with a favorable Franck Condon factor can be directly laser cooled and this has now been demonstrated for SrF molecules[52].
The starting point for all these direct methods are molecular sources, which is the focus of this thesis. The remainder of this chapter will introduce the advances in molecular beams from hot effusive beams to supersonic beams and then to cold buffer gas beams.

1.2 A short history of molecular beams

At the beginning of molecular beam research stands the development of vacuum pumps that made it possible to sufficiently evacuate a chamber, so that the mean free path of the particles in the beam would be bigger than the aperture of the apparatus. In 1911, Dunoyer then created the first atomic beam of sodium atoms by letting them escape from a narrow cylinder into a highly evacuated chamber. Obtaining a beam of neutral not interacting particles with thermal velocities moving in a given direction opened up a tool to investigate many open questions about the kinetic theory of gases, atomic physics, gas surface interactions, collision dynamics and chemical reactions. From then on these molecular beams were widely used and led to many important results for example the first experi-

mental measurement of the Maxwellian speed distribution by Otto Stern in 1920 or the spin quantisation in atoms by Otto Stern and Walther Gerlach [53].
Effusive beams consist of a source chamber that houses an oven which evaporates the desired species and has an aperture [1] from where the particles can escape [54]. The velocity of these beams was commonly measured and selected by putting rotating disks into the beam path. In attempts to create narrow beams, baffles were put into the beam line [55]. However in these sources, the maximum attainable intensity is limited by the effusion rate through the first slit. Just turning up the oven temperature and thereby creating a higher density of molecules inside the source chamber, was experimentally found to lead to effects of diminished beam density [56]. From these observations, a rule of thumb emerged which suggested the ideal beam intensity was obtained if the mean free path in the source chamber was similar to the width of the slit, the molecules effused from.
In 1951, Kantrowitz and Grey [57] proposed that by letting gas expand through a nozzle [2] rather than by effusion through a simple aperture, it should be possible to create a molecular beam of higher intensity and lower divergence. They suggested that the velocity distribution would be narrower and peaked around a velocity higher than that of an effusive beams. Kistiakowsky and Slichter [58] were the first to set the proposal of accelerating the gas to supersonic velocities into practice. To switch from an oven source to a nozzle source they had to use a gas with a low boiling point so that they could just connect a gas inlet to the nozzle. They used ammonia and showed in first experiments, that the beam intensity could be enhanced by a factor of more than 20 and that when changing the gas pressure behind the nozzle, the intensity grew far more rapidly than the inlet pressure. In order to achieve supersonic flow, a large initial pressure ratio is needed. They ran the experiment with a continuous gas flow, where a supersonic flow was maintained for 30 s. To help achieve the inital pressure gradient, a valve was installed in the supply line, that was able to rapidly open. Similar experiments were also conducted by Becker et al. [59] and by Deckers et al. [60]. A limiting factor in their experiments was the pumping speed of their vacuum pumps. It was further improvements in the technology of vacuum pumps that made advances and study of these supersonic beams possible. In the late 1950 s and late 1960 a focus lay on better valve design and with valves that were able to open and close very quickly; the pulsed supersonic source was born [61], [62]. This reduced the high pumping requirements needed for the continuous sources and made it possible to measure the velocity distribution via time of flight methods as already proposed by Knauer et al. [54] for effusive beams. After studying and characterising nozzle sources, people sought to increase the range of species that could be used. So far the choice was restricted by using gases with a low enough boiling point that a high enough backing pressure could be achieved. In the 1970 s and 1980 s different ways of creating atomic and molecular sources were developed. Very early on, sources of metastable atoms were created by a discharge,

[1] The term aperture is usually used for openings in a wall of the chamber that is thin, however it can also be used for channels.

[2] The term nozzle usually refers to a channel with varying cross-section in the direction of beam propagation, such as the convergent-divergent de Laval nozzle

where the anode was a needle inside the nozzle and the skimmer represented the cathode. In that way metastable atoms such as helium [63], argon and neon [64] were produced. It was also noticed that instead of using a significant pressure of the desired gas species, a beam of molecules could be created by seeding a carrier gas with the species of interest. This has the result that the forward velocity of the usual heavier molecules is accelerated to that of the lighter carrier gas. Beams of potassium and rubidium [65] and many more species were produced by diluting the vapour in rare gases. This made it necessary to combine oven sources with a supersonic nozzle [66]. Where high enough temperatures could be reached, molecular beams as well as atomic beams could be produced via thermal disscociation, such as Valentini et al. did in 1976 creating beams of chlorine, bromine and iodine molecules and atoms [67]. Other ways of creating atomic beams included arc heated nozzle beams [68] or heating the gas by an electric discharge [69]. Another way of seeding supersonic beams was used in 1988 by Li et al. [70], when they used laser desorption of molecules suspended in a glycerol matrix to create molecular beams. Laser ablation has since not only been used for supersonic sources [71], but also for loading atoms and molecules into a buffer gas cell [8], [72]. In the 1960 s, when people started building their own gas valves, they also tried cooling them and thereby the field of cluster beams emerged [59]. However, apart from condensing into clusters of various sizes, cooling a supersonic valve also results in beams with lower energy as used by Kern in 1985 [73]. He noticed an optimimum in speed ratio (forward velocity to FWHM of velocity distribution) before clustering set in which heated the gas up, restricting a further increase in speed ratio. Apart from creating their own valves, people also started to adapt commercially available valves [74] to suit lower temperatures [75] or open more rapidly [71]. The detection and characterisation of molecular beams at these times had been greatly improved by the development of the laser in the 1960 s.

Although when supersonic beam research started in the 1950 s, the narrow velocity distribution and even the high forward velocity was favorable for some applications, as the field of cold molecules emerged, the need to produce cold as well as slow molecules grew (sec. 1.1). When in 1998 CaH was trapped by using buffergas cooling, the first step towards a new method to create molecular beams was born. The first cryogenic buffer gas beams were created in 2005 when sodium and PbO were loaded into a buffer gas cell via laser ablation. The cell was anchored to a cold plate of a liquid helium cryostat and the beams were extracted through a circular aperture in the buffer gas cell. The resulting forward velocities were much lower than those observed in supersonic beams [76],ranging between effusive velocities of the species of interest and the helium buffer gas, and the obtained fluxes were higher. This source was improved by using a two-stage aperture [77]. Using only the first aperture, which was chosen to be fairly large, gave a high flux beam with elevated forward velocities due to hydrodynamic effects, however still well below the hydrodynamic limit of helium. By putting a second aperture after the first one, which consisted of a fine mesh, the forward boost of the molecules was eliminated and a near-effusive beam was obtained with the compromise of a reduced flux. With this set-up Yb as well as O_2 beams were produced,

and the molecular oxygen beam was coupled into a permanent magnetic octupole guide to transfer the molecules from cold temperatures to room temperature and separate them fom the buffer gas. Further variations of the two stage aperture were investigated to create a beam of CaH molecules slow enough to load directly into a trap [78]. Instead of using a magnetic guide, an electrostatic guide can also be used, thereby increasing the number of species that can be guided. An example is given in reference [79] where ammonia and formaldehyde is extracted from a cryogenic reservoir via a bent electrostatic guide. The bend makes sure that only molecules below a certain forward velocity can pass through the guide. Further improvements and alterations of buffer gas beams were made by combining an oven source with a buffer gas source. This enables to introduce molecules into a buffer gas cell in a more controlled and possibly more efficient way compared to laser ablation. The use of different buffer gases was investigated as well which showed that neon buffer gas has the potential to outperform helium in terms of maximum flux of cold molecules. This was demonstrated by producing beams of guided deuterated ammonia, free-space potassium [80] and ThO [81]. The main advantage of using neon buffer gas is that it will stick to any 4K surface it encounters thereby foregoing the need of charcoal sorption pumps. This improves the pumping speed of the set-up. Although with the use of neon the buffer gas cell has to be held at higher temperatures to ensure a significant vapour pressure, the increase in forward velocity of the beam is not very much as neon is also heavier. A number of other buffer gas beams have been created and investigated, including beams of larger molecules such as naphthalene [82]. Using buffer gas as a coolant has made it possible to trap a number of species directly inside the buffer gas cell using a superconducting magnet [8]. This shows that buffer gas cooling represents a widely applicable method of cooling large number of molecules to temperatures and forward velocities low enough to be loaded into traps.

1.3 Buffer gas cooling of YbF molecules

While many species have been cooled using buffer gas cooling, there are still a number of problems in terms of stability and reproducibility of the molecular beams produced. Improvements in beam fluxes and reduction in forward velocity is desirable and therefore research in different kinds of buffer gas beams is very valuable for the field of cold molecules. This thesis presents results of buffer gas cooling of ytterbium fluoride (YbF) molecules. This is motivated primarlily by the desire to produce a slower and more intense beam of these molecules so as to improve the sensitivity of the electron EDM experiment at Imperial College [5] which is based around a YbF beam.
The YbF molecules are loaded into the buffer gas cell via laser ablation. Two different set-ups were used for cooling these molecules. The set-up described in chapter 2 consists of a buffer gas cell mounted on the cold plate of a liquid helium cryostat. Chapter 3 describes the means of probing the molecules inside the buffer gas cell and discusses the effect of the buffer gas on the saturation of the transition used to detect them. Different collision

processes between the YbF molecules and the buffer gas are investigated. Chapter 4 then looks further into the dynamics inside a closed buffer gas cell focussing on the cooling process. Knowledge from these experiments in a closed buffer gas cell were the stepping stones for the extraction of a cold and slow beam of YbF molecules. For this purpose a second set-up as described in chapter 5 was designed around a cryo-cooler. This made continuous operation of the experiment at cold temperatures possible. In chapter 6, the influences on the molecular beam using different cell apertures are investigated, as is the influence of the position of the helium inlet line with respect to the cell aperture. A second cell design based on a pulsed valve and an open cylinder was tested, which delivered the buffer gas in pulses rather than having a continuous flow. The beam characteristics of all different configurations are compared and improvements based on the experimental results are discussed. This thesis shows how a cold and slow beam of YbF molecules can be obtained.

Chapter 2

Experimental Set-up I

In the course of this PhD, two set-ups were used. The first was used to investigate the production, diffusion and thermalisation of YbF in a helium buffer gas inside a cryogenically cooled closed buffer gas cell. The second set-up was based on the results from the first and had the advantage of being built around a cryocooler, which allowed us to run the experiment continuously at low temperatures and to extract a beam of cold molecules. This set-up is described in chapter 5.

2.1 The Buffer Gas Apparatus

An Infrared Laboratories model HD3 cryostat (fig. 2.1) was modified to accommodate the buffer gas cooling apparatus. The buffer gas cell is mounted on the copper cold plate of the cryostat, connected to a low temperature dewar. This dewar can be filled with liquid nitrogen or liquid helium enabling cell temperatures of about 20 K and 80 K respectively. The reason for 20 K instead of 4 K is probably a poor thermal link between the cold plate and the aluminium cell. This was improved in the new set-up described in chapter 5. A second dewar, which is always filled with liquid nitrogen, cools an aluminium radiation shield surrounding the cold plate to 77 K to prevent room temperature radiation from heating up the cell. Windows on the radiation shield which are needed for optical access are coated with indium tin oxide to let visible light through while reflecting thermal radiation. To prevent heat conduction to the low temperature cold plate, the whole cryostat is evacuated by a Oerlikon Turbovac 361 turbomolecular pump to a base pressure of approximately 10^{-6} mbar. The cryostat itself sits on the optical table and can be filled with liquid nitrogen and liquid helium in situ. After the helium chamber has been precooled with liquid nitrogen is it necessary to take the cryostat off the table and pour excess nitrogen out in order to prevent the formation of nitrogen ice when the liquid helium is transferred into this dewar.

The buffer gas cell itself is made out of an aluminium cube of side 40 mm which has 20 mm holes drilled through five of its sides. Three of these sides have windows attached to allow optical access for the probe as well as the ablation laser, while one accommodates

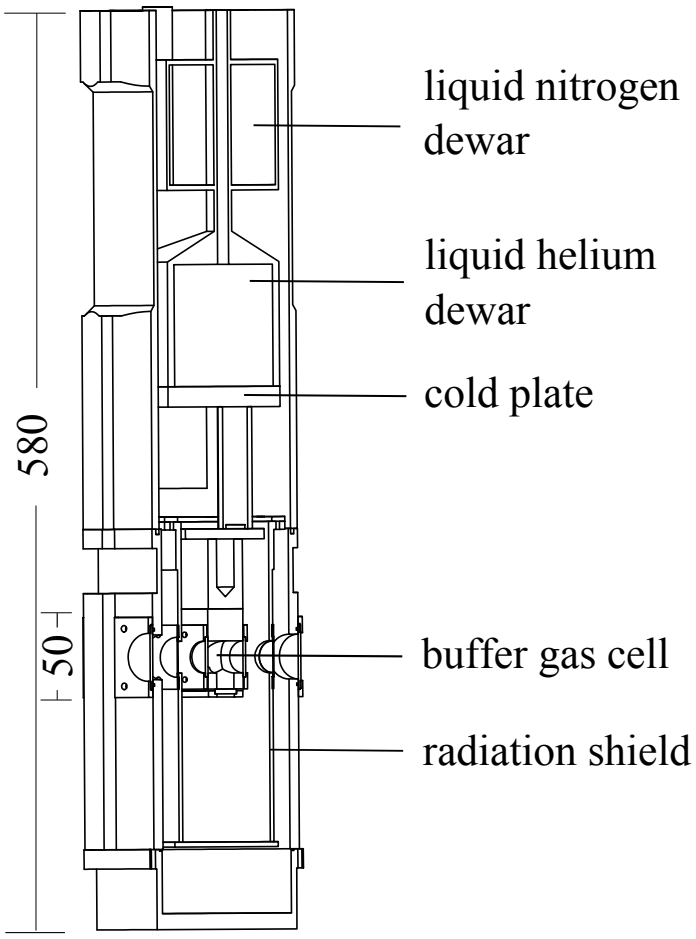


Figure 2.1: Sketch of HD3 cryostat (dimensions are given in mm)

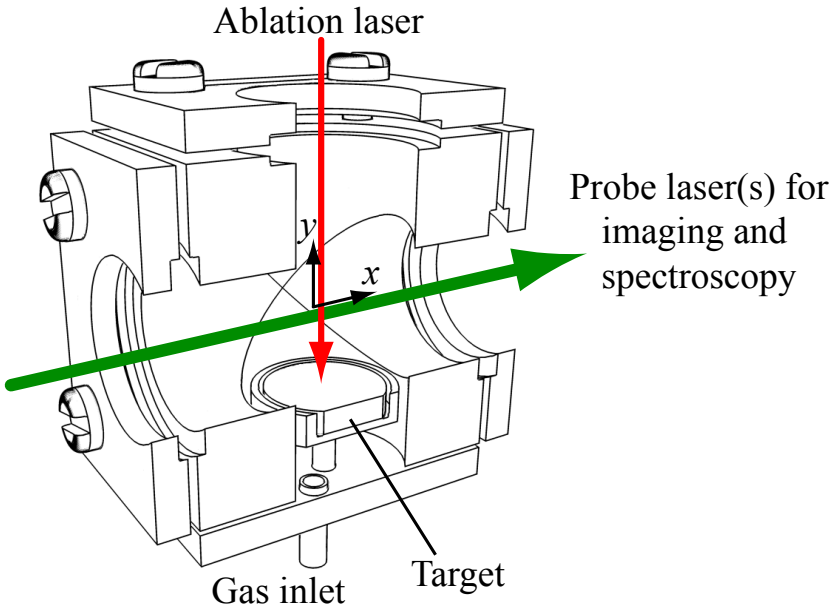


Figure 2.2: Buffer gas cell

the ablation target sitting in a holder. The fifth open side is currently blanked off but allows insertion of an aperture to extract a molecular beam out of the cell. In order to fill the cell with helium gas, a gas line of 2.5 mm diameter entering the cell just beneath the target is connected to a room temperature chamber outside the cryostat which provides helium gas of 99.996% purity. To reduce heat conduction along this tube it has thin walls and is made out of stainless steel for most of its length. The section of the tube that enters the cell is made of thicker-walled copper and is heat sunk to the cold plate to ensure that the gas has the same temperature as the cell. The helium pressure inside the cell is controlled via a Varian 951-5106 leak valve and a valve which leads to a VRC model 200-7.0 rotary pump. The pressure is monitored on the room temperature side by a Kurt J. Lesker model 945 pirani gauge (fig. 2.3).

2.2 The YbF Source

YbF is a radical, which means that it must be produced by some non-equilibrium process. The loading technique of choice is laser ablation, whereby the precursors of the molecules are evaporated from a solid target by a high intensity pulsed laser. The target consists of vacuum hot pressed AlF_3 and Yb powder with a mass ratio of 30% and 70% respectively supplied by Sophisticated Alloys. By ablating this target some of the AlF_3 molecules are broken up and can react with Yb atoms to form YbF. This process creates byproducts as well including the stable compounds YbF_2 and YbF_3. The ablation laser is a Spectron Laser Systems SL401T pulsed Nd:YAG laser operating at 1064 nm.Typical energies used in our experiments are about 50 mJ delivered in pulses of 10ns duration. The beam enters the cryostat via a small periscope and is aligned at low energies using burn paper. The

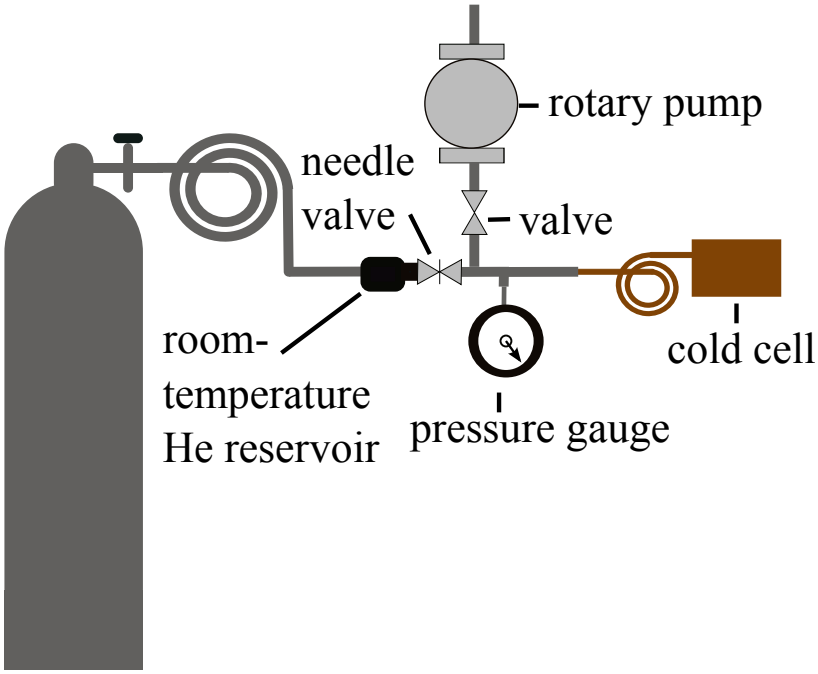


Figure 2.3: Sketch of the gas handling system (not to scale)

beam coming out of the laser is slightly expanding and has a diameter of about 2 mm when it reaches the target. This leads to a typical pulse fluence of 1000 mJ/cm^2. The laser is operated at a repetition rate of 10 Hz, and is synchronised to the 50 Hz line frequency to supress the effects of line noise in the experiment.

2.2.1 Helium pressure inside the buffer gas cell

In all experiments described in this thesis, the cell pressure is monitored on a pirani gauge at a room temperature reservoir which is connected to the cell by a narrow (2.5mm) gas line (fig. 2.3). This pressure does not necessarily equal the helium pressure inside the cell because of the limited conductance of the narrow tube and the temperature difference that exists between the cell and the gas reservoir. We therefore calibrated the pressure measured directly at the cell against the pressure measured outside of the cryostat with the whole apparatus at room temperature. For this purpose, windows on the cryostat and radiation shield were removed so that a 16mm diameter tube could be passed through the open ports and attached directly to the cell replacing one of the cell windows. This enabled us to measure the pressure directly in the cell using a second pirani gauge (Leybold). The pressure in the room temperature reservoir was monitored on the same pirani which is used for all the other experiments done with this set-up. To have a good absolute knowledge of the pressure, both gauges were calibrated to a capacitance manometer (MKS baratron), calibrated for helium gas, that has an accuracy of 0.5 % of the reading. The results for a range of pressures are displayed in figure 2.4.

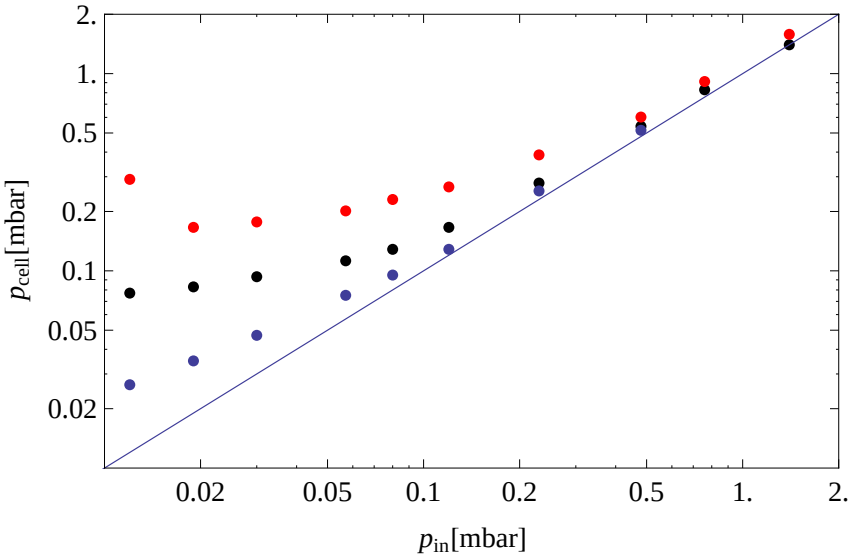


Figure 2.4: Pressure (in mbar) measured at the cell versus pressure measured at the inlet tube,blue: pumped on cell over night, red: during ablation, black: pressure settled after ablation, errors are expected to be 0.5% of the reading

The data show that the pressure measured at the cell p_{cell}, is proportional to the pressure measured outside the cryostat p_{r}, plus a constant offset p_{off}: $p_{\text{cell}} = g p_{\text{r}} + p_{\text{off}}$. The value of g, which we would expect to be 1, is found from fitting the datapoints to be 1.04 ± 0.01. The offset pressure is due to outgassing of the target and its value depends on the ablation history. After pumping on the cell overnight, the offset pressure is found to be $p_{\text{off}} = 0.014 \pm 0.003$ mbar. While the target is being ablated, the offset pressure rises to 0.174 ± 0.054 mbar. Two minutes after the ablation has been stopped, the offset has reduced to 0.053 ± 0.018 mbar. The errors on these pressure offsets are the statistical errors obtained from the fitting procedure. However this experiment was only performed once, therefore the reproducibility of these numbers is not known. Due to the complexity of the ablation process, the errors on these numbers are assumed to be much bigger. These experiments were meant to show the overall trend of the pressure inside the cell versus the helium pressure measured outside the cell in the room temperature reservoir and they show that the vacuum in our cell at room temperature is affected by ablation of the target but that we monitor the correct partial pressure of helium with the gauge that is fixed to the helium inlet tube.

Cell pressure at low cell temperatures-Thermal transpiration effects

It is expected that the pressure offset due to outgassing of the target as well as ablation byproducts is less significant for lower temperatures because most vapours freeze to the cell walls. However, when two gas reservoirs are held at different temperatures and are connected by a narrow tube, thermal transpiration has to be taken into account.
At high gas pressures, the mean free path λ of the gas is much smaller than the diameter

d of the tube and the pressure in both reservoirs will be the same because the transport is hydrodynamic. This changes for low pressures when $\lambda \gg$d, a condition referred to as the Knudsen regime. The rate of flow of molecules from reservoir 1 to reservoir 2 and vice versa will be equal to the rate at which the molecules enter the connecting tube times the probability that they exit it. In the free molecular flow regime the flows in each direction are independent and are given by the kinetic gas theory as

$$-\frac{dN_i}{dt} = An(T_i)\frac{< v(T_i) >}{4}Q_{ij}, \tag{2.1}$$

where A is the cross-sectional area of the capillary, n is the number density at temperature T_i and $< v(T_i) >$ is the mean speed at that temperature. Q_{ij} is the transmission probability from chamber i to chamber j, which is a function of the tube dimensions as well as the scattering law for the gas molecules at the tube wall. When the system reaches steady state and there is zero net flow, the two flows equalise $\frac{dN1}{dt} = \frac{dN_2}{dt}$ and the pressures in the two chambers scale as $\frac{P_2}{P_1} = \sqrt{\frac{T_2}{T_1}}\frac{Q_{12}}{Q_{21}}$ with $p = nk_{\mathrm{B}}T$ and $< v(T_i) > \propto \sqrt{T}$. In the Knudsen limit, it is assumed that $Q_{12} = Q_{21}$ and the equation simplifies to:

$$\frac{P_2}{P_1} = \sqrt{\frac{T_2}{T_1}} \tag{2.2}$$

This shows that under initially isobaric conditions if the temperature difference between two reservoirs stays constant, the gas flow is directed towards the chamber that sits at the higher temperature which leads to its pressurisation. At higher pressures, when the

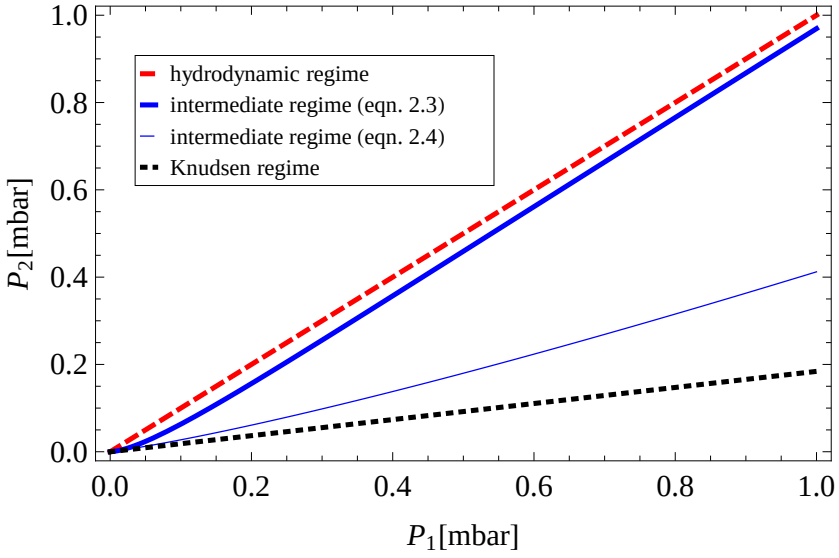


Figure 2.5: Pressure (P_2[mbar]) inside the cell(T_2=10K) as a function of input pressure (P_1[mbar], T_2=295K) for hydrodynamic regime ($P_1 \approx P_2$), intermediate regime (eqn. 2.4) and Knudsen regime(eqn. 2.2)(reservoirs are connected via 2.5 mm diameter tube)

mean free path approaches the diameter of the tube, this effect decreases as it is more and more dominated by molecular impacts and hydrodynamic effects of the streaming gas.

Therefore this simple scaling law is not a good representation for the intermediate regime and experimental evidence shows that $Q_{12} > Q_{21}$ if $T_1 > T_2$ [83]. S. Weber and G. Schmidt [84] found an empirical formula for the pressure ratio along a tube of radius R that is held at two different temperatures at both ends [84] and this formula has been used throughout this thesis to calculate the pressure inside the buffer gas cell:

$$\begin{aligned}\log\frac{p_2}{p_1} =& \frac{1}{2}\log\frac{T_2}{T_1} + 0.18131\log\frac{y_2+0.1878}{y_1+0.1878} + 0.41284 \\ & \log\frac{y_2+1.8311}{y_1+1.8311} - 0.15823\log\frac{y_2+4.9930}{y_1+4.9930}\end{aligned} \tag{2.3}$$

where $y = \left(\frac{273.25\mathrm{K}}{T}\right)^{1.147}\frac{Rp[\mu\mathrm{Hg}]}{13.42}$.

In fig. 2.5, the result of eqn.**??** (thick blue line) is compared to the solutions for the normal and Knudsen region. However there are different empirical formulas for the thermal transpiration effects. Another approximation has been found by Takaishi and Sensui [85] and it is given here and also shown in figure 2.5 (thin blue line) to show that the uncertainty of the pressure in the cell is quite big:

$$\frac{P_2}{P_1} = \frac{AX^2 + BX + C\sqrt{X} + 1}{AX^2 + BX + C\sqrt{X} + \sqrt{T_2/T_1}}; \quad (T_2 < T_1) \tag{2.4}$$

where $X = P_2 d$ and A, B, C are empircial coefficients, which for helium are given in [85].

2.3 Absorption detection set-up

A schematic of the experiment is shown in figure 2.6. The probe laser, which is a Spectra Physics model 380D dye laser pumped by a Spectra Physics BeamLok 2080-15S argon-ion laser, sits on a separate table to the cryostat and the light is delivered to the set-up via an optical fibre. This also ensures that realignment of the laser cavity does not affect the experimental alignment. The laser is operated with Rhodamine 560 dye which has a lasing range of about 60 nm. This allows us not only to address the (0–0) band of the $X^2\Sigma^+ \rightarrow A^2\Pi_{1/2}$ transitions in YbF at 552 nm but to also probe the $6s^2\ {}^1S_0 \rightarrow 6s6p^3P_1$ transition in Yb at 556 nm. A birefringent filter is used for coarse frequency selection in 75 GHz steps, while a scanning etalon in combination with dual galvo-plates is used to scan the laser smoothly over a maximum range of 30 GHz. For that purpose an external voltage is supplied to the galvanometers, which change the length of the laser cavity, as well as to a piezo, which changes the length of the etalon. The linewidth of the laser is smaller than 1 MHz. Frequency stabilisation is achieved by locking the output to a low finesse confocal Fabry Perot cavity with a free spectral range (fsr) of 0.5 GHz. To avoid mode-hops, this cavity is backed up by another confocal Fabry Perot slave cavity with a higher fsr of 10 GHz. Three beams of the probe laser are split off to be coupled into a wavemeter and to two optical cavities for frequency measurements (sec. 2.3.2). The

probe laser is then directed through a 100 MHz acousto-optical modulator (aom) used as a fast optical shutter. It is then split off into different beams according to the spectroscopy method used. For conventional absorption spectroscopy, one low intensity laser beam (50 mW/cm^{-2}) is directed through the cell and detected by a photodiode with a time-response of $\approx 10\mu$s. This allows us to measure the time evolution of the molecule density in a chosen rotational state. To record an absorption spectrum, the probe dye laser

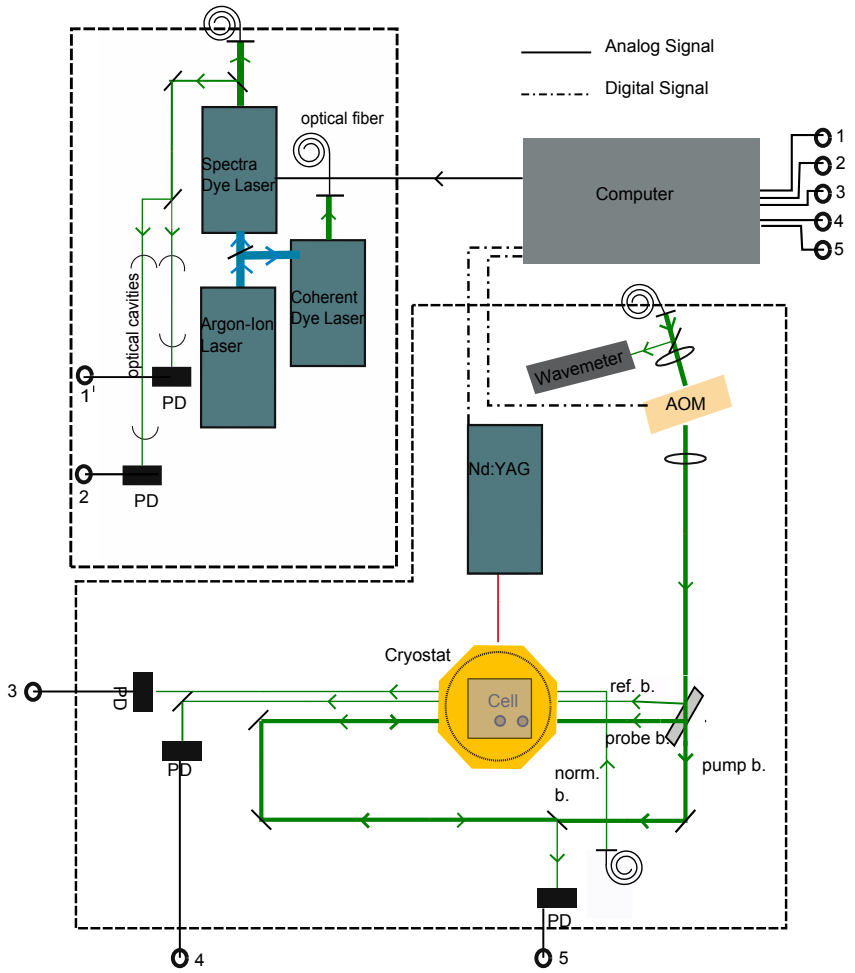


Figure 2.6: Schematic of the experimental set-up

frequency is stepped between one shot of the experiment and the next. The time-resolved signal on each shot is integrated to give the total signal as a function of laser frequency. As discussed in section 3.5, the molecular yield from ablation degrades over time and there are shot to shot fluctuations in the yield of about 10 %. To prevent our measurements from being influenced by the changing molecular yield, we constantly monitor the population in the gound state by measuring the absorption of a probe beam from a second dye laser whose frequency is fixed to the $A^2\Pi_{1/2}$-$X^2\Sigma^+$ (0-0) Q(0) transition frequency. This laser is a coherent 899 dye laser using the same Rhodamine 560 dye and pumped by the same argon-ion laser. It is frequency locked to an absorption line in an iodine vapour cell and the

output is shifted by an acousto-optic modulator to reach the desired transition frequency. The absorption signals of both probe beams are recorded by the computer. By dividing measured absorption by the relative ablation yield at each scan point the varying YbF yield is factored out.
For measuring saturated absorption spectra the frequency-tuneable beam is split into two low intensity probe beams with typical intensities of 50 mW/cm^{-2} and one pump beam with a typical intensity of 1000 mW/cm^{-2}. The pump beam is carefully overlapped with one of the probe beams while the other probe beam serves as a reference beam for the saturated absorption measurements explained in section 3.3. By subtracting the spectrum observed on the reference beam from that on the probe beam, the Doppler free saturated absorption spectrum is obtained.
For the purpose of taking absorption images, the aom is used to switch the laser on and off on a μs time scale. The laser beam is expanded to about 2 cm beam width, directed through the cell and then focussed back down onto a Marlin F033B CCD camera. The minimum shutter speed of this camera is 34 μs, using the aom to pulse on the probe laser, shorter exposure times can be obtained. For measurements where lithium was used as a reference material inside the buffer gas cell, it was detected by using a home made diode laser tuned to the D1 transition of Li.

2.3.1 Computer Control

The experiment is controlled by a home written computer program known as Scan Master. The interface is a National Instruments (NI) PCI-6534 pattern generator and a NI PCI-6251 data acquisiton card. The zero in time in the experiment is set by the ablation laser Q-switch and the data from the photodiodes is recorded from that point onwards. For the absorption spectra the probe laser frequency was scanned by supplying it with a voltage from the analog output of the data acquisition card. In order to take time dependent absorption images, the laser frequency was fixed on a particular resonance of the molecules and the time the aom switches on was scanned instead. The clock in the experiment is supplied by an approximately 1 MHz oscillator, which is phase-locked to the 50 Hz mains frequency so as to freeze the 50 Hz mains noise. The typical sampling rate for the photodiodes in these experiments is 250 kHz.

2.3.2 Frequency Monitoring

To obtain a precise measurement of the probe laser frequency, beams are split off from the main beam to be coupled into two confocal Fabry-Perot cavities as well as a HighFinesse model WS6 wavemeter which has an absolute accuracy of 600 MHz. The two optical cavities have low finesse and their free spectral ranges are 150 MHz and 750 MHz. Cavity transmission data is used to obtain an accurate linear frequency scale for the absorption scans (fig. 2.7). This is done by fitting the cavity fringes to an Airy-Function A(f(x)),

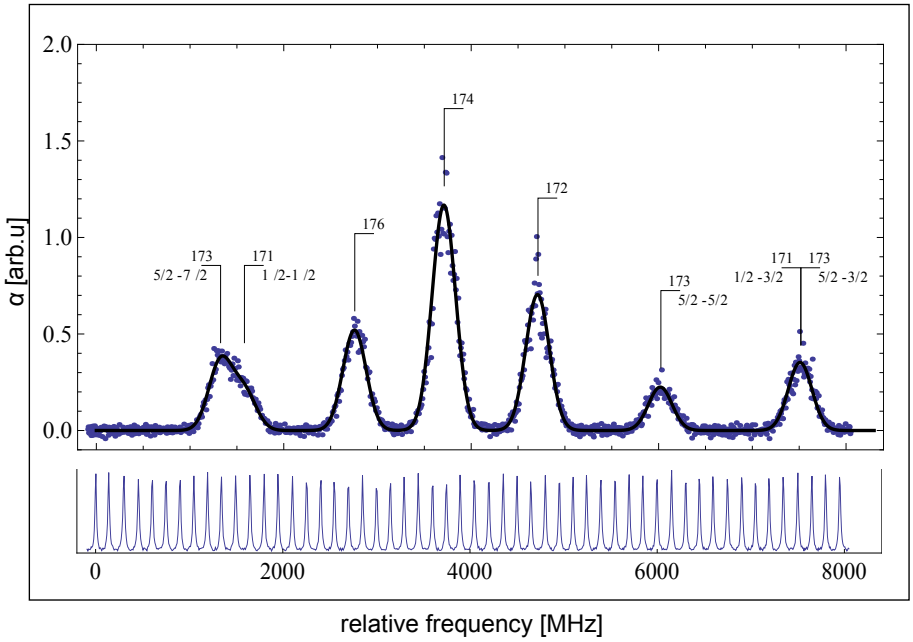


Figure 2.7: Spectrum of the $^1S_0 \rightarrow {}^3P_1$ transition in Yb used to measure the fsr of the long Fabry-Perot cavity. The different lines correspond to different isotopes of Yb as indicated. Multiple hyperfine-split lines exist for the odd isotopes.

where f(x) is a polynomial of order n, where n is the number of transmission maxima in the scan.

$$A(f(x)) = y_0 + \frac{a}{1 + F\mathrm{Sin}\left(\pi \frac{f(x)}{\mathrm{fsr}}\right)^2} \tag{2.5}$$

The fitting is done in two steps, first positions of the maxima are plotted versus the scan points and a polynomial is fitted. These values then give the starting value for the coefficients in f(x). While for the linearisation of scans the 150 MHz free spectral range cavity is more important, both are used to line up succesive scans and a relative frequency resolution better than 10 MHz is achieved. In order to measure the fsr of the long cavity, a spectrum of Yb was recorded because the spectral intervals are well known [86]. The recorded Yb spectrum is shown in 2.7 along with the data from the long cavity. Using that data we find the fsr of the long cavity to be 149.8±0.1 MHz.

Chapter 3

Absorption spectroscopy of YbF

Laser absorption spectroscopy is used to detect the YbF molecules in the buffer gas cell. This chapter presents some results obtained from saturated absorption spectroscopy and conventional absorption spectroscopy done at buffer gas cell temperatures of 80K and 10K. First the energy level structure of YbF is described so that the features in the recorded spectra can be identified. Then the basics of saturated absorption spectroscopy are described together with a model of absorption in a buffer gas cell. With this theoretical background, measurements of the saturation intensity as a function of buffer gas pressure are presented and values for collisional cross-sections and for the total number of molecules created in the cell are found.

3.1 YbF energy-level structure

As this chapter shows laser spectroscopy of the $X^2\Sigma^+ \rightarrow A^2\Pi_{1/2}$ transition in YbF, it is necessary to give a short introduction to the energy level structure of YbF. Details can be found in references [87], [88], [89] and [90].
As the experiments in this thesis were performed on the (0-0) vibrational band of YbF, the vibrational structure can be neglected and the main focus lies on the rotational levels. The rotational energy levels as a function of rotational number N are given by: $E(N) = BN(N+1)$. Although the vibrational structure is omitted here, the molecule is still treated as a vibrating rotor, meaning that the rotational constant, $B = \frac{1}{2\mu R^2}$ depends on both vibration and rotation. This is due to the fact that R increases with increasing vibration due to anharmonicity and it increases with increasing rotation due to centrifugal stretching. Therefore with the D-coefficient accounting for centrifugal stretching, the rotational constant is given by:

$$B = B_v - D_v N(N+1) + ... \tag{3.1}$$

with

$$B_v = B_e - \alpha_e(\nu + \frac{1}{2}), \tag{3.2}$$

and

$$D_v = D_\mathrm{e} - \beta_\mathrm{e}(\nu + \frac{1}{2}), \tag{3.3}$$

Here α_e and β_e are the weights for the influence of the vibrational motion and B_e and D_e are constants that depend only on the electronic state.
When YbF is formed, one 6s electron of Yb is transferred to F while the other one stays localised around Yb. Therefore the YbF molecular structure is mainly determined by the unpaired electron. The transition used for detection and spectroscopy goes from the ground electronic state $X^2\Sigma^+$ to the first electronic excited state $A^2\Pi_{1/2}$.
In the ground state $\mathrm{X}^2\Sigma^+$, the projection of the orbital angular momentum onto the internuclear axis is $\Lambda = 0$. The + sign in the ground state denotes a reflection symmetry of the electronic wavefunction through the plane containing the internuclear axis. The superscript 2 corresponds to the multiplicity $2S+1$ for $S = \frac{1}{2}$. The total angular momentum $\mathbf{J}$ is the sum of the electron spin $\mathbf{S}$ and the rotational angular momentum $\mathbf{N}$:

$$\mathbf{J} = \mathbf{S} + \mathbf{N} \tag{3.4}$$

The magnetic moment of the electron interacts with the magnetic moment associated with the rotation of the molecule giving rise to a splitting of the rotational levels into two components:

$$\begin{aligned} E_1(N) &= B_v N(N+1) - D_v N^2(N+1)^2 + 1/2\gamma N \\ E_2(N) &= B_v N(N+1) - D_v N^2(N+1)^2 - 1/2\gamma N \end{aligned} \tag{3.5}$$

In the first excited state $\mathrm{A}^2\Pi_{1/2}$, the projection of the orbital angular momentum $\mathbf{L}$ onto the internuclear axis is $\Lambda = 1$. The orbital angular momentum $\mathbf{L}$ is strongly coupled to the internuclear axis by electrostatic forces and the electron spin angular momentum $\mathbf{S}$ is coupled to $\mathbf{L}$ through spin orbit coupling. The projection of the spin onto the internuclear axis is denoted as Σ (not to be confused with the Σ that denotes $\Lambda = 0$). The projection of the total electronic angular momentum $\mathbf{J}$ onto the internuclear axis is denoted by Ω, and we have

$$\Omega = \Lambda + \Sigma \tag{3.6}$$

The large fine structure interaction gives rise to two states labelled A_1 and A_2, which have $\Omega = \frac{1}{2}$ and $\Omega = \frac{3}{2}$ respectively. In this thesis only transitions to the A_1 level are discussed, hence the subscript 1/2 on the Π. For each state with $\Omega = +1/2$ (formed from $\Lambda = 1$, $\Sigma = -1/2$), there's a corresponding state with $\Omega = -1/2$ (formed from $\Lambda = -1$, $\Sigma = +1/2$). The two are coupled by the rotation of the molecule to produce energy eigenstates of definite parity that are the symmetric or antisymmetric combinations $|\pm\rangle = |\Omega = 1/2\rangle \pm |\Omega = -1/2\rangle$. This splitting is called Λ-doubling.
The two selection rules for electric dipole transitions between the X and A states are that only transitions between opposite parity are allowed, and the difference in total angular

momentum of the upper and lower state has to be $\Delta J = 0, \pm 1$. The first rule shows that the Λ-doubling does not cause any extra transition. From a state in the ground state with particular parity $(-1)^N$, only a transition to one of the upper states is allowed. Altogether the selection rules leave six different transitions from a given Λ-doubled upper state as shown on the left of figure 3.1. These are ${}^{O}P_{12}$, P_{11}, ${}^{P}Q_{12}$, Q_{11}, ${}^{Q}R_{12}$, R_{11}, where the letters P, Q, R indicate transitions with a difference in total angular momentum of $\Delta J = -1, 0, 1$ respectively and the superscripts O, P, Q refer to changes in rotational number of $\Delta N = -2, -1, 0$. No superscript means that $\Delta J = \Delta N$. The first 1 in the subscripts corresponds to the upper A_1 whereas the second number shows if the transition goes to the E_1 or E_2 state (eqn. 3.5).

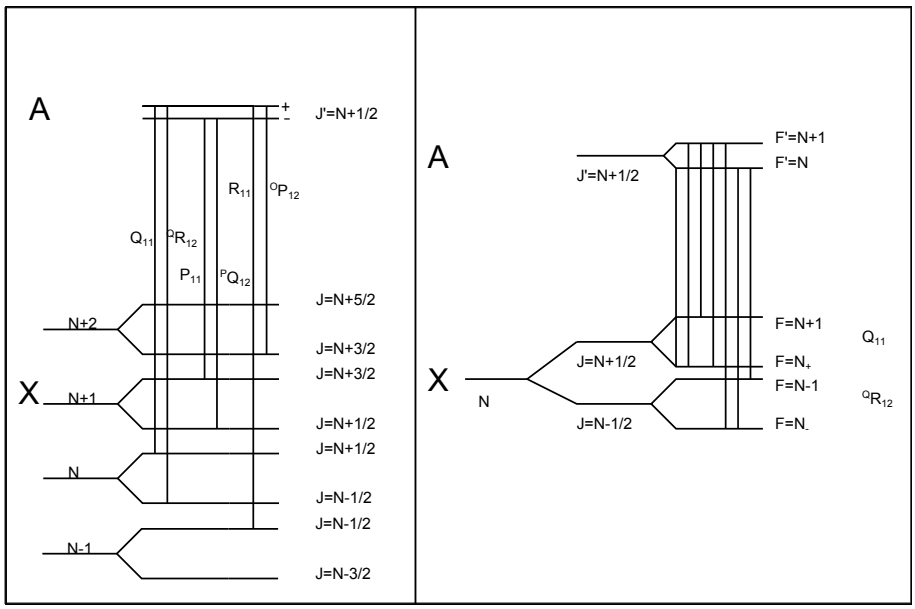


Figure 3.1: Allowed rotational transitions between the $X^2\Sigma+$ and $A^2\Pi_{1/2}$ states in YbF(left) and the hyperfine splitting of the Q-branch (right). Although there are 7 allowed transitions, because the hyperfine splitting of the upper state is so small, it cannot be resolved in our experiments. Therefore the 4 hyperfine levels of the ground state are seen in the spectra

Looking at the frequencies of the different branches explicitely, one finds that the P_{11}, ${}^{P}Q_{12}$ and ${}^{O}P_{12}$ branches have a different dependence on N than the Q_{11} , R_{11}, ${}^{Q}R_{12}$ branches. While the latter frequencies increase with N, former first decrease with N before forming a bandhead and then continuing towards the blue side of the spectrum with further increase of N. For convenience I will adopt the simpler notation ${}^{i}Q(N)$, ${}^{i}P(N)$ and ${}^{i}R(N)$, where N is the rotational quantum number and P, Q and R correspond to $\Delta N = -1, 0, 1$ as explained above. The spectra, already crowded due to small rotational constants are even more congested by having several natural isotopes of Yb indicated by the superscript i. The abundancies of the five most abundant isotopes are 14.82%(^{171}YbF), 21.83%(^{172}YbF), 16.13%(^{173}YbF), 31.83%(^{174}YbF), 12.76%(^{176}YbF). When i is not noted, the transition corresponds to the most abundant isotope ^{174}YbF.

For the even YbF isotopes, the total effective Hamiltonian for magnetic interactions is given by:

$$H_{\text{mag}} = \gamma \mathbf{S} \cdot \mathbf{N} + b\mathbf{I} \cdot \mathbf{S} + cI_k S_k + C\mathbf{I} \cdot \mathbf{N} \tag{3.7}$$

where the first term is the spin-rotation interaction that forms the doublets $J = N \pm 1/2$, $\mathbf{I}$ is the nuclear spin of the ^{19}F nucleus nucleus. I_k and S_k represent the components of the nuclear and electronic spin along the internuclear axis. The last three terms decribe the hyperfine Hamiltonian, where $b\mathbf{I} \cdot \mathbf{S} + cI_k S_k$ represents the electron-nuclear hyperfine interaction and $C\mathbf{I} \cdot \mathbf{N}$ is the interaction between the nuclear spin and the molecular rotation. The last term is very small compared to the other two except at high N. Each doublet is split again by the hyperfine interaction to form a total of four states with total angular momenta $F = N + 1, F = N$ and $F = N, F = N - 1$ as indicated on the right of fig. 3.1. This coupling scheme is also known as Hund's case ($b_{\beta J}$). At lower N both spin-rotation coupling and hyperfine interactions are comparable in magnitude, hence the quantum number J is no longer a good one in this case and as a result, the two states with $F = N$ become mixed. For the lowest N values the hyperfine interactions dominate and the electronic and nuclear spin are coupled together first to form an intermediate angular momentum $\mathbf{G}$ with $G = 0, G = 1$. Then $\mathbf{G}$ couples to $\mathbf{N}$ to form the total angular momentum $\mathbf{F}$. This coupling scheme is also referred to as Hund's case ($b_{\beta s}$).
The hyperfine splitting of the upper state is much weaker than that of the ground state as the unpaired electron has a much smaller probability of being near the nucleus. Each of the Λ-doubled states is therefore only split by a small amount (<2.5 MHz [87]) to form $F' = J' \pm \frac{1}{2}$. The total angular momentum now being F, the selection rule for an electric dipole transition becomes $\Delta F = 0, \pm 1$.The right hand side of figure 3.1 shows the hyperfine splitting of a Q-line.

3.2 Absorption Spectroscopy

A good way to detect molecules in a buffer gas cell is by laser absorption measurements. This section covers the basics of laser absorption as well as describing the details of the YbF system.
As a laser beam goes through a dilute cloud of molecules, it interacts with the gas by stimulated absorption and emission. The excited molecules can also decay back to the ground state by spontaneous emission, which leads to an observable attenuation of the light beam as it travels through the gas cloud. The loss of intensity equals the probability of the absorption of light as:

$$\frac{dI}{dz} = -\kappa(\omega) I = -\Delta n \sigma(\omega) I \tag{3.8}$$

where $\kappa(\omega) = \Delta n \sigma(\omega)$ is the absorption coefficient. Here $\sigma(\omega)$ is the absorption cross-section and $\Delta n = n_1 - n_2$, where n_i is the number density of molecules in the state i. For convenience let us first assume a two-level system. In the steady state, the net rate of

energy absorbed equals the rate at which energy is scattered out of the beam, hence:

$$(n_1 - n_2)\sigma(\omega)I(\omega) = n_2 A_{21}\hbar\omega, \tag{3.9}$$

where A_{21} is the rate of emission per molecule from state 2 to state 1. The absorption cross-section is therefore given by:

$$\sigma(\omega) = \frac{n_2}{n_1 - n_2}\frac{A_{21}\hbar\omega}{I(\omega)} = \frac{\Omega^2/4}{\delta^2 + \Gamma^2/4}\frac{A_{21}\hbar\omega}{I(\omega)} \tag{3.10}$$

The last expression is obtained by solving the optical Bloch equations of a two-level system for steady state to obtain an expression for $n_2/(n_1 - n_2)$. [91],[92]. $\Omega = \frac{E_0 z_{12}}{\hbar}$ is the Rabi frequency of the system with E_0 being the electric field amplitude of the light and z_{12} being the z-component of the transition dipole moment between states 1 and 2 ($d_{12} = \langle 1|\mathbf{d}|2\rangle$). δ stands for the detuning of the light from resonance frequency ω_0. Γ is the total rate for spontaneous emission and in the case of the two-level system is equal to A_{21}. The expression for the absorption coefficient can be simplified by inserting the expression for the Rabi frequency, writing the intensity in terms of the incident electric field amplitude squared as $I = \frac{c\epsilon_0|E_0|^2}{2}$ and using

$$A_{21} = \frac{g_1}{g_2}\frac{z_{12}^2\omega_0^3}{\pi\epsilon_0\hbar c^3} \tag{3.11}$$

where g_1 and g_2 are the degeneracies of level 1 and 2:

$$\sigma(\omega) = \frac{g_2}{g_1}\frac{3\lambda^2}{2\pi}\frac{\Gamma^2/4}{(\omega - \omega_0)^2 + \Gamma^2/4} \tag{3.12}$$

This absorption cross-section has the form of a Lorentzian function, which also gives the linewidth of the observed absorption spectrum for low intensity light where $\kappa(\omega) = n_1\sigma(\omega)$, as Γ. On resonance, the absorption cross-section reaches it maximum:

$$\sigma(\omega_0) = \frac{g_2}{g_1}\frac{3\lambda^2}{2\pi} \tag{3.13}$$

At higher intensity, the influence of the light on the population in level 1 has to be taken into account. A saturation intensity I_s can be introduced, which is the intensity on resonance needed to reduce the lower state population by a quarter. From eqn. 3.9, this intensity is found to be:

$$I_\mathrm{s} = \frac{\hbar\omega A_{21}}{2\sigma(\omega_0)} = \frac{g_2}{g_1}\frac{\pi hc\Gamma}{3\lambda^3} \tag{3.14}$$

The saturation intensity in the two level case is therefore determined by the spontaneous emission rate. This is the rate that the laser excitation has to compete with in order for the transition to become saturated. The difference in lower and upper population density

can be expressed as:

$$(n_1 - n_2) = \frac{n}{1 + \frac{I}{I_s}}, \tag{3.15}$$

where n is the total number density of molecules. By using the solution for $(\rho_{11} - \rho_{22})$ from the optical Bloch equations of a 2-level system, an expression for I_s in terms of the Rabi frequency is found as:

$$\frac{I}{I_s} = \frac{2\Omega^2}{\Gamma^2} \tag{3.16}$$

The population difference can also be expressed in those terms for detuned light, however the minimum value I_s has to be replaced by the corresponding higher value for $I_s(\omega)$. This then leads to an absorption coefficient of:

$$\kappa(\omega, I) = \frac{n\sigma(\omega)}{1 + I/I_s(\omega)} = n\sigma(\omega_0)\frac{\Gamma^2/4}{\delta^2 + \Gamma^2/4(1 + \frac{I}{I_s})} \tag{3.17}$$

This shows that for high intensities the absorption coefficient is reduced and a broadening of the spectral lines will be observed. The linewidth is increased from a FWHM of Γ to $\Gamma\left(1+\frac{I}{I_s}\right)^{1/2} = \left(\Gamma^2 + \frac{\Omega^2}{2}\right)^{1/2}$. This broadening is due to the fact that the intensity needed to saturate the transition is lowest on resonance, whereas in the wings the amount of absorption is less affected.This kind of broadening is homogeneous broadening as it affects all molecules in the same way. Another mechanism that broadens spectral lines but affects each molecule differently and is therefore inhomogeneous, is Doppler broadening. The molecules that are probed are not at rest but have a distribution of velocities corresponding to their temperature. If the molecules are at rest, they can only absorb light at a frequency ω_0, ignoring radiative broadening. However as they are moving with velocity $\mathbf{v}_1$ the Doppler shift of the light has to be accounted for, hence the frequency they are able to absorb will shift from ω_0 to

$$\omega = \omega_0\left(1 \pm \frac{v_{1z}}{c}\right) \tag{3.18}$$

Hence the distribution of absorbed frequencies reflects the velocity distribution of the particles, leading to a Gaussian lineshape as:

$$\sqrt{\frac{M}{2\pi k_B T}} e^{-\frac{Mv^2}{2k_B T}} dv = \frac{c}{\omega_0}\sqrt{\frac{M}{2\pi k_B T}} e^{-\frac{Mc^2(\omega-\omega_0)^2}{2\omega_0^2 k_B T}} d\omega \tag{3.19}$$

Therefore for higher temperatures, a gaussian can be fitted to the spectral lines and from the variance $\sigma_G = \frac{\omega_0^2 k_B T}{Mc^2}$, the temperature is obtained. For low enough temperatures, the linewidth resulting from Doppler broadening is on the same order as the one resulting from homogenous broadening mechanisms. This means that both broadening mechanisms, inhomogenous and homogeneous have to be taken into account. The composite lineshape known as a Voigt profile is a convolution of the two:

$$V(\omega - \omega_0, \sigma_G, \gamma) = \int_{-\infty}^{\infty} d\omega' G(\omega', \sigma_G) L(\omega - \omega_0 - \omega', \gamma) \tag{3.20}$$

where $G(\omega', \sigma_G)$ and $L(\omega - \omega_0 - \omega', \gamma)$ are the Gaussian and Lorentzian functions describing the two broadening mechanisms with variance σ_G and FWHM γ respectively. The integral can be evaluated to be

$$V(\omega - \omega_0, \sigma_G, \gamma) = \frac{\mathrm{Re}[w(z)]}{\sigma_G\sqrt{2\pi}} \tag{3.21}$$

with $z = \frac{(\omega-\omega_0)+i\gamma}{\sigma_G\sqrt{2}}$ and w being the complex error function.
One of the spectroscopic methods that is able to provide Doppler free spectra is saturated absorption spectroscopy. A typical set-up consists of a pump and a probe beam, that are counterpropagating and overlapping over the entire interrogation region. As the light frequency is scanned, the pump beam decreases the absorption coefficient for those molecules that have the right velocity to be resonant with ω (hole burning). As probe and pump beam are counterpropagating, the Doppler shift ensures that they are never resonant with the same molecules unless the component of the velocity along the beam is zero, in which case the resonance frequency (eqn. 3.18) for both beams becomes ω_0. Recording the signal from the probe beam then shows a dip on resonance in the absorption spectrum. This dip is the saturated absorption spectrum, the width of which is only limited by homogeneous broadening mechanisms, such as power broadening from the pump and probe beam, collisional broadening, transfer broadening or in the ideal case only radiative broadening. An angular misalignment of pump and probe beam can lead to a residual Doppler component in the observed lineshape.

3.3 Absorption and saturated absorption spectroscopy of YbF

In order to take absorption spectra of the $X^2\Sigma^+ \rightarrow A^2\Pi_{1/2}$ transition of YbF, a 1 mm diameter beam of wavelength 553 nm from a cw dye laser is sent through the buffer gas cell and onto a photodiode. The intensity is chosen to be 15 mW cm^{-2} to be in the linear absorption regime. The signal from the photodiode is usually recorded for about 8ms from the moment the ablation laser fires. A typical absorption profile can be seen in figure 3.2. When the ablation laser is fired, a sharp dip appears in the absorption profile due to fluorescence from the plume and electronic noise from the Q-switch. At the same time the molecular signal starts to appear, usually reaching its maximum between 0-200 μs after the ablation pulse. Then a decay of the absorption signal is observed on a timescale of the order of 1 ms, depending on the buffer gas density in the cell. This decay mainly corresponds to molecules diffusing to the cell walls, where they are lost.
As the spectroscopy laser intensity fluctuates between different shots, the last few points of the absorption profile, where the molecular density has dropped to zero, were used to normalise the signal. Another laser locked to the ^{174}Q(0) transition was sent through the cell as well to factor out the fluctuation of the ablation yield. Absorption spectra can be obtained, by scanning the frequency of the probe laser. A typical scan, consists of around 800 points, covering a range of 1–3 GHz with the laser frequency stepped between one shot and the next. From the full temporal profile we integrate the signal over a 100 μs time

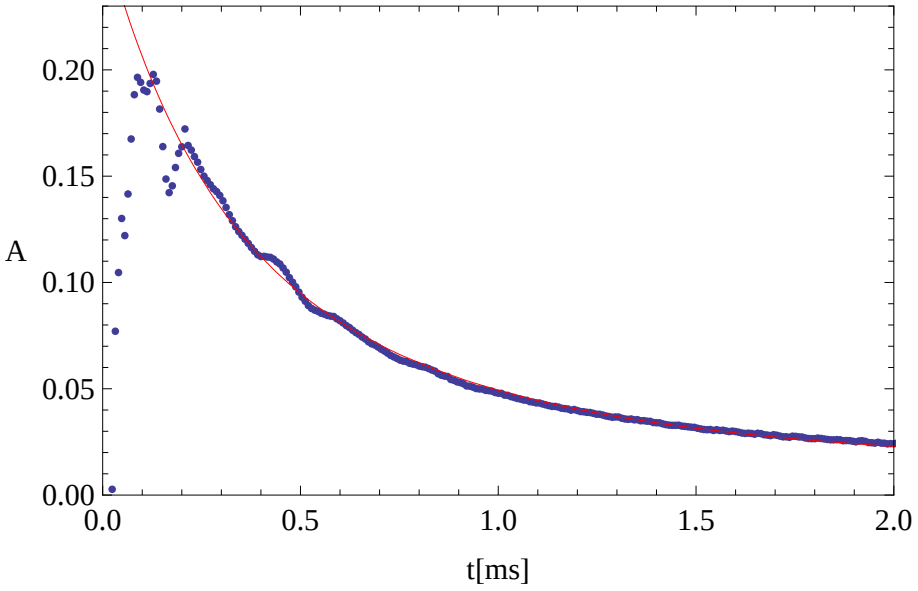


Figure 3.2: Fractional absorption signal of YbF molecules in a buffer gas cell as a function of time

slice. By varying the centre time of this time slice we can see how the spectrum varies as a function of time since ablation (sec. 4.7). The fractional absorption A is converted into optical depth α by using the relation $(1 - A) = e^{-\alpha}$ and is plotted for different frequencies to get a spectrum. These spectra show a Doppler width from about 40 MHz-120 MHz, depending on the cell temperature used.

Except at the very lowest temperatures, this Doppler broadening is much larger than the hyperfine splitting, which can therefore not be resolved using conventional absorption spectroscopy. This is overcome with the use of saturated absorption spectroscopy. The laser beam is split into three by inserting a thick glass plate. The two low intensity beams are both used as probe beams, one of them being overlapped with the pump beam, while the other is used as a reference beam. The pump beam has typical intensities of 300 mW cm^{-2}) and is sent counterpropagating to the probe beam through the cell. The normalisation laser locked to the Q(0) transition is again used to factor out the influences of differing ablation yields. Both probe lasers as well as the normalisation laser are sent onto photodiodes and the signals are recorded by ScanMaster. By subtracting this absorption spectrum from that obtained by the reference beam, a Doppler free spectrum is obtained. The frequency scale is obtained by sending some of the light into two Fabry-Perot cavities giving a relative frequency uncertainty better than 10 MHz. Our wavemeter gives an absolute precision of about 200 MHz.

3.3.1 Results

In Figure 3.3, the top graph shows a typical absorption spectrum of the Q(13) transition in YbF. The three peaks are due to the three even isotopes 172, 174 and 176 of YbF.

The measurements were performed at a cell temperature of 88 K. The expected Doppler broadening at these temperatures is 113 MHz, however the individual peaks look much broader. This is due to the unresolved hyperfine structure. The lower graph shows the

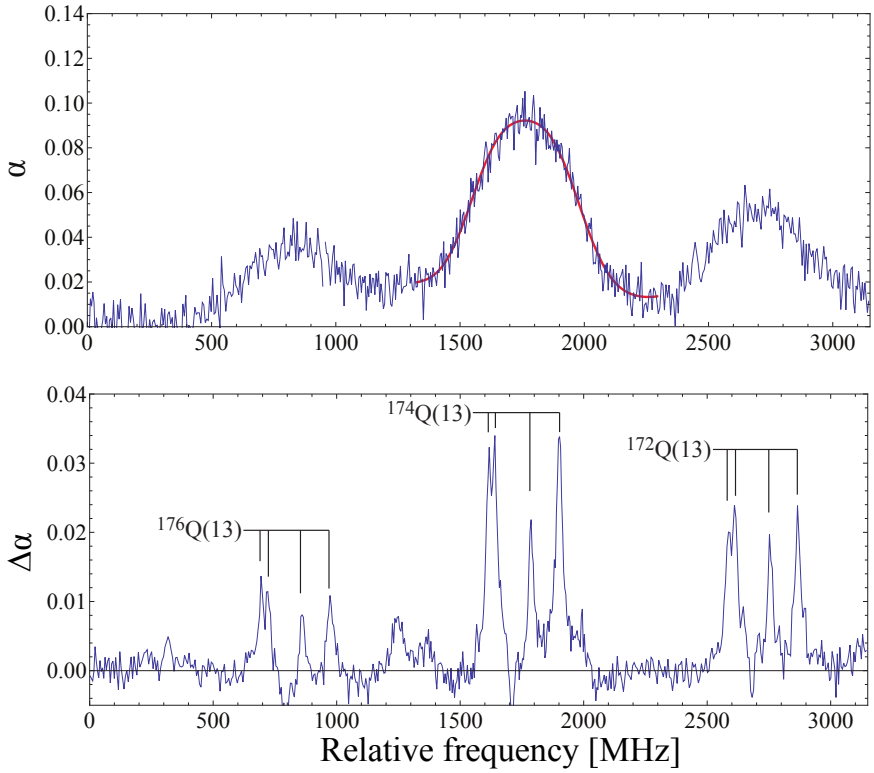


Figure 3.3: Doppler limited (top) and doppler free spectrum (bottom) of the Q(13) transition showing the three most abundant isotopes and the four hyperfine components

saturated absorption spectrum of the same line, clearly resolving all four hyperfine components in all three isotopes. Knowing the positions of the individual hyperfine levels then makes it possible to fit each line in the Doppler limited spectrum with a sum of four Voigt profiles with fixed centres and Lorentzian and Gaussian widths common to all components. The resulting temperature of 91 ±8 K from the Doppler width is in agreement with the measured temperature of the cell. The linewidth of the saturated absorption features was usually measured to be around 30 MHz. However previous high resolution spectroscopy on a YbF beam has set an upper limit of 15 MHz on the natural linewidth of the A state [87]. More recently it has been measured to be 5.7±0.2 MHz [93]. This suggests that there are other mechanisms responsible for the observed linewidth, such as angular misalignment of the beams, pressure broadening or power broadening.

As described in section 3.1 , the P-lines form a bandhead at around 542.808 THZ and then go to the blue side together with lower Q-lines. Considering also that there are three similarly abundant even isotopes in YbF, this part of the spectrum is very crowded. However by lowering the temperature of the cell, the populations of higher rotational states can be reduced, making it possible to probe the lower Q-lines without any obstructions from the P-lines. An example of this is seen in figure 3.4, where the spectrum from Q(5) to P(16)

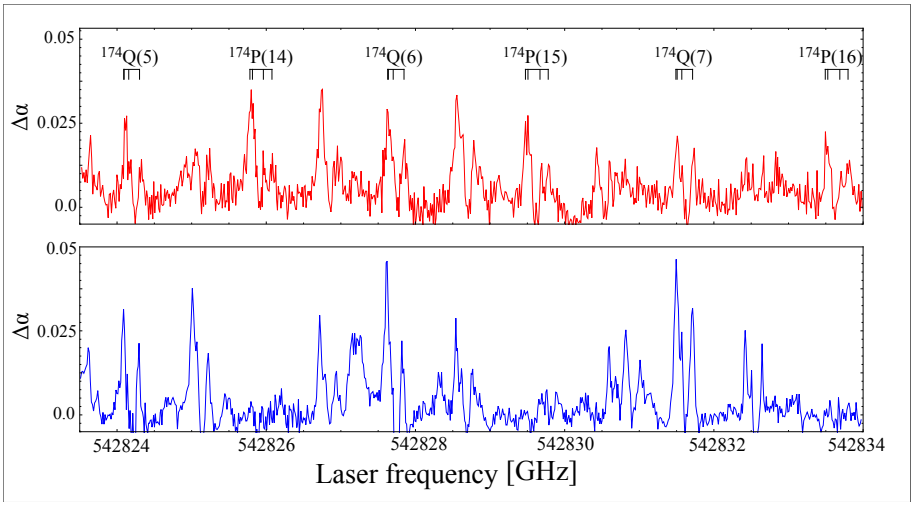


Figure 3.4: Saturated absorption spectra recorded with a buffer gas cell temperature of 80 K (upper trace) and 10 K (lower trace). At the low temperature, transitions involving the higher rotational states (the P lines) have vanished. Spectral lines that are not labeled are due to the other isotopologues of YbF.

is shown for cell temperatures of 80 K and 10 K. The upper trace taken at 80 K shows strong P(14)-P(16) lines as well as Q(5)-Q(7) lines. By contrast the P lines are not seen in the lower trace, taken at 10 K, where the thermal occupation of levels of higher N has become insignificant. Having this handle on the temperature therefore nicely allows one to probe a large number of lines without them being too obstructed by unwanted resonances. Saturated absorption spectra were measured for Q-lines originating between N=4 and N=12 using a cell temperature of 10 K and between N=13 and 21 with a cell temperature of 80 K. The spectra were fitted to Lorentzian functions to obtain an exact value of the hyperfine splittings. The two cavities with accurately-known free spectral ranges and the wavemeter were used to fix the frequency scale. The eigenvalues of the magnetic hyperfine Hamiltonian (eqn. 3.7), neglecting the nuclear spin-rotation interaction, were computed [87] and the hyperfine separations were then fitted to them. The floating parameters of this fit were the hyperfine parameters b, c and the spin-rotation coupling constant for which the functional form $\gamma(N) = \gamma_0 + \gamma_1 N(N+1)$ was used. The measured intervals as well as a global fit to all hyperfine components can be seen in figure 3.5. The best fit parameters are $\gamma_0 = -13.52 \pm 0.23$ MHz, $\gamma_1 = 4.72 \pm 0.64$ kHZ, b=139.8 ± 3.9 MHz and $c = 86 \pm 12$MHz. These measurements were published in [72].

3.4 Saturation of absorption in a buffer gas cell

Next the mechanisms responsible for the saturation of absorption in a buffer gas cell are discussed. A molecule cannot be treated as a 2-level system, as the number of vibrational and rotational levels makes sure that there is only a small probability of falling back to the inital state after some absorption-emission cycles. A way to simplify the system but

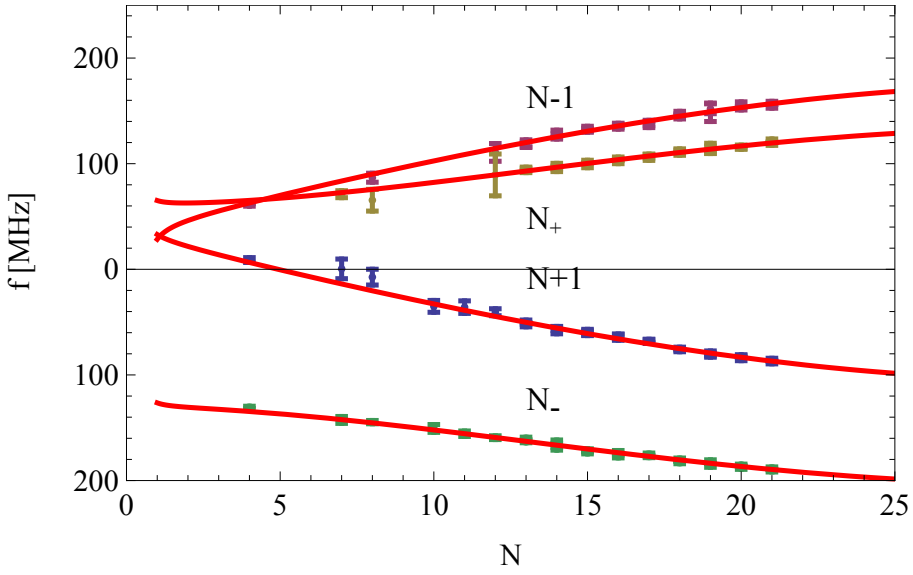


Figure 3.5: Measured frequency intervals of several $Q(N)$ transitions with fits to the eigenvalues of the effective Hamiltonian 3.7. At each N, the frequency of each hyperfine component minus the mean frequency of all four components is plotted.

include these other states is by introducing a third state that is not connected to the laser. As molecules are excited, they fall into this third level with a certain probability given by $(1 - r)$, where r is the branching ratio for the excited state to decay to the initial state. This causes the absorption to decrease as more and more molecules are pumped into dark states. The intensity needed to saturate the absorption is hence determined by a competition between this optical pumping of molecules into inaccessible states and any mechanism that repopulates the state connected to the laser. In the buffer gas cell there are three relevant mechanisms that replenish level 1. First, diffusion brings new molecules into the interaction region. This occurs at a rate ϕ in the three level absorption model. Second, inelastic collisions transfer population back from the dark states (level 3) into level 1, with a rate γ_{31}. Third since the Doppler broadening exceeds the natural linewidth, the laser only interacts with a particular velocity class. Optical pumping creates a hole in the velocity distribution but velocity changing collisions with the buffer gas refill this hole. While the rate for the first process scales with the inverse of the helium density and is very slow in these experiments, mechanism 2 and 3 are responsible for the observed saturation effects seen in our experiments.

An overview of the calculations done by M. R. Tarbutt, to obtain an expression for the fractional absorption is given below. For more detail, the reader is referred to the appendix of [94].

In this model, a plane polarised laser field, $\mathbf{E} = E_0\hat{\mathbf{z}}\cos\omega t$ is detuned from the level 1-level 2 resonance frequency by δ. It couples these two levels with Rabi frequency Ω. Level 3 represents all other vibrational and rotational states not coupled to the laser. Level 2 can decay spontaneously either to level 1 at a rate $r\Gamma$ or to level 3 at a rate $(1-r)\Gamma$. Inelastic

collisions with helium atoms also cause level 2 molecules to decay to levels 1 and 3 with rates denoted γ_{21}, γ_{23}. The molecules also collide elastically with the helium atoms which causes a dephasing of level 2 at a rate γ_{el}. Levels 1 and 3 are in the electronic ground state of the molecule, so spontaneous emission out of these levels is negligible. However population transfer from level 1 to level 3 and vice versa is possible via inelastic collisions with rates γ_{13} and γ_{31} respectively. There is not enough energy for a collision to excite a molecule to level 2. Molecules move in and out of the interaction region with a characteristic rate ϕ, which is the inverse of the average time taken to diffuse out of the probe laser beam. The total velocity changing collision rate is γ_{c}. To investigate the light-molecule interactions, the Bloch equations for the coherences ρ_{12}, ρ_{21} and the populations ρ_{11}, ρ_{22} are formulated as in [91], but including the population transfer to and from the third level, as discussed above.

The change in intensity of the light (eqn.3.8 as a function of propagation distance z can be written in terms of the coherences and the total molecular density to include all the factors that diminish the intensity of the laser beam.

$$\frac{dI}{dz} = i\hbar\omega\frac{\Omega}{2}(\rho_{12} - \rho_{21})n \tag{3.22}$$

The time of interest, over which we want to calculate the absorption is shorter than the characteristic diffusion time but much longer than $1/\Gamma$. That being so, we take n as constant and use the steady state solution of the Bloch equations. The absorption cross-section at resonance (3.13) has to be changed to include the branching ratio r and and a polaristion factor

$$p = \frac{|\langle 1, M|\mathbf{d}\cdot\hat{\mathbf{z}}||2, M\rangle|^2}{\sum_{M_1}|\langle 2, M|\mathbf{d}|1, M_1\rangle|^2} \tag{3.23}$$

accounting for the degeneracies in level 1. This then gives:

$$\sigma_0 = \frac{3\lambda^2 rp}{2\pi} \tag{3.24}$$

and the usual saturation intensity of the equivalent 2-level molecular system is given by:

$$I_{\mathrm{s}} = \frac{\pi hc\Gamma}{3\lambda^3 rp} \tag{3.25}$$

It is also convenient to introduce a dimensionless quantity that expresses the Doppler-broadened linewidth normalised to the natural linewidth $w = \sqrt{\frac{8\pi k_{\mathrm{B}}T}{M\lambda^2\Gamma^2}}$, where M is the mass of the molecules. In order to arrive at an expression for the fractional absorption $A = \frac{I_{\mathrm{in}}-I_{\mathrm{out}}}{I_{\mathrm{in}}}$, a few approximations need to be made. First of all the small absorption approximation is made, which means that we take the laser-driven excitation rate to be constant throughout the medium. We see laser absorption of about 30% in our experiments, which indicates the magnitude of the error introduced by this approximation. Then it is assumed that all collision rates are significantly smaller than the natural linewidth of the upper electronic state. The flux ϕ, is taken to be much smaller than the collision rates.

Concerning the two inelastic collision rates connecting level 1 and level 3, a relationship can be found by looking at the populations when the laser is turned off. In steady state, this yields:

$$\frac{\gamma_{13}}{\gamma_{31}} = \frac{1 - f_1}{f_1}, \tag{3.26}$$

where f_1 is the fraction of population in level 1 when the laser is turned off. In almost all situations, it is expected that $f_1 \ll 1$, as the effective degeneracy of state 3 is vastly larger than that of level 1. In that case $\gamma_{13} \gg \gamma_{31}$. The only exception would be if level 1 were the rotational ground state and the rotational temperature were much lower than the rotational spacing. This condition is not fulfilled for any of the experiments dicussed in this chapter. As mentioned above, the Doppler width is large compared to the natural linewdith. This is accounted for by writing the Bloch equations as a function of velocity. The absorption becomes a function of v and hence has to be integrated over the whole velocity distribution to find the total absorption. The detuning δ is then redefined to be the detuning from resonance minus the Doppler shift $\delta_D = \frac{2\pi v}{\lambda}$ of the molecules $\delta = \delta_L - \delta_D$. The laser beam in the experiment has a Gaussian intensity profile, which is accounted for by integrating over this distribution. The result for the fractional absorbed power when the laser is tuned to resonance, is then found to be:

$$A = \int_0^\infty d\rho \frac{\sqrt{\pi}\alpha_0 e^{-\rho^2} e^{\frac{1}{4w^2}\left(1+\frac{I_0}{I'_{\mathrm{s}}}e^{-\rho^2}\right)}}{w\sqrt{1+\frac{I_0}{I'_{\mathrm{s}}}e^{-\rho^2}}} \times \left[1 - \mathrm{erf}\left(\frac{1}{2w}\sqrt{1+\frac{I_0}{I'_{\mathrm{s}}}e^{-\rho^2}}\right)\right]\rho \tag{3.27}$$

Here I_0 is the intensity at the centre of the probe beam and α_0 is the optical depth on resonance, which is given as:

$$\alpha_0 = \frac{f_1 n \sigma_0 L}{1 + \gamma'_{21} + \gamma'_{23} + 2\gamma'_{\mathrm{el}}} \tag{3.28}$$

where L is the length of the interaction region, and primed quantities are collision rates normalized to Γ,e.g. $\gamma'_x = \gamma_x/\Gamma$. The quantity I'_{s} is the saturation intensity, which differs from the two-level saturation intensity by a factor that includes the effects of the third level,

$$I'_{\mathrm{s}} = \frac{2}{1-r}\frac{\gamma_{13} + \gamma_c}{\Gamma} I_{\mathrm{s}} \tag{3.29}$$

This shows that the intensity required to saturate the transition is proportional to the rate for repopulating level 1 via inelastic and velocity-changing collisions. The rates are related to the corresponding cross-sections by the equation:

$$\gamma_{\mathrm{x}} = n\sigma_{\mathrm{x}}\sqrt{\frac{8k_{\mathrm{B}}T}{m_{\mathrm{He}}\pi}} \tag{3.30}$$

Equation 3.29 gives an expression for the sum of the two cross-sections:

$$\sigma_{13} + \sigma_c = \frac{I'_s}{n} \frac{3\lambda^3 r(1-r)p}{2\pi hc} \sqrt{\frac{m_{\mathrm{He}}\pi}{8k_B T}} \tag{3.31}$$

3.5 Collisional cross-section measurements of YbF

On increasing the buffer gas density in the cell, it was noticed that the intensity needed to saturate the transition increased. This suggested that, information on the relevant collision cross-section could be obtained, by measuring the saturation intensity for various helium densities. We did so by sending a probe beam with a 1/e-diameter of 1250 μm through the cell. This probe was tuned into resonance with the $^{174}Q(13)$ transition. Its intensity was changed by using neutral density filters and the transmitted power was measured with a photodiode. For these measurements it was particularly important to factor out any fluctuations in the ablation yield by using the reference laser locked to the ^{174}Q(0) transition of YbF. This was again done by dividing through by the reference signal. In order to get back to absolute units of absorption for the probe, the signals were then multiplied by the average absorption of the reference beam obtained from all measurements. An average over 100 points was taken for each intensity setting at a particular helium density.

3.5.1 Results

Figure 3.6 shows an example of of measurements of factional absoprtion of YbF as a function of incident intensity. The fractional absorption decreases for higher probe intensities because of saturation. The results for three different number densities of helium are shown and it can be seen that the fractional absorption drops more rapidly for lower helium densities. This is due to competition between optical pumping, which depletes level 1 and collisional redistribution, which refills it. The measurements are fitted to the function for the fractional absorption (eqn. 3.27), obtained from the three level absorption model of YbF in a buffer gas cell. The floating fit parameters are the optical depth at resonance α_0 and the saturation intensity of the three-level system I'_s. The data fit very well to the model and from each fit a value for the saturation intensity I'_s is obtained. In figure 3.7, I'_s is plotted for various buffer gas densities. It can be seen that the saturation intensity increases linearly with buffer gas density. From eqn. 3.29 this is the behaviour we expect. This linear increase also justifies earlier assumptions that the relevant collision rates are smaller than Γ, at least for the low density data which have most weight in the fit. The gradient of the graph is found to be $\frac{I'_s}{n} = 1 \times 10^{-20}$ (Wm^{-2})/m^{-3}. This value can be inserted into eqn. 3.31 to give the sum of the two cross-sections σ_{13} and σ_c. However before a result can be obtained, the values for the polarisation factor p and branching ratio r have to be found for the ^{174}Q(13) transition that was used.

The polarisation factor p as given in eqn. 3.23 is 1/3 when averaged over all the degenerate sub-states M. The branching ratio r is the product of the Franck Condon factor

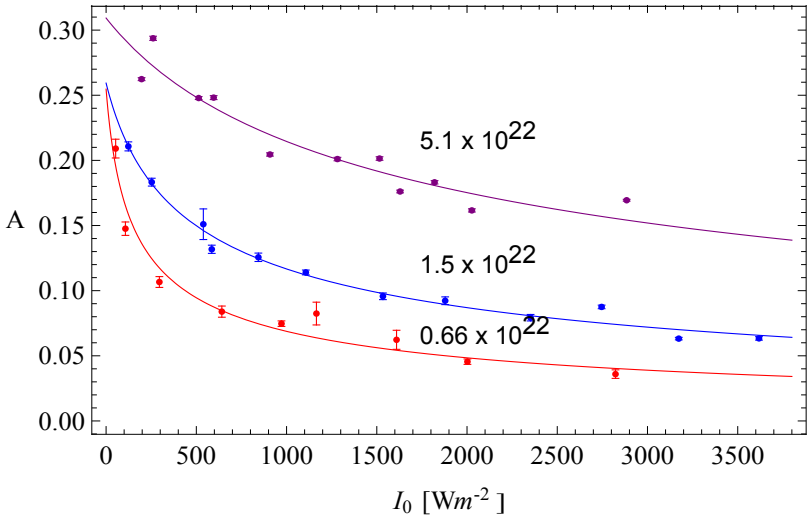


Figure 3.6: Fractional absorption A as a function of intensity at centre of probe beam for three different values of helium buffer gas density, given in atoms per m^3

Z for the (0-0) vibrational transition and a factor which gives the probability of decaying to the same rotational and hyperfine level. The branching ratios for the various rotational components are given in Appendix A. This experiment was done on the Q(13) transition which has the two components Q_{11} and ${}^{Q}R_{12}$. For the upper level $J' = 27/2$, the relative weights of these two transitions are 0.5 and 0.245 respectively. The hyperfine and spin-rotational splitting is on the same order of magnitude at $N = 13$ and the four components are split as indicated in figure 3.5, where N_- corresponds to the ${}^{Q}R_{12}$ and N_+ to the Q_{11} branch. We are able to clearly resolve two components in the spectra, but the splitting between the third and fourth component is unresolved. Therefore the branching ratio of both rotational branches is averaged and then divided by three to account for the three resolved components. This gives a ratio of $r \approx 0.25$. This factor is then multiplied by the Franck Condon factor, known to be 0.933 ± 0.003 [93], which gives $r \approx 0.23$. These results yield a value for the sum of the two cross-sections of $\sigma_{13} + \sigma_c = 37 \times 10^{-20}$ m^2. There are a number of uncertainties in determining this value. The fractional error on the gradient of the straight line is 15%. Using the spread in the diffusion lifetimes measured at the same nominal helium density, the fractional uncertainty in the measurement of the helium density is estimated to be 20%. The fractional uncertainty in calibrating the laser intensity is also 20%. The fractional uncertainty in the branching ratio r is estimated to be 24%, partly from the 5% uncertainty in the Franck-Condon factor, but mostly from the uncertainty of how best to treat the four unresolved components of the line as discussed above. This leads to a 19% error in the cross-section which depends on the value of r(1 - r). Other possible errors come from the approximations we have made in our model. First it was assumed that the absorption is small, however this does not contribute a significant error at this level. Second it was assumed that all relevant collision rates are much smaller

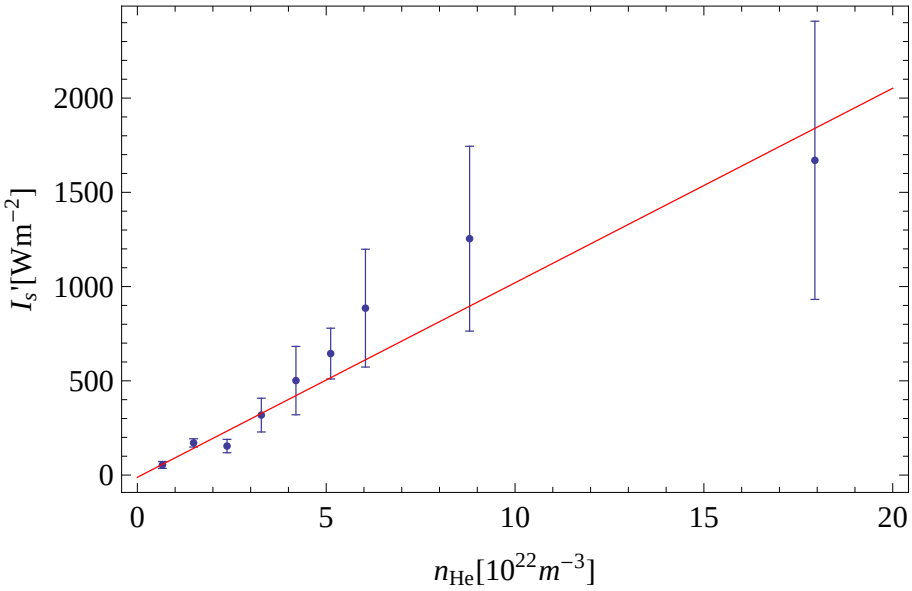


Figure 3.7: Saturation intensity I_s' as a function of helium buffer gas number density in the cell

than Γ. Γ has been measured to be $3.58 \pm 0.13 \times 10^7$rad s^{-1} and putting the sum of the cross-sections into equation 3.30 gives $\gamma_{13} + \gamma_c = 5 \times 10^7 s^{-1}$ for a helium number density of $n_{He} = 2 \times 10^{23} m^{-3}$. This implies that for the last data point, the collision rate is of same magnitude as the spontaneous decay rate. However it is the points at the lower end of the plot that have the smallest errorbars and therefore fix the gradient of the fit and for these values the collision rates are still much smaller Γ. Third we have used a fitting function that is appropriate when the laser is resonant for the molecules at rest, but this cannot be satisfied for all four of the hyperfine components. Setting the detuning from the resonance frequency to half the Doppler broadening decreases the cross-section by 3% and setting it to the full Doppler width decreases it by 12%. For 80K the Doppler broadening is quite big compared to the natural linewdith, but the error for the cross-section comes out as fairly small compared to other errors, therefore this error is negligible. Considering all the errors the final result is $\sigma_{13} + \sigma_c = 37 \pm 14 \times 10^{-20}$ m^2.

Knowing that the 3-level model with the approximations used fits well to our data, the number density of molecules in the cell can be obtained from it as well. The fractional absorption (eqn. 3.27) is a function of α_0, which is given in equation 3.28 and in the low pressure, low flux approximation becomes $\alpha_0 \approx f_1 n \sigma L$. It is therefore directly proportional to the molecular density. From the fits to the fractional absorption as a function of incident intensity, a consistent value of $\alpha_0 = 18.1 \pm 0.8$ was obtained irrespective of the helium density. The fact that the detuning is not zero for all of the four hyperfine components has more of an effect on the determination of α_0 than for I_s'. Taking this effect into account by multiplying it with the branching ratio and adding this value to the fitted α_0 gives a corrected value of $\alpha_0 = 23 \pm 4$. Using the above values for r and p and inserting them into the absorption cross-section (eqn. 3.24) gives $\sigma_0 = 1.1 \times 10^{-14} m^2$. The absorption length

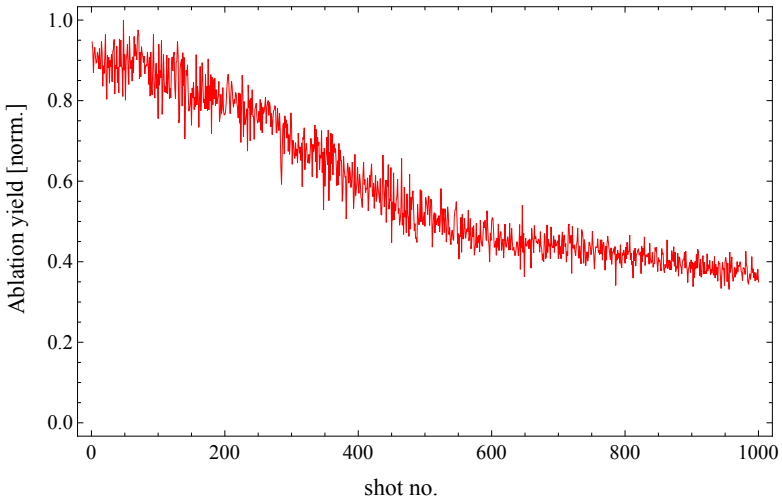


Figure 3.8: Ablation yield as a function of number of ablation shots, normalised to the highest yield in that scan

is taken to be L=3 cm and the fraction of all molecules in N=13 corresponds to $f_1 = 0.05$ for a Maxwell-Boltzmann distribution at 80K. The total density of molecules is then found to be $n_{\mathrm{YbF}} = 1.3 \times 10^{18}$ m^{-3}. Considering that the cell has a volume of about 2×10^{-5} m^3, this gives a total number of 3×10^{13} YbF molecules produced.

Figure 3.8 shows the absorption of a resonant laser beam by molecules in the cell versus the number of ablation shots. It can be seen that after an initial spike the amount of absorption degrades to less than half its inital value after 1000 shots. This effect is due to partly degradation of the target but also to coating of the window opposite of the target. As the windows become coated with ablation products, some of the ablation light is either relected back or absorbed by this layer rather than reaching the target. In order to maintain a reasonable yield of molecules, the target spot is changed by moving the ablation laser beam every few 1000 shots. The yield of molecules also changes with ablation power and spot size, however we can consistently produce this molecular density, once the experimental conditions are optimised.

3.6 Conclusion

Absorption spectroscopy has been used to detect YbF molecules in our buffer gas cell. By tuning the temperature of the buffer gas cell and thereby shifting population among rotational states, it was shown that a clean spectrum of a wide range of rotational lines can be obtained as in figure 3.4. This made it possible to determine the spin-rotation and hyperfine parameters of YbF to be $\gamma_0 = -13.52 \pm 0.23$ MHz, $\gamma_1 = 4.72 \pm 0.64$ kHZ, b=139.8 ± 3.9 MHz and $c = 86 \pm 12$ MHz. These results are in good agreement with those of similar precision obtained by laser spectroscopy of an effusive beam [95], and with more precise values obtained using the laser-rf double resonance technique reported in [88]. The

mechanisms that determine the saturation intensity of the transition used to probe YbF in the cell were investigated. As the power of the probe beam increases, the absorbed power increases linearly at first but eventually saturates because the population in the resonant state is optically pumped into states that are not resonant with the laser. The resulting hole in the combined velocity and internal state distribution is repopulated by collisions and so saturation of the absorption sets in when the rate of optical pumping is equal to the relevant collision rate. It was found that the saturation intensity has a linear dependence on the buffer gas density for densities up to 10^{23} m^{-3}. The sum of the two cross-sections $\gamma_{13} + \gamma_c$was measured to be $37 \pm 14 \times 10^{-20}$ m^2. In chapter 4 we will compare this with the diffusion cross-section for YbF in He. For most saturated absorption spectra a linewdith around 30 MHz was obtained, compared to a measured natural linewidth of 5.7 MHz. There are several mechanisms that can broaden the line, however inserting typical values for optical depth and cross-sections into the three level model shows that the observed broadening is likely to be a result of power broadening. This is further supported by the fact that the measured linewidth did not show a significant change with buffer gas pressure, thereby excluding significant pressure broadening. Finding that the 3-level absorption model fits well to the experimental data, the number density of YbF in the cell was estimated to be 1.3×10^{18} m^{-3}.

Chapter 4

Buffer Gas Cooling of YbF

The YbF molecules are formed by laser ablation of precursors inside a cold reservoir of helium gas. They thermalise by colliding with the He atoms. The following section focuses on describing the dynamics inside the cell, which is governed by diffusion of the molecules through the background gas. The time dependence of diffusion as well as heat transport are investigated to obtain a good understanding of the efficiency of the buffer gas cooling method. The most important parameter for this process is the diffusion cross-section of YbF with He and therefore it is estimated theoretically as well as measured.

4.1 Cooling in a buffer gas cell

Molecules inside a buffer gas cell are cooled by collisions with a colder gas. The gas of choice is usually helium as it has a low boiling point of 4.2 K and is inert, thereby minimising reactions with the species to be cooled. However other buffer gases such as neon may also be used as discussed in section 7. A simple hard sphere model allows one to estimate the number of collisions needed to cool the molecules. From energy and momentum conservation and after thermal averaging, the translational temperature T_{N} of the molecules after N collisions with a buffer gas at fixed temperature T_{b} is [9],[37]:

$$T_{\mathrm{N}} = (T_0 - T_{\mathrm{b}})e^{-N/\kappa} + T_{\mathrm{b}} \tag{4.1}$$

where $\kappa = \frac{(M+m)^2}{2Mm}$, T_0 is the initial temperature of the molecules, M is their mass and m is the mass of the helium atoms. In the case of He and YbF, $\kappa = 26$, meaning it takes 26 collisions to cool the molecules to $1/e$ of their initial temperature. After N collisions the molecules will have travelled a certain distance, depending on the flow regime. This distance X_{th} must lie between the distance of a diffusive random walk and a directed expansion:

$$\sqrt{N}\lambda \leq X_{\mathrm{th}} \leq N\lambda \tag{4.2}$$

If we want to cool the molecules from 2000K to 4K, 230 collisions are needed to arrive within 5% of the desired temperature. To estimate how long this takes at typical buffer

gas densities, the time between two collison events has to be estimated. It is given by:

$$t_{\mathrm{c}} = \frac{\lambda}{\bar{v}_{\mathrm{rel}}} \tag{4.3}$$

where λ represents the mean free path and $\bar{v}_{\mathrm{rel}}$ is the average relative velocity between the molecules and the buffer gas with reduced mass $\mu = \frac{Mm}{M+m}$. The mean free path, which is the average distance travelled by the YbF molecule between two collision events, is inversely proportional to the buffer gas density n and the YbF-He collision cross-section σ [96]:

$$\lambda = \frac{1}{\sqrt{2}n\sigma} \tag{4.4}$$

In the hard sphere case, $\sigma = \pi d^2$, where d is the diameter of each sphere or the sum of both radii in case the spheres are of different size. The potential energy curve for two hard spheres is then $V(r) = \infty$ for $r < d$ and $V(r) = 0$ for $r \geq d$. In reality the interaction potential as a function of r is better described by a long range attraction and a short range repulsion. A more realistic cross-section can be obtained from these potential energy curves, as explained in section 4.3. It should also be noted at this point that the diffusion and thermalisation cross-section differ from the total elastic cross-section [97]. For now, inserting typical helium densities of 5×10^{22} m^{-3} inside the cell and a typical cross-section of 10^{-18} m^2 into equation 4.4 and assuming a temperature of 4 K to calculate the average relative velocity (147 ms^{-1}) shows that the 230 collisions needed will take about 22 μs. At these densities the mean free path is about 14 μm, which means that the distance needed to thermalise (eqn. 4.2), lies between 0.21 mm and 3.22 mm.
So far cooling of the translational degrees of freedom has been discussed, however molecules also have rotation and vibration. Energy can be transferred to and from all of these degrees of freedom when collisions with the buffer gas atoms happen. Generally for a diatomic molecule three different energy transfers are possible:

- energy is transferred between the vibrational mode of molecule M and translational modes of molecule M or atom A (V-T process)
- energy is transferred between rotational modes of molecule M and translational modes of molecule M or atom A (R-T process)
- energy is transferred between the vibrational modes of two colliding molecules (V-V process)[1]

Under the assumption that the molecules are very dilute in the buffer gas, the third process can be neglected leaving only the V-T and R-T processes. If a perturbation V(t) is applied to a system but is only slowly varying compared to the time interval $\tau_{ik} = \frac{1}{\nu_{ik}} = \frac{h}{E_k - E_i}$, where $\nu_{ik}h$ represents the energy separation between two internal energy states, the system remains in its eigenstates. This is the adiabaticity condition and can be written in terms

[1] this is a resonant process as a diatomic molecule only has one vibrational mode

of a parameter ξ assuming V is applied for a time τ, as

$$\xi = \frac{\tau}{\tau_{ik}} \tag{4.5}$$

However if the perturbation is applied impulsively $\tau < \tau_{ik}$ and hence ξ is smaller than unity and the probability of transitions between the states becomes appreciable. In the case of collisions between molecules, the time interval during which the perturbation is applied is given by the ratio of an effective action range of the intermolecular force and the average relative velocity of the colliding molecules. For inducing transitions, the intense short range forces are more effective and hence in first approximation only the repulsive part of the intermolecular potential is taken into account. Therefore the effective range is at most r_ϵ at the potential minimum ϵ, giving a perturbation time $\tau = \frac{r_\epsilon}{\bar{v}_{\mathrm{rel}}}$ and an adiabaticity parameter

$$\xi = \frac{r_\epsilon}{\bar{v}_{\mathrm{rel}}} \frac{E_k - E_i}{h} = \sqrt{\frac{\pi\mu}{8k_{\mathrm{B}}}} \frac{r_\epsilon}{\sqrt{T}} \nu_{ik} \tag{4.6}$$

The above equation shows that collisions are more effective at changing the state at higher temperatures. For V-T processes, the energy levels are simply separated by $h\nu_{\mathrm{vib}}$ and $\xi = \frac{r_\epsilon}{\bar{v}_{\mathrm{rel}}}\nu_{\mathrm{vib}}$. For YbF-He collisions, $r_\epsilon \approx 5 \times 10^{-10} m^2$ and ν_{vib} is about 1.5×10^{13}Hz [98]. Even at room temperature, where $\frac{r_\epsilon}{\bar{v}_{\mathrm{rel}}}$ is 4×10^{-13}s, this gives $\xi \approx 6$, which means that the V-T exchange is relatively unlikely. Anharmonicity reduces the frequency of higher vibrational transitions, hence energy transfer between vibrations and translations becomes more likely for high vibrational levels.

To estimate the probability for R-T energy transfer, a rigid rotor is assumed to describe the rotational energy levels and hence the energy difference between the rotational states defined by the quantum numbers N and $N+1$ is $E_{N+1} - E_N = 2B(N+1)$, where B is the rotational constant, which is for YbF $\approx 7 \times 10^9$Hz$\times h$ [98]. This gives a $\xi = \frac{r_\epsilon}{\bar{v}_{\mathrm{rel}}} \frac{2B(N+1)}{h}$, which for the lowest rotational level is $\approx 6 \times 10^{-3}$. This is much smaller than unity and hence energy transfer between rotations and translations is very efficient. It can be seen that ξ increases with increasing quantum number N, which means that the transfer of rotational energy quanta to the translations is more efficient at lower rotational levels. This can cause an overpopulation of upper rotational levels with respect to the Boltzmann distribution. Taking these ideas into consideration, we may expect that buffer gas collisions will cool the translational and rotational degrees of freedom efficiently but perhaps not the vibrations.

4.2 Diffusion in a buffer gas cell

The ablation process and the formation of the molecules happens on a sub μs timescale. However movement on a longer millisecond timescale is governed by diffusion of the molecules through the helium background gas. The flux $\mathbf{j}$ is driven by the gradient of

the number density n:

$$\mathbf{j} = -D\nabla n \tag{4.7}$$

where D is a proportionality constant with units $\mathrm{m}^2\mathrm{s}^{-1}$ and known as the diffusion coefficient. Putting this into the continuity equation $\frac{\partial n}{\partial t} = -\nabla\mathbf{j}$ and assuming an isotropic diffusion coefficient, one obtains the time dependent diffusion equation:

$$\frac{\partial n}{\partial t} = D\nabla^2 n \tag{4.8}$$

The general solution of this equation is a superposition of diffusion modes k each having its own amplitudes a_k and time constant τ_k:

$$\mathbf{n}(\mathbf{r}, t) = \sum_k a_k f_k(\mathbf{r}) e^{-t/\tau_k} \tag{4.9}$$

The $f_k(\mathbf{r})$ are the solutions to the spatial diffusion equation:

$$\frac{f_k}{D\tau_k} + \nabla^2 f_k = 0 \tag{4.10}$$

For diffusion in a buffer gas cell, the boundary conditions are given by the cell geometry, where it is assumed that the particles are immediately lost as soon as the cell walls are reached ($n = 0$). For simple geometries eqn. 4.10 can be solved analytically and it can be seen that higher order diffusion modes have a shorter time constant τ_k associated with them. For example taking the simple geometry of a cube of side length a, the solution is[96]:

$$n(x, y, z, t) = \sum_{k=0}^{\infty} A_k \cos\left[\frac{(2k-1)\pi x}{a}\right] \cos\left[\frac{(2k-1)\pi y}{a}\right] \cos\left[\frac{(2k-1)\pi z}{a}\right] e^{-\frac{t}{\tau_k}} \tag{4.11}$$

where:

$$\frac{1}{D\tau_k} = \frac{3\pi^2(2k-1)^2}{a^2} \tag{4.12}$$

4.3 The diffusion cross-section

To be able to relate the diffusion coefficient to a diffusion cross-section, we take a step back and look at elastic collisions in general. To treat elastic collisions of two bodies, it is useful to work in the centre of mass reference frame, where the centre of mass moves with a constant velocity $\mathbf{v}_\mathrm{m} = \frac{m_1\mathbf{v}_1 + m_2\mathbf{v}_2}{m_1+m_2}$ and the relative velocity of the two colliding species is $\mathbf{v}_\mathrm{r} = \mathbf{v}_1 - \mathbf{v}_2$. Considering momentum conservation, the pre-and post collision velocities denoted without and with an asterisk respectively, are given in this frame of reference as:

$$\mathbf{v}^*_{1(2)} = \pm\frac{m_2(m_1)}{m_1 + m_2}\mathbf{v}^*_\mathrm{r} \tag{4.13}$$

Considering energy conservation shows that the magnitude of the relative velocity is unchanged by an elastic collision. The whole problem is therefore reduced to the calculation of the scattering angle χ. This calculation is simplified by recognising that the motion of a particle of mass m_1 relative to a molecule of mass m_2 is equivalent to the motion of a particle with reduced mass $\mu = \frac{m_1 m_2}{m_1+m_2}$ relative to a fixed centre of force.

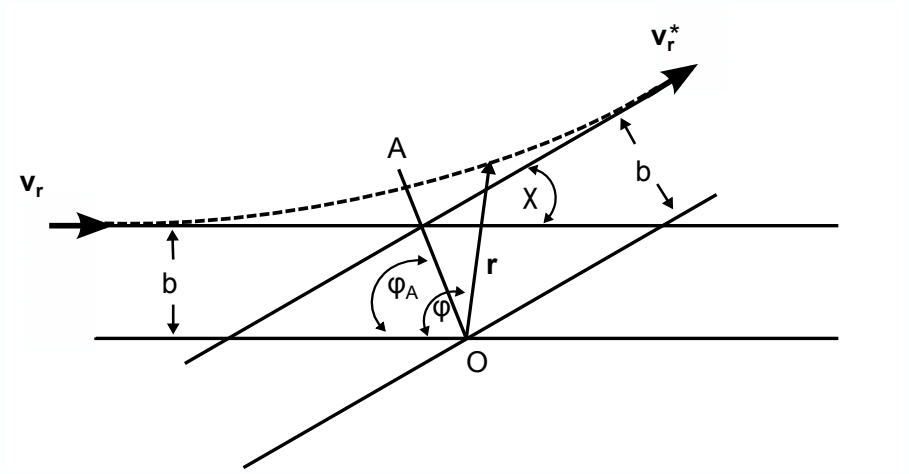


Figure 4.1: Elastic scattering problem of two particles simplified to the centre of mass frame and one particle of reduced mass that is deflected from a fixed scattering centre (after [99])

This scattering problem, which has been reduced to calculating one trajectory is displayed in figure 4.1, where the impact parameter b denotes the distance between particle and scattering centre perpendicular to the incoming velocity. The first step to obtain the differential scattering cross-section is then to find an expression for the deflection angle χ. Using the polar coordinates r and ϕ as displayed in figure 4.1, the equation for the angular momentum is [2]

$$r^2\dot{\phi} = \text{const} = b\mathbf{v}_\text{r} \tag{4.14}$$

The energy is the sum of potential and kinetic energies, which for large distances is the asymptotic kinetic energy E:

$$\frac{1}{2}\mu(\dot{r}^2 + r^2\dot{\phi}^2) + V(r) = \text{const} = \frac{1}{2}\mu v_\text{r}^2 = E \tag{4.15}$$

In the above equation, V(r) describes the inter-particle potential. From eq.4.14 and 4.15, time may be eliminated to give the equation for the orbit as:

$$\left(\frac{dr}{d\phi}\right)^2 = \frac{r^4}{b^2} - r^2 - \frac{2V(r)r^4}{\mu v_\text{r}^2 b^2} \tag{4.16}$$

[2] where a dot denotes a time derivative

Solving this for the angle ϕ gives:

$$\phi = \int_0^\infty dr \, \frac{b}{r^2} \frac{1}{\sqrt{1 - V(r)/E - b^2/r^2}} \tag{4.17}$$

At the intersection of the orbit with the apse line OA, $\phi = \phi_{\rm A}$ and $\frac{dr}{d\phi} = 0$ and hence solving

$$1 - V(r_{\rm m})/E - b^2/r_{\rm m}^2 = 0 \tag{4.18}$$

gives the classical turning point $r_{\rm m}$. The value for $\phi_{\rm A}$ is then obtained by evaluating the integral for ϕ between the turning point and infinity.

$$\phi_{\rm A} = \int_{r_{\rm m}}^\infty dr \, \frac{b}{r^2} \frac{1}{\sqrt{1 - V(r)/E - b^2/r^2}} \tag{4.19}$$

From figure 4.1, it can then be seen that the scattering angle $\chi(E, b)$ for the relative velocity is:

$$\chi(E, b) = \pi - 2\phi_A = \pi - 2b \int_{r_{\rm m}}^\infty dr \, \frac{r^{-2}}{[1 - V(r)/E - b^2/r^2]^{1/2}} \tag{4.20}$$

Knowing the scattering angle χ, an expression for the differential cross-section can be derived. The differential cross-section is the fraction of particles with energy E that are scattered at an angle χ into the solid angle $d\Omega = \sin\chi d\chi d\epsilon$, where ϵ is the azimuthal angle. $d\sigma$ is the area occupied by particles that are scattered through an angle in the range $\chi \to \chi + d\chi$. These particles have impact parameters in the range $b \to b + db$, and the area they occupy is $2\pi b db$.

$$\begin{aligned} \frac{d\sigma}{d\Omega} d\Omega &= b \, db \, d\epsilon \\ \Rightarrow \frac{d\sigma}{d\Omega} &= \Big(\frac{b}{\sin\chi}\Big) \frac{db}{d\chi} \end{aligned} \tag{4.21}$$

To obtain the total elastic scattering cross-section, eqn. 4.21 is integrated over the whole solid angle. We are interested in the diffusion cross-section. From fig. 4.1, it can be seen that after the scattering, the relative velocity remaining in the direction of the initial relative velocity $\mathbf{v}_r$ is $\cos\chi \mathbf{v}_{\rm r}$. In evaluating the diffusion cross-section we have to weight the differential cross-section by $(1 - \cos\chi)$ to acount for the fact that backward scattering is more effective at limiting diffusion than forward scattering. Thus, the diffusion cross-section $\sigma_{\rm D}$ is [99]:

$$\sigma_{\rm D}(E) = \int d\Omega \, (1 - \cos\chi) \frac{d\sigma}{d\Omega} = 2\pi \int_0^\infty db \, b(1 - \cos\chi) \tag{4.22}$$

Experimentally it is common to measure the diffusion coefficient D, which is dependent on temperature, pressure and the diffusion cross-section of the particles involved. In 1917, Chapman and Enskog individually [100, 96, 101, 99, 102] established a relationship between the diffusion coefficient D_{12} and the diffusion cross-section $\sigma_{\rm D}$ for diffusion of gas 1 into

gas 2 (which has a number density n) in a binary mixture at a certain temperature T. In the first approximation, the diffusion coefficient is given as:

$$D_{12} = \frac{3}{16}\left(\frac{2\pi k_B T}{\mu}\right)^{\frac{1}{2}} \frac{1}{n} \frac{1}{\int_0^\infty dx\, e^{-x^2} x^2 \sigma_D(E)} \tag{4.23}$$

The integral

$$\bar{\sigma}_D = \int_0^\infty dx\, e^{-x^2} x^2 \sigma_D(E) \tag{4.24}$$

with $x = \frac{E}{k_B T}$, is often called the collision integral and is essentially the temperature averaged diffusion cross-section. This is also the quantity that is determined from our diffusion experiments of YbF through helium.

4.3.1 Calculation of Li-He diffusion cross-section

The Li-He system is experimentally very well studied. As discussed in section 4.4, it can act as a good reference for calibrating the YbF cross-section. In order to calculate the cross-section, we use the Li-He interaction potential of reference [103], calculated using pseudopotentials. The datapoints given are interpolated. In order to calculate the scattering angle, the classical turning points for different impact parameters and inital kinetic energies have to be found first, which is done by solving equation 4.18. Having calculated r_m, the interpolated interaction potential function is put into eqn. 4.20 to obtain the scattering angle as a function of different impact parameter and initial kinetic energies. The diffusion cross-section is then evaluated using eqn. 4.22.

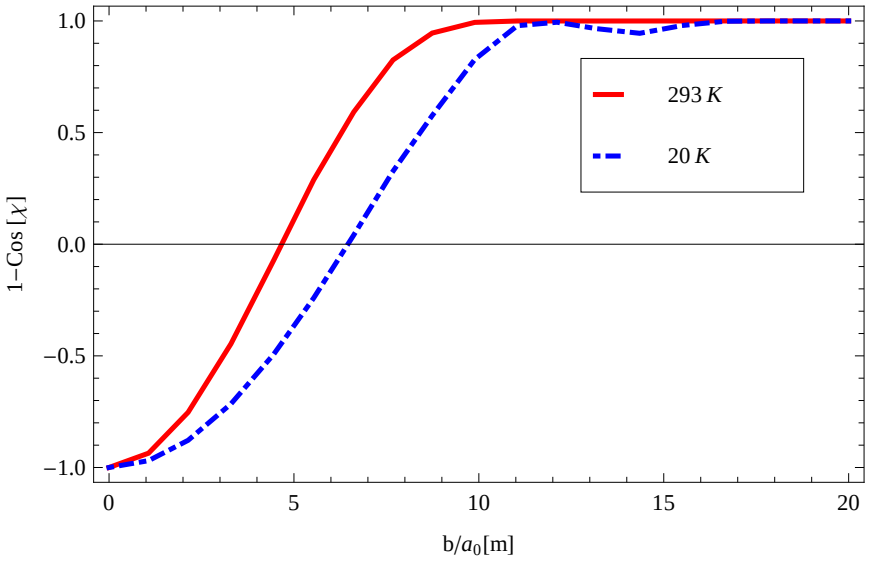


Figure 4.2: The cosine of the scattering angle χ as a function of impact parameter b in units of Bohr radii for Li-He collisions(full red line:293 K, dashed blue line:20 K)

Figure 4.2 shows the cosine of the scattering angle for two energies corresponding to

temperatures of 293 K and 20 K as a function of the impact parameter. One can see that for values of the impact parameter higher than 20 Bohr radii, the function goes to 1. Hence for higher impact parameters, the particles are too far away from each other to experience scattering events that significantly change the forward momentum. It also means that when integrating the scattering angle over all impact parameters to obtain the momentum transfer cross-section, the integral only has to be evaluated from $b = 0$ to $b = 20$, where b is in units of the Bohr radius a_0. Using eqn. 4.24 for a particular initial temperature T, then yields $\bar{\sigma}_{\mathrm{D}}$, which can be compared to experimental data. The results for 20 K, 80 K and 293 K are 71×10^{-20} m^2, 51.9×10^{-20} m^2 and 35.8×10^{-20} m^2 respectively
To look at the accuracy of the theoretical results for the energy averaged cross-sections, they are compared to other calculations from references [104] and[105] and show an agreement better than 6% at the temperatures of interest, where the best agreement is for room temperature and a slightly worse agreement is seen for lower temperatures. To get another error estimate, we investigated how much the end result changes if the depth of the interaction potential is increased by 10%. This showed a worst deviation from the original result of 4% for the 20K cross-section.
So far, the calculation has been classical, therefore it should be estimated if quantum effects need to be considered as well. They become important if the de Broglie wavelength $\lambda = \frac{\mathrm{h}}{p}$ where p is the momentum of the particle, approaches the size parameter R of the interatomic potential (V(R)=0). Gases behave classically for $\lambda/R \ll 1$. For a pair of colliding molecules with reduced mass μ and kinetic energy equal to the depth ϵ of the interatomic potential, the ratio λ/R is given by

$$\Lambda^* = \frac{h}{R\sqrt{2\mu\epsilon}} \tag{4.25}$$

which is called the de Boer parameter. For the Li-He interaction potential, the depth is about 3.5×10^{-23} J and $R = 5 \times 10^{-10}$. This gives a de Boer parameter of 2, which from table 1 of reference [101] means that quantum effects can increase the cross-section at 20 K by 2%. Taking all above considerations into account an error of 5% was estimated for all temperatures for the calculated Li-He cross-section.

4.3.2 Calculation of YbF-He diffusion cross-section

In order to calculate the diffusion coefficient for YbF through a helium buffer gas for different temperatures and buffer gas pressures, the interaction potential is required. The group of R. V. Krems [106] have calculated the potential energy surface for YbF-He and this is our starting point.

First the classical turning points for different impact parameters and inital kinetic energies have to be calculated again, which is done in the same way as for lithium. However this time V has a dependence on the angle of incidence Θ relative to the molecular axis as well as the interatomic distance r as it makes a difference whether the He atom sees more

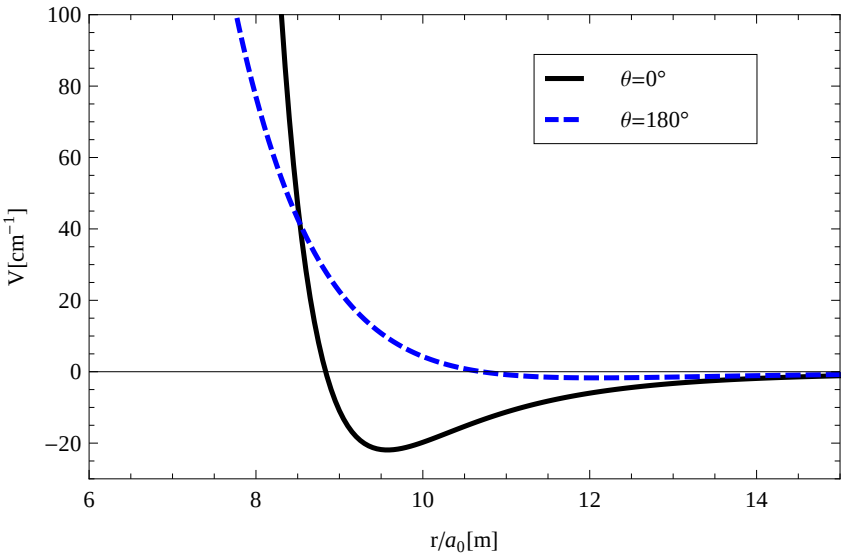


Figure 4.3: Potential energy curve for an angle Θ of 0°(black) and 180°(blue,dashed)

of the fluorine atom or the ytterbium atom. Θ is defined as taking the value zero for a head on collision on the fluorine side. As can be seen when looking at the potential energy surface, the potential well depth is deepest for this configuration. If the helium atom approaches the molecule on the ytterbium side ($\Theta = 180°$), the attraction is much weaker and the repulsion begins at larger values of the interatomic distance r. As the interatomic potential is only given for values of r between 1.5-4 bohr radii, it is assumed that the potential decays as r^{-6} for larger values of r.
Once r_m is known, the scattering angle can be evaluated using equation 4.20. Just as for lithium, the contribution to the integral is negligible for impact parameters bigger than 20 a_0.
After the function $\sigma_\mathrm{D}(E, \Theta)$ has been found, the collision integral is solved for a specific temperature using equation 4.24. This then gives a result dependent on Θ,but due to the random orientation in the large number of collisions inside the cell, it is reasonable to assume that all angles of approach are sampled equally [99]. Hence the average over all angles is taken in determining the value for the diffusion cross-section $\bar{\sigma_\mathrm{D}}$. For 20 K, 80 K and 293 K this yields $79.6 \times 10^{-20}\mathrm{m}^2$, 55.8×10^{-20} m^2 and 40.9×10^{-20} m^2 respectively. As the same method as for calculating the lithium cross-section has been used, the same error of 5% on the calculated results is assumed.

4.4 Measurements of the YbF-He diffusion cross-section

In order to measure the diffusion cross-section of ytterbium fluouride molecules in a helium buffer gas, the molecular density is probed as a function of time by measuring the amount of laser absorption. In the diffusion equation 4.10, the term $\frac{1}{D\tau_\mathrm{k}}$ is only dependent on the boundary conditions. In our case these are given by a zero molecular density at the cell

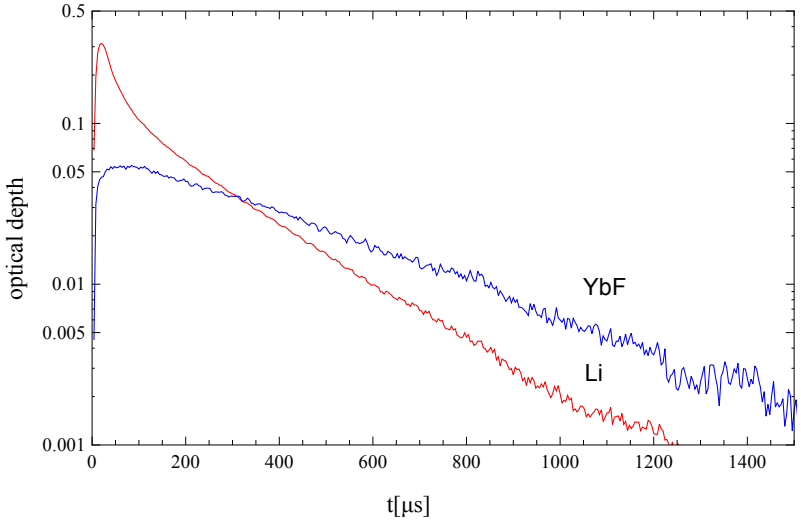


Figure 4.4: Laser absorption profiles as a function of time for both lithium (red) and YbF(blue) for helium density of $2.2 \times 10^{22}\mathrm{m}^{-3}$ and a cell temperature of 293K

walls, as there the molecules stick and are lost. This is the same for all species and hence for a particular diffusion mode, the term $\frac{1}{D\tau_k}$ is a constant. For the buffer gas cell used, the diffusion equation cannot be solved analytically. Also as will be discussed further in section 4.6, the initial populations of the various diffusion modes depends on the buffer gas density. For these reasons, it can be advantageous if a reference atom with a well known diffusion cross-section is used to provide a calibration. For that purpose a lithium wire was mounted on the target used for YbF ablation and a second probe laser resonant with the D1-line of lithium at 671 nm was overlapped with the YbF detection laser. This ensured that both species could be produced with the same ablation shot and detected at the same place. With this method it is reasonable to assume that inital conditions and dominant diffusion modes are the same for both species. In that case the YbF diffusion cross-section can be evaluated using:

$$\frac{D_{\text{He-YbF}}}{D_{\text{He-Li}}} = \frac{\tau_{\text{Li}}}{\tau_{\text{He-YbF}}} \tag{4.26}$$

where D is given by eqn. 4.23. As the temperature and helium density for both species are the same, this simplifies to:

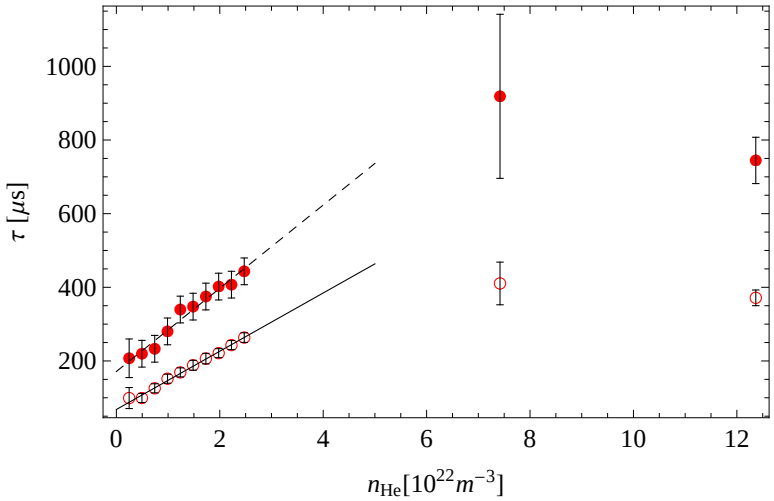
$$\bar{\sigma}_{\text{He-YbF}} = \bar{\sigma}_{\text{He-Li}} \sqrt{\frac{\mu_{\text{Li}}}{\mu_{\text{YbF}}}} \frac{\tau_{\text{YbF}}}{\tau_{\text{Li}}} \tag{4.27}$$

4.4.1 Results

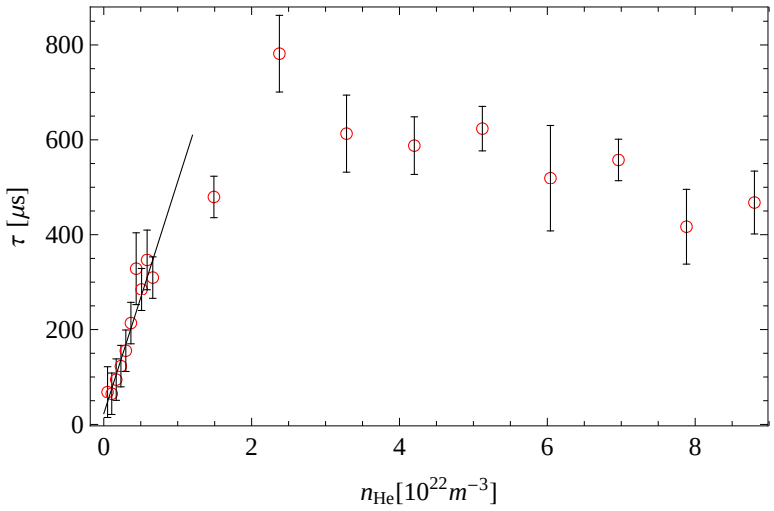
Figure 4.4 shows an example of laser absorption profiles as a function of the time since ablation for Li and YbF. For times greater than about 300 μs, the absorption curves fit exponential decays well, and it is the time constant of these fitted exponentials that we call the diffusion time constant. These time constants were measured for a range of buffer

gas densities and for three temperatures, 20 K, 80 K and 293 K. At 80 K, only Li data was obtained. The results are shown in figure 4.5. The error bars represent the typical standard deviations estimated from repeated measurements under the same conditions. The diffusion times are expected to vary linearly with helium density, as indicated by eqn. 4.12 and eqn. 4.23. This is observed et low densities. At higher densities a levelling off of the time constants is seen. This behaviour is displayed by both YbF and Li at 293 K, by Li at 80 K and YbF at 20 K. The data for Li at 20 K appear to show a more complicated behaviour at high density. For Li, the lifetimes level off at approximately 400 μs at 293K, 600 μs at 80 K and roughly 500 μs at 20 K. For YbF the corresponding values are approximately 800 μs at 293 K and 1000 μs at 20 K. The density at which this deviation from the linear behaviour appears is about the same for the two species and shifts to lower values as the temperature is lowered.
To obtain the diffusion cross-section, only the data points at lower densities that behave as expected for diffusion were included in the linear fit. For 80 K and 293 K this meant that the first 10 points were used. For the 20 K data it was not clear whether to fit the first 4 or 5 data points. The gradients of the two fits are consistent within errors and the weighted mean of these two fits was taken as the best estimate.

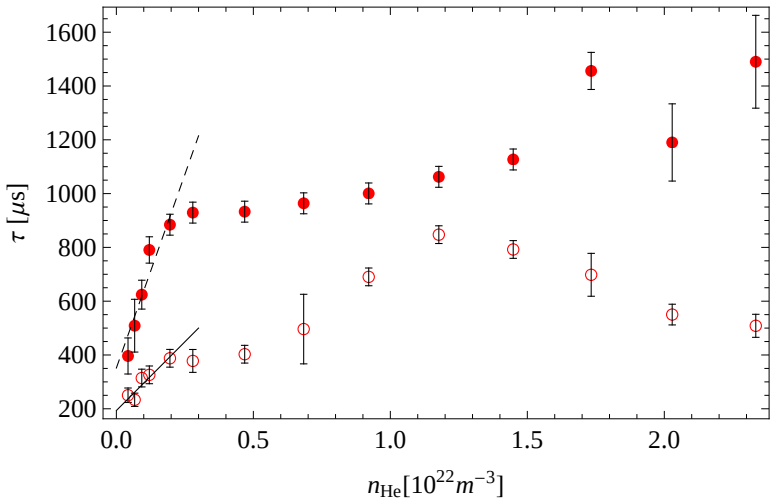
Using the theoretical result for the lithium diffusion cross-section at 20 K and 293 K (sec. 4.3.2), the fitted gradients give YbF diffusion cross-sections of $(203 \pm 75) \times 10^{-20}$ m^2 at 20 K and $(41 \pm 4) \times 10^{-20}$m^2 at 293 K. Comparing these to the calculated cross-sections at 20 K and 293 K, which were 79.6×10^{-20} m^2 and 40.9×10^{-20} m^2 respectively, shows a good agreement for the room temperature measurements but less so for the 20 K data.
It can be seen in the fitted datasets that the time constant does not go to zero when interpolated to zero helium density. This suggests that the ablation process itself puts a significant density of material in the cell through which the YbF and Li have to diffuse. This is in agreement with the results from chapter 5, where the helium density was measured directly at the cell. The offset is smallest for the lithium data at 80 K. Although the reason for this is is not clear, it can be speculated that when the cell is warm, vacuum contaminants such as water and hydrocarbons reach the cell and are absorbed into the target and when the cell is cold, the target absorbs helium just like a cryo-sorb. At 80 K these effects are diminished as it is not cold enough to absorb helium but too cold to let water or hydrocarbons into the cell.
In these experiments the YbF molecules were probed at a frequency that corresponds to the P_1 bandhead in the (0-0) spectrum and therefore incorporates lines from P(3)-P(6) of various isotopes. One may wonder whether the temporal change in the density of these states is influenced by rotational cooling over the timescales used in these diffusion measurements. This would complicate the interpretation of the decay curves and make the diffusion constant measurements unreliable. In section 4.7, we will see that the rotational temperature decreases over the timescale of hundreds of μs. A model that includes both rotational cooling and diffusion shows that the cooling is important at early times but that the decay is dominated by diffusion for later times that are used for fitting. These effects



(a) 293K



(b) 80K



(c) 20K

Figure 4.5: Measured diffusion time constants versus buffer gas density for Li(open circles) and YbF(full circles) at 293 K, 80 K, 20 K

are discussed more thoroughly in section 4.7.1.

4.5 Absorption Images

To investigate the dynamics in the cell further and motivated in part by the behaviour of the loss time constants at higher helium density (as seen in figure 4.5), absorption images of YbF were taken that provide some spatial information on the YbF distribution. The probe laser beam was expanded to a diameter of about 2cm and absorption images were recorded on a CCD camera. The minimum shutter time of the camera was 34 μs. In order to improve this time resolution, the laser beam was sent through an aom and the first order beam was picked off to use as the probe. This allowed fast switching on and off of the beam. The time interval between successive pictures was usually varied between 10-500 μs, depending on whether one wanted to look at the dynamics over a short time or look at the complete decay of the signal. In order to achieve the highest possible absorption signal, the laser was tuned to the band head at a frequency of 542808.7GHz. This means that the images include rotational lines in the range of N=3-6.

4.5.1 Results

It was observed that the inital molecular distribution inside the cell changed with differing helium pressure. If the images were recorded shortly after changing from high to low pressure, it was seen that they retained the characteristices of higher pressures. After waiting for a few minutes, the images looked as expected for lower pressures.Therefore it was important to let the pressure settle for a few minutes after changing it.
The results for absorption images of YbF for three different helium densities can be seen in figure 4.6. The distribution of molecules in the first frame, which captures the first 30 μs in the cell is very different for low and high helium densities. For low helium densities the loading process allows the molecules to spread through the entire cell on a timescale less than the time resolution of these images. However for higher helium densities, the ballistic expansion of the molecules away from the target is arrested before they have filled the cell and so they are confined to a region close to the target. In the subsequent images the molecules can be seen expanding into the rest of the cell, but this expansion is slow, particularly at the highest density. As in the absorption profiles, the molecular density decays faster for very high buffer gas densities and occurs before the molecules have expanded to fill the cell, suggesting that the molecules are diffusing back onto the target, or that there is an extra loss mechanism.

It can also be seen that the maximum of absorption for low densities is not in the first frame but that it takes a few tens of μs for the peak density to arrive. As the absorption images include rotational lines from N=3-6, which become significantly more populated when cooling the molecules down, the increase in absorption signal over the first few frames could be rotational cooling. It is also possible that the reactions to make

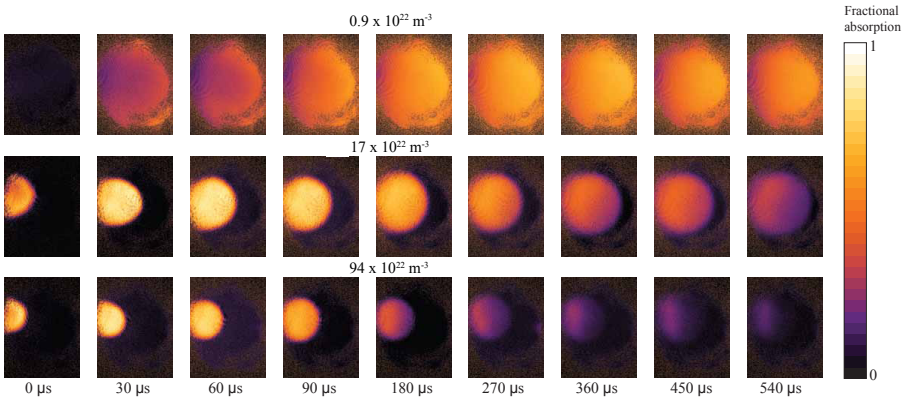


Figure 4.6: Absorption images as a function of time after the ablation pulse for three different buffer gas densities at a cell temperature of 20K. For a helium density of $0.9 \times 10^{22}\mathrm{m}^{-3}$, the size of the observed molecular cloud is limited by the one inch diameter window used for detection.

YbF out of the AlF_3/Yb target take longer at lower buffer gas densities. Although these two processes can not be disentangled, the relatively long time constant associated with the process[3] seems to support rotational cooling as a result of the relatively slowly cooling buffer gas (see also section 4.8).

4.6 Simulating diffusion in our buffer gas cell

As the geometry of the buffer gas cell used for the experiments described in this section is quite complicated, no analytical solution for the spatial diffusion equation 4.10 exists and thus a numerical solution had to be found. This was done using the finite element program Comsol Multiphysics Version 3.2. In order to compare the simulation results with measurements taken in the lab, a timescale of 8 ms with a resolution of 10 μs was chosen. In the experiments the molecules are loaded into the cell via laser ablation. To model the dynamics inside the cell, an appropriate inital condition had to be used. From the first frame of the absorption images (fig. 4.6), it can be seen that there are more or less two different initial conditions depending on the helium pressure inside the cell: For low helium densities, the molecules have spread throughout the entire cell within the first 10 μs, whereas they are confined in a smaller area close to the target for higher helium densities. As diffusion happens on a timescale of the order of ms, ablation dynamics during the first μs can be neglected and those two initial conditions are expected to represent the two extremes of the inital distribution of molecules in the cell. The two different inital distributions of $n(\mathbf{r}, t)$ were therefore taken to be $n(\mathbf{r}, 0) = n_0$ to simulate low buffer gas densities and $n(\mathbf{r}, 0) = n_0 e^{-|\mathbf{r}|/r_0}$ to simulate higher buffer gas densities. $r = 0$ is at the surface of the target and r_0 was chosen to be 1 mm. The 1 mm radius was chosen to match the size of the observed craters produced on the target by the ablation laser.

[3] formation processes are expected to be very rapid

4.6.1 Results

The output of the simulation gives the distribution of YbF density inside the cell at particular times for a specific diffusion coefficient. To compare results from the simulation to

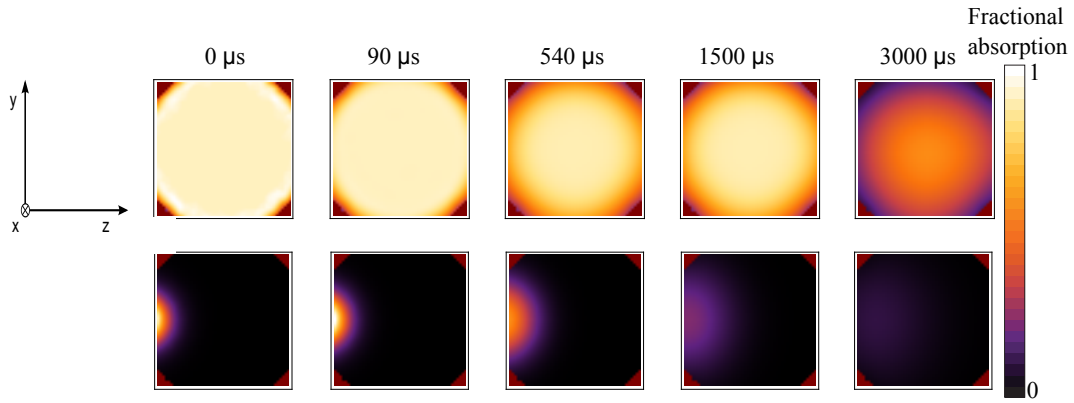
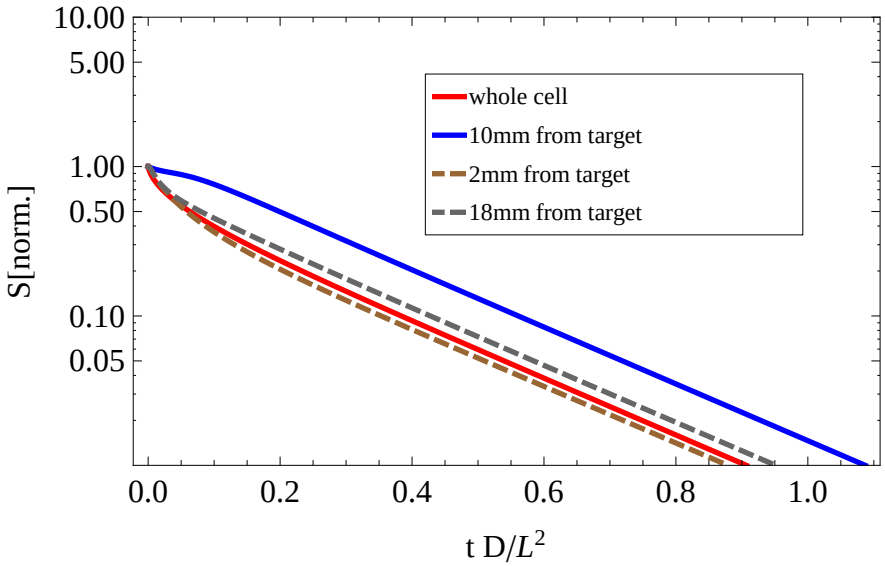
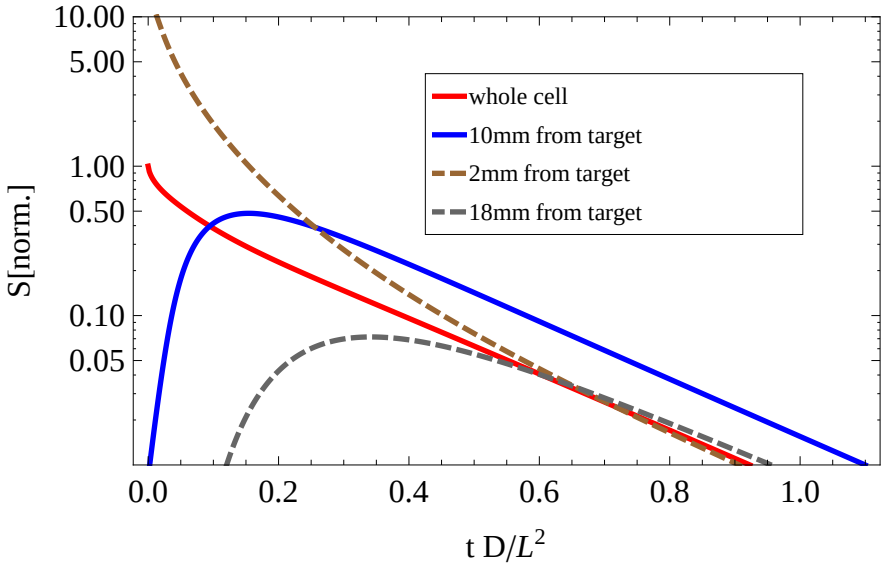


Figure 4.7: Simulated diffusion images for a diffusion constant of 0.005 m^2 s^{-1}. This corresponds to a cell temperature of 20 K, a diffusion cross-section of 80×10^{-20} m^2 and a helium density of 3×10^{22} m^{-3}. a) uniform molecule distribution at t=0. b) localised molecule distribution near the target at t=0, (the image size corresponds to the size of a one inch diameter window, as used in the experiments)

experimental results, the raw simulation data were analysed in two different ways. Absorption images were simulated by integrating the particle density along the x-direction in an area of the y-z plane that corresponded to the position and area of one of the windows in the cell. The results can be seen in figure 4.7, where the initial density is homogeneous in the upper row and concentrated close to the target in the lower row. The helium density is the same in both, but we see that the molecular signal seems to decay more slowly in the upper panel. Thus the more rapid decay observed in the experiments at high density comes naturally from diffusion and does not require additional loss mechanisms postulated in the previous section. The density was also integrated along a line in the x-direction, thereby simulating the absorption profiles obtained by shining a laser beam through the cell and detecting it on a photodiode. These results are displayed in figure 4.8. The four curves show the evolution of this integrated density with time in the case when the inital density distribution is uniform. We see that the position of the probe laser does not make a great difference to the decay dynamics. Looking again at the diffusion equation eqn. 4.10, we see that it can be re-written as $\frac{\partial n}{\partial t'} = \nabla_R^2 n$ where $t' = \frac{Dt}{L^2}$ is a dimensionless time parameter and the spatial derivatives in ∇_R^2 are taken with respect to the scaled distance $R = \frac{r}{L}$. Here L is a characteristic length scale whose exact value is not important. We take L to be 1cm. Using scaled time and length parameters makes it easy to see how the results change with the diffusion constant and the size scale of the cell. In graph 4.8, the time is expressed in the dimensionless form t'. For $Dt/L^2 > 0.1$ the decay follows a single exponential irrespective of probe position. When the initial distribution is localised close



(a) Case of uniform inital density



(b) Initial density localised near the target

Figure 4.8: Variation with time of YbF density (integrated along a line through the cell) at several distances from the target.

to the target however, the observed dynamics are sensitive to the position of the probe laser as shown in figure . If the probe laser is positioned at 2 mm, close to the initial peak molecular density, the intitial decay is very fast compared with that seen at long time. Most of the amplitude initially decays with this fast time constant and only a small fraction of molecules is left to decay with the lowest order time constant. By contrast, the integrated density far from the target, increases initially as the molecules diffuse into the region of the probe laser, then density falls again with the characteristic time constant of long times.

These observations can be explained by population of different diffusion modes as given in eqn. 4.9. The higher order modes, representing more rapid spatial variations of density, decay more quickly in accordance with the diffusion equation. When the cell is uniformly filled, the density rapidly settles into the lowest order diffusion mode which has the longest diffusion time. An initial localised molecular distribution significantly populates higher order diffusion modes that decay away rapidly. Eventually only the lowest order diffusion mode is left. In the experiment the size of this initial molecular distribution depends on the helium density, cell size and ablation power. From a certain helium density onwards and for a fixed ablation power, the ballistic expansion does not manage to fill the whole cell anymore and from then on, the initial molecular distribution gets smaller, as the buffer gas density is increased. Although for higher densities the diffusion coefficient gets smaller, which slows the diffusion down, the initial molecular distribution decreases which drives more rapid initial diffusion. Ideally it would be possible to observe this multi-exponential decay, however in an experiment with a certain amount of noise,it might not be possible to observe the slowest diffusion time which is independent of the initial distribution of the molecules. Therefore the deviation from linearity as seen in figures 4.5 can be explained by the change in inital condition.

To compare the simulation results with the experiment, the tail of the simulated absorption profiles, which always approaches the same time constant, was fitted to an exponential decay. The time constant in s from the diffusion simulations is $\frac{22\times10^{-6}}{D}$, where D is the diffusion constant in units of m^2s^{-1}. Inserting this into eqn. 4.12 the solution for a cubic cell, gives a diameter of about 3 cm which is in good agreement with the size of our cell. This is a good check that the simulations give reasonable time scales. Taking the calculated results for the diffusion cross-sections for lithium from section 4.3.1 and plugging them into equation 4.23 gives time constants for lithium at 20 K, 80 K and 293 K of 1300×10^{-22} μs/m^{-3}, 482×10^{-22} μs/m^{-3} and $171\times10^{-22}\mu$s/m^{-3} respectively. This can be compared to the experimentally obtained gradients of the time constant versus helium density graphs from section 4.4 which are $1022\pm226\times10^{-22}\mu$s/m^{-3}, $489\pm48\times10^{-22}$ μs/m^{-3} and $79\pm2\times10^{-22}$ μs/m^{-3} for 20 K, 80 K and 293 K respectively. It is surprising that the results agree very well for the 20K and 80K data but not so well for the room temperature data. It is assumed that the helium density is best known for the room temperature data as there are no thermal transpiration effects that need to be considered and the helium density was directly measured at the cell as explained in section 5. A possible error could

be in the calculation of the lithium diffusion cross-section at 293 K but not at 80 K and 20 K, however that seems to be unlikely. Hence there appears to be a systematic error that is dominant at room temperature or there may be a systematic offset that is similar for all the temperatures but is only noticeable at 293 K where the measurement is most precise.

4.7 Temperature Measurements

When trying to cool molecules, it is important to know what temperature can be reached. In particular, we would like to know how well the translational and rotational degrees of freedom thermalise to the cell temperature, and on what time-scale.
The translational temperature can be obtained from the Doppler broadening of an isolated spectral line. If homogenous and inhomogenous widths are of similar magnitude, the spectra are fitted to Voigt profiles (sec. 3.2). If the $1/e$ half-width of the Gaussian component of this profile, in frequency units, is σ_{D}, the translational temperature is given by:

$$T = \frac{(\lambda\sigma_D)^2 m}{k_B} \tag{4.28}$$

Unfortunately there are no isolated lines in the spectrum of YbF. As can be seen clearly in chapter 3, the spectrum is complicated by hyperfine components, that are separated by the same order as the expected Doppler linewidth and by components from other isotopes. Nevertheless, we can use the saturated absorption method to resolve the hyperfine components. The Doppler-broadened line can then be fit to a Multi-Voigt model, where the centre-frequency of each component is fixed (from the saturated absorption spectrum), and single Lorentzian and Gaussian widths, common to all components are used in the fit. Then the fitted Gaussian width once again determines the temperature. An example of this procedure is shown in fig. 4.9, which is a four component Voigt fit to the Q(7) line, along with the associated saturated absorption spectrum.

It was observed that the translational temperature depended on the time at which the absorption was measured. Figure 4.9 shows spectra taken of the Q(7) transition 200 μs and 2000 μs after the ablation pulse. A cooling from about 75 K-20 K can clearly be observed as the linewidth decreases and partly-resolved hyperfine features appear. To investigate the time dependence of the translational temperature further, the absorption profile was gated in steps of 100μs, with a bin size of 100 μs, starting 100 μs after the ablation pulse. The translational temperature was evaluated for each of these spectra.
Because the translational temperature evolved over time, a similar analysis was done for the rotational temperature by comparing the intensity of rotational lines Q(4)-Q(12). For these measurements it was particularly important to have the normalisation beam locked to the Q(0) transition to factor out the ablation yield. The relative populations determined from the area of the Doppler profile, taking the different line strengths (appendix. A) into account. These were then plotted against the rotational quantum number N. The

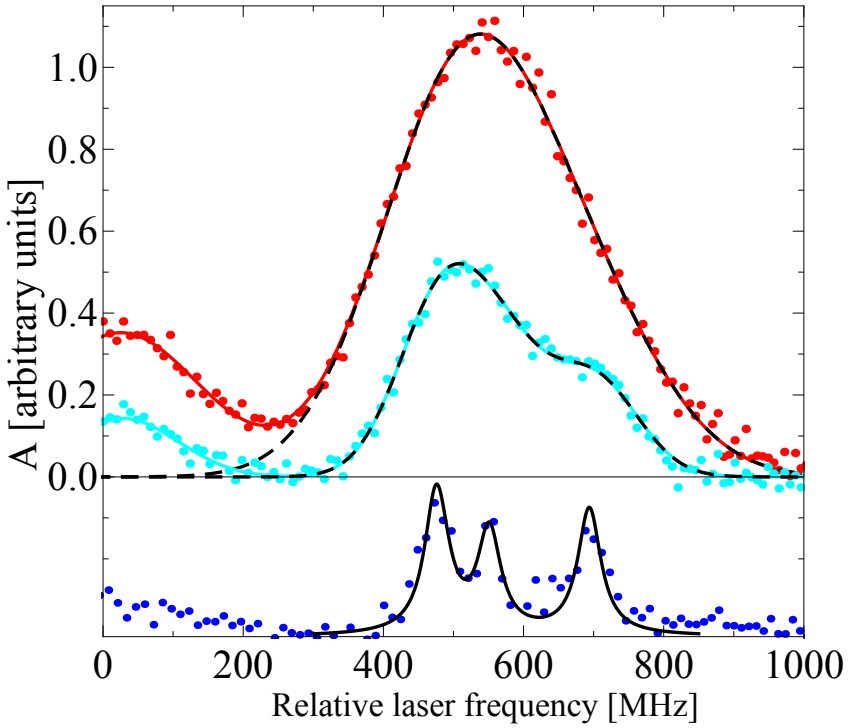


Figure 4.9: Absorption spectrum of the Q(7) line obtained 200μs (red) and 2000μs(blue) after the ablation pulse (above) fitted to Voigt profiles and a saturated absorption spectrum recorded simultaneously showing its hyperfine components (below).The cell temperature is approximately 20K

molecular population of rotational levels (within one vibrational level) can be described by a Boltzmann distribution, where the rotational energy is $E_{\text{rot}} = BN(N+1) - DN^2(N+1)^2$, with B being the rotational constant and D accounting for centrifugal distortion. Hence the populations can be fitted to

$$P(N) = (2N+1)e^{-\frac{BN(N+1)-DN^2(N+1)^2}{k_B T}} \tag{4.29}$$

To look at the temporal behaviour of this temperature as well, the absorption on all these lines was gated in steps of 200 μs with a bin size of 200 μs. Figure 4.10 shows the rotational populations at times 400 μs and 2000 μs after the ablation. At the later time there is a clear shift of the peak population to lower rotational levels, indicating rotational cooling from about 35 K to 20 K.

4.7.1 Results

The results for the time dependent translational and rotational temperature are displayed in figure 4.11. This shows significant cooling which occurs on two separate time-scales. The translational and rotational temperatures are nearly the same at all times. In order to

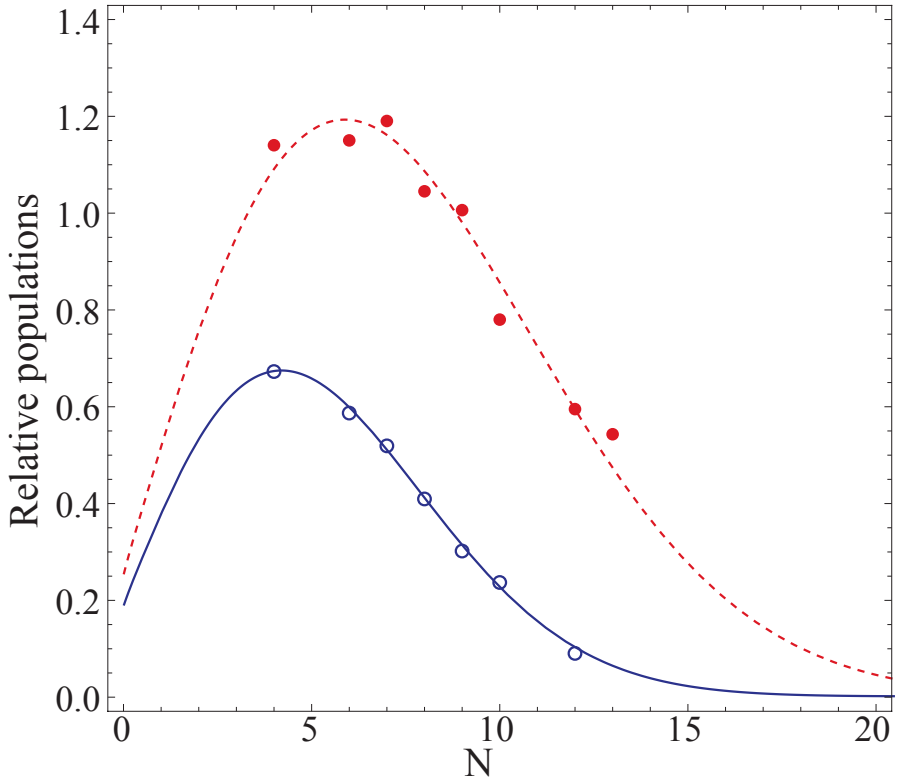


Figure 4.10: Relative populations of Q-branch transitions from different rotational levels N at 400μs after ablation (filled points) and 2000μs after ablation(open points) fitted to Boltzmann distributions with the rotational temperature as a free parameter. The cell temperature is approximately 20K and a helium density of $0.9 \times 10^{22}\mathrm{m}^{-3}$ is used

understand what the cooling of the molecules corresponds to, one has to find an appropriate model to fit to the data. The first idea is to fit the data to a simple hard sphere model of cooling with a temperature independent cooling rate R and a buffer gas temperature T_{bg}:

$$\frac{dT}{dt} = R(T - T_{\mathrm{bg}})/\kappa \tag{4.30}$$

$$T = (T_0 - T_{\mathrm{bg}})e^{-\frac{Rt}{\kappa}} + T_{\mathrm{bg}}, \tag{4.31}$$

where $\kappa = \frac{(m+M)^2}{2mM}$. However it is obvious that the data do not support a simple exponential decay. The model can be made more realistic by assuming that the buffer gas is heated up slightly during ablation and then cools back down over time to the temperature of the cell walls (T_c). This effect is plugged into eqn. 4.31 by making the buffer gas temperature time dependent with a characteristic cooling time constant τ_{bg}:

$$T_{\mathrm{bg}}(t) = (T_{\mathrm{bg0}} - T_c)e^{-\frac{t}{\tau_{\mathrm{bg}}}} + T_{\mathrm{c}} \tag{4.32}$$

Furthermore as the molecules cool down they become slower and hence the cooling rate R has to change as well. The rate is also dependent on the helium density n_{He} and the YbF-He

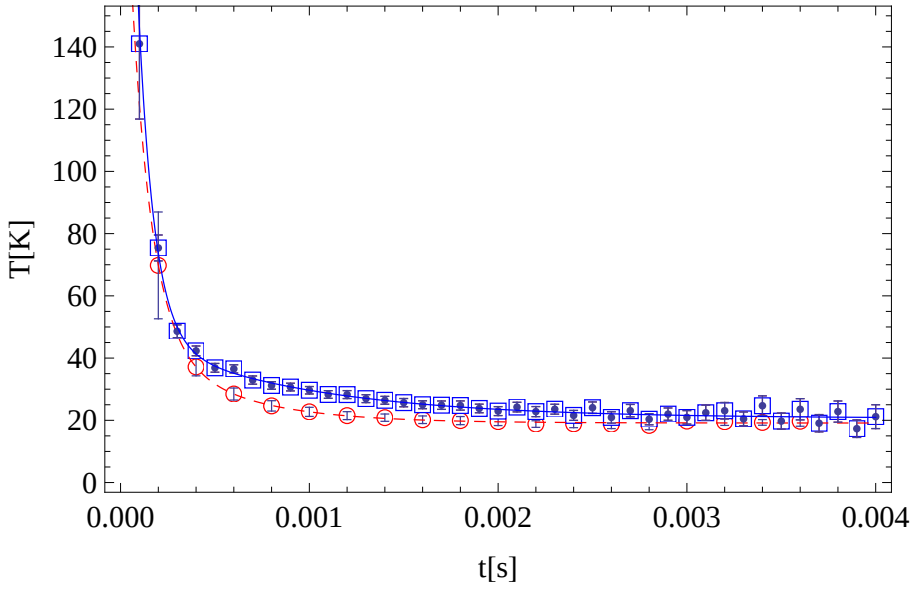


Figure 4.11: Translational (blue squares) and rotational (red circles) temperature versus time after the ablation pulse for a buffer gas density of $0.9\times10^{22}\mathrm{m}^{-3}$ and a cell temperature of 20 K as measured with thermometers on the cold plate

Table 4.1: Results for fitting translational and rotational temperatures as a function of time using eqn. 4.33 with eqn. 4.32

Fit parameter	T_{trans}	T_{rot}
$T_0[K]$	400 ± 200	400 ± 700
$T_{\mathrm{bg0}}[K]$	48 ± 4	50 ± 36
$T_{\mathrm{c}}[K]$	21 ± 1	19.1 ± 0.1
$\tau_{\mathrm{bg}}[s]$	0.00092 ± 0.00018	0.00046 ± 0.00025
$b=\sqrt{\frac{8k_{\mathrm{B}}}{\pi u}}\frac{n_{\mathrm{He}}\sigma}{\kappa}[Jkg^{-1}K^{-1}m^{-1}]$	3700 ± 550	3500 ± 3100

cross-section σ, which is for now assumed to be temperature independent, as $R = n_{\mathrm{He}}\sigma_D\bar{v}$. In order to include this rate in equation 4.30, the velocities of the two species are added in quadrature, giving:

$$\frac{dT}{dt} = -\sqrt{\frac{8k_B}{\pi}}\sqrt{\frac{T}{M}+\frac{T_{\mathrm{bg}}}{m}}n_{\mathrm{He}}\sigma\frac{(T-T_{\mathrm{bg}})}{\kappa} \tag{4.33}$$

Integrating this equation and fitting it to the datapoints yields a good fit with the parameters [4]displayed in table 4.1.

The fitted values of the parameter b in the table, give the thermalisation cross-sections. They are $(7.2\pm1.1)\times10^{-20}$ m^2 for the translational temperature and $(7\pm6)\times10^{-20}$ m^2 for the rotational temperature. As the cross-section obtained from the translational temperature data should be similar to the diffusion cross-section of YbF through helium it is expected to be about an order of magnitude higher than these values (section 4.4). This

[4] u here is the atomic mass unit

suggests that, on the timescale observed in these experiments, the molecules are always in thermal equilibrium with the helium, and it is in fact the cooling of the helium that we observe in the data. As the ablation happens, heat is dumped into the buffer gas in a localised region around the target. Hot helium then mixes with cold helium causing the temperature to drop rapidly until the entire buffer gas is in equilibrium at an intermediate temperature, higher than the cell walls. The buffer gas then comes back into equilibrium with the cell walls on a timescale reflected in a second, longer time constant. Hence this model describes heat conduction through the cell using two modes, analogous to the diffusion modes described earlier (section 4.2) and the fit function used is:

$$T = A_1 e^{\frac{-t}{\tau_1}} + A_2 e^{\frac{-t}{\tau_2}} + T_\mathrm{c} \tag{4.34}$$

The fit results are displayed in table 4.2. This shows that the cell sits at a temperature of about 20K and the longer time constant is $460 \pm 220\mu$s. These results seem reasonable when comparing with estimated heat conduction times. The heat equation is analogous to the diffusion equation given as [107]:

$$\frac{\partial T}{\partial t} = \frac{k}{c_\mathrm{p}\rho}\nabla^2 T, \tag{4.35}$$

where k is the thermal conductivity of the gas, c_p is the specific heat capacity and ρ its density. From equation 4.12, we know that the lowest order diffusion time constant for a cube is given by $\tau = \frac{a^2}{3\pi^2\alpha}$, where $\alpha = \frac{k}{c_\mathrm{p}\rho}$ is the thermal diffusivity (analogous to the diffusion coefficient) and has units of $\mathrm{m^2 s^{-1}}$. The thermal conductivity of helium at 20 K is 26×10^{-3} W m^{-1} K^{-1} [108]. The specific heat capacity is 5193 J K^{-1} kg^{-1}. Putting these numbers into the above equation gives, for a helium density of 0.9×10^{22} m^{-3}, a lowest order time constant of about 360 μs, in good agreement with what is observed in the experiment. The cell temperature T_c comes out about 7 K higher than measured by the themometers attached to the cold plate. Some temperature difference is not surprising though because the cell is made of aluminium and because the heat link between cold plate and cell is not perfect. Therefore it is assumed that the temperature obtained from these measurements is correct and this method is henceforth used to determine the temperatures when required. An increase of buffer gas temperature due to the ablation process and subsequent cooling has also been noted in references [8],[109] which suggests that this is a common feature when using this loading technique. If we were to assume that the whole energy from ablation, which is typically about 50 mJ is transferred into helium buffer gas with a typical number density of $10^{22}\mathrm{m}^{-3}$, the rise in temperature would correspond to 8000 K. Usually most of the energy is absorbed by the target but it shows that the particles that are deposited into the buffer gas can indeed heat up the gas as seen in the above measurements. For cold molecular beams it is therefore important to make sure that the buffer gas has time to cool back down before the molecules leave the source.

Table 4.2: Results for fitting translational as well as rotational temperature as a function of time using eqn 4.34

Fitparameter	T_{trans}	T_{rot}
T_{c}	20.6 ± 0.9	19.1 ± 0.5
$A_1[K]$	300 ± 100	200 ± 300
$A_2[K]$	28 ± 3	32 ± 31
$\tau_1[s]$	0.000084 ± 0.000014	0.000107 ± 0.000093
$\tau_2[s]$	0.00088 ± 0.00016	0.00046 ± 0.00022

Effects of cooling of buffer gas after ablation on diffusion cross-section measurements

Knowing that the buffer gas cools after inital heating with a time constant of a few hundred microseconds, it has to be investigated whether this effect influences the diffusion times obtained in section 4.4. Because the molecules are essentially in thermal equilibrium with the buffer gas, the rotational population is given by equation 4.29, where T is now dependent on time and given by equation 4.34 with the fit parameters displayed in table 4.2 as known for the particular helium density 0.9×10^{22} m^{-3}. The fraction of population contributing to the bandhead, where the diffusion measruements were made, is found by normalising the population of rotational lines 3-6 to the population in all rotational lines. The equation which shows the effect of diffusion and rotational cooling on the particle density is then:

$$P(t) = P_{3-6}(t)e^{\frac{-t}{tau_{\mathrm{D}}}} \tag{4.36}$$

Producing artificial data using this formula and fitting the tail to a single exponential decay, gives an estimate of how much the fitted time constant can deviate from the actual diffusion time constant. This procedure is shown in figure 4.12 with the theoretical YbF-He diffusion time constant $\tau_{\mathrm{D}} = 1.628$ ms at a density of 0.9×10^{22} m^{-3} at which the cooling time constants for the buffer gas are known. The data in the tail are then fitted to an exponential starting from 0.5ms,1ms and 2ms. These fits overestimate the diffusion constant by 16%, 5% and <1% respectively. If the time constants from many such fits are plotted as a function of these starting times, the resulting curve is an exponential decay with a time constant as expected of the order of the longer cooling time from equation 4.34.

The cooling of the buffer gas over time also has an effect on the translational temperature. As the diffusion coefficient is proportional to the thermal velocity (eqn. 4.23, the time constant becomes a function of time. In order to look at the theoretical significance of that effect, the constant factor $D\tau_{\mathrm{D}} = 0.22 \times 10^{-4}$ is obtained from the diffusion simulation and the τ_{D} in equation 4.36is then replaced by:

$$\tau_{\mathrm{D}}(t) = 0.22 \times 10^{-4} \frac{16}{3} n_{\mathrm{He}} \sigma_{\mathrm{D}} \sqrt{\frac{\mu}{2\pi k_B T(t)}} \tag{4.37}$$

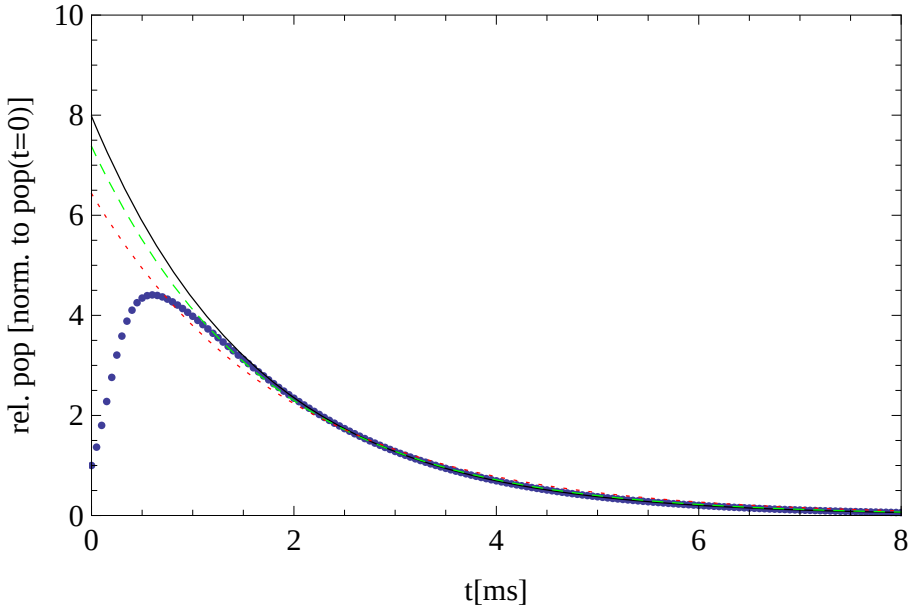


Figure 4.12: Population in rotational levels N=3-6 as a function of time [in ms] normalised to the population in these levels at t=0 considering rotational cooling and diffusion through the buffer gas. The three fits are single exponential decays starting 0.5 ms(red,dotted), 1 ms(green,dashed) and 2 ms(black, through line) after the ablation pulse

Using the calculated value of the diffusion cross-section for YbF, synthetic data are created that incorporate both rotational cooling and a time dependent diffusion coefficient. These are fitted to a single exponential. The time constant resulting from the fit is then compared to the theoretical time constant for YbF of 1.628 ms at a temperature of 20 K and buffer gas density of 0.9×10^{22} m^{-3}. This shows that when fitting from 0.5 ms,1 ms and 2 ms onwards the time constant is overestimated by 25%, 11% and 4%. However the same analysis applied to real experimental data shows that from 0.32 ms onwards, where the fits were gated for the liquid helium data, the time constants change up to 10% but do not show a consistent trend as proposed by the above model. Therefore no systematic error has to be accounted for in the data and the 10% variations are in agreement with the assigned errorbars of the time constants.

4.8 Summary and conclusions

In this section the dynamics of YbF molecules in a buffer gas cell have been investigated. Table 4.3 summarizes the main results on cross-sections and time constants. The diffusion times of YbF and lithium were measured as a function of helium density. This showed the expected linear increase for lower helium densities from which the diffusion cross-section can be obtained. At higher buffer gas densities onwards it was seen that the time constants flatten off. This has been observed by other groups as well [110], [8]. Sushkov et al. [110], measure the diffusion times of silver, gold, lithium and rubidium. All species show a similar behaviour: the time constants level off and then decrease with increasing

helium density. The alkalis seem to be affected in this way at a lower helium density. The flattening off in our experimental data occurs at lower helium density for lower temperature. This is similar to the observation in reference [110] where the highest time constant is measured at 120 K rather than 32 K. The authors suggest that possible mechanisms that decrease the time constant for higher buffer gas densities are dimer formation of the atoms or capture by clusters or impurities produced during the ablation process. In order to investigate this behaviour, diffusion simulations of our buffer gas cell were performed as well as absorption images taken to gain spatial information of the diffusion process. The absorption images show that for low pressures the molecules spread throughout the whole cell right after the ablation whereas for higher pressures they stay confined to an area close to the target. In the latter case, it seems as if the density decays faster than for lower pressures. Simulations of diffusion in the cell using these two initial conditions(a homogeneous distribution throughout the cell and a molecular density confined to the target region) showed a similar behaviour to the experimental absorption images. The modelling of the experiment shows that the diffusion is initially more rapid when the molecules are localised near the target than when the cell is filled homogeneously. In the former case the decay curves depend strongly on the probe position with the main fraction of the density decaying much faster when the probe is close to the target. This observation, together with the insights obtained from the absorption images, suggests that the flattening off of the time constant for higher buffer gas densities is due, at least in part, to the inital confinement close to the target.

The diffusion cross-section for YbF was calculated and measured at 20 K and 293 K as listed in table 4.3 and the measurements are in agreement with the calculations. The calculation is based on the potential energy surface calculated in [106] and our experiments are the first test of that potential. The measurements are performed with respect to the reference atom lithium for which the potential and cross-section is well known. This means that the measurements do not require a precise knowledge of the helium pressure or of solutions of the diffusion equation in the cell(which for our more complicated geometries had to be found numerically). Thermal transpiration plays a role in the pressure regime of buffer gas cells as shown in 2.2.1. The corrected density can deviate up to 60% depending which empirical formula is used, for buffer gas densities commonly used. The method of obtaining the diffusion cross-section by measuring the gradient of the diffusion time versus helium density is regularly used [111],[8],[112],[113],[110]. Uncertainties associated with this method have been discussed in this chapter. The possible effects of probe position on obtained time constants and the difficulty in determining the precise helium density show that it is important to have a reference atom that is detected in the same region of the cell.

Further on calculated and measured diffusion times were compared for lithium and show good agreement for 20 K and 80 K but not for 293 K, even though the helium density is best known for that temperature. This underlines that it is very hard to have a good knowledge of the exact conditions in the cell and that it can therefore be advantageous to

Table 4.3: Comparison of theoretical and experimental results for diffusion cross-sections for Li and YbF and diffusion time constants for Li

T (K)	$\bar{\sigma}_{\text{D,Li-He}}$ (th.) ($10^{-20}m^2$)	$\bar{\sigma}_{\text{D,YbF-He}}$ (th.) ($10^{-20}m^2$)	$\bar{\sigma}_{\text{D,YbF-He}}$ (exp.) ($10^{-20}m^2$)	$\tau_{\text{Li}}/n_{\text{He}}$ (th.) ($10^{-22}\mu s/m^{-3}$)	$\tau_{\text{Li}}/n_{\text{He}}$ (exp.) ($10^{-22}\mu s/m^{-3}$)
293	35.8	40.9	41 ± 4	171	79 ± 2
80	51.9	55.8	-	482	489 ± 48
20	71.0	79.6	203 ± 75	1300	1022 ± 226

measure cross-sections using a reference atom for which the cross-section is well known. This takes the helium density and knowledge about the diffusion mode out of the equation (eqn. 4.27).

Measuring the temperature of the molecules in the cell, cooling was observed on a timescale of 1 ms. This is attributed to cooling of the helium after it has been heated up by the ablation process. The cooling has two time constants, of which the longer one is on the order of a few hundred microseconds (see table 4.2). Thermalisation of the molecules with the helium is thought to occur on a timescale faster than the time resolution of the experiment. Although we can see the effect of rotational cooling in the absorption images, it was shown that when fitting only the late tail of the absorption profiles, these effects do not significantly influence the obtained diffusion times.

Chapter 5

Experimental Set-up II

5.1 The Buffer Gas Molecular Beam Apparatus

The cryostat 5.1 in this set-up is built around a SRDK-415D cryocooler with a F-50H compressor unit from Sumitomo Heavy Industries Ltd. It has two cooling stages, of which the first has a rated cooling power of 35 W at 50 K. Though it is referred to throughout this thesis as the 50 K stage, it can reach a minimum temperature of about 30 K at very low heat loads. The second cooling stage has a rated cooling power of 1.5 W at 4.2 K and a minimum temperature at zero heat load of about 2.2 K. The cold head is installed pointing upwards as opposed to the arrangement described in sec.2.

The whole apparatus is housed in a custom made vacuum chamber to limit heat conduction by gas from room temperature surfaces to the cold surfaces. The chamber is based on ISO250 tubing which can be seperated in the middle to allow better access to the cold head. The chamber is evacuated by a Leybold turbovac 361 turbomolecular pump with a backing pump (Leroy Somer LS90PR/T). The pump is mounted on the lower half of the vacuum chamber besides four KF ports and two electrical feed-throughs. The guard vacuum can be monitored on a Leybold PR27 Penning gauge mounted on one of the KF40 ports. The electric feed throughs are used for connections to thermometers, two heaters and a pulsed gas valve. All but one of the themometers are homemade ruthenium oxide temperature sensors using Rohm 1206 surface mount resistors of 1 kΩ and 1.5 kΩ resistance at room temperature [114],[115]. They were calibrated to a Lakeshore Cernox CX-1050-CH-1.4D thermometer, which is also used to measure the cold plate temperature.

On the upper half, eight KF25 and eight KF40 ports were welded to the chamber, to mount windows for optical access. This is needed to produce the molecules in the cell by laser ablation and to detect them using laser-induced fluorescence and absorption spectroscopy. Four windows each are mounted at four different heights and are alternating 25 mm and 40 mm wide. The 40 mm windows have been chosen to allow efficient fluorescence collection while the 25 mm windows allow laser beams through and therefore do not need to be so big. The windows are anti-reflection coated in the visible to reduce background scatter and the window for the ablation laser is anti-reflection coated in the infrared. A further

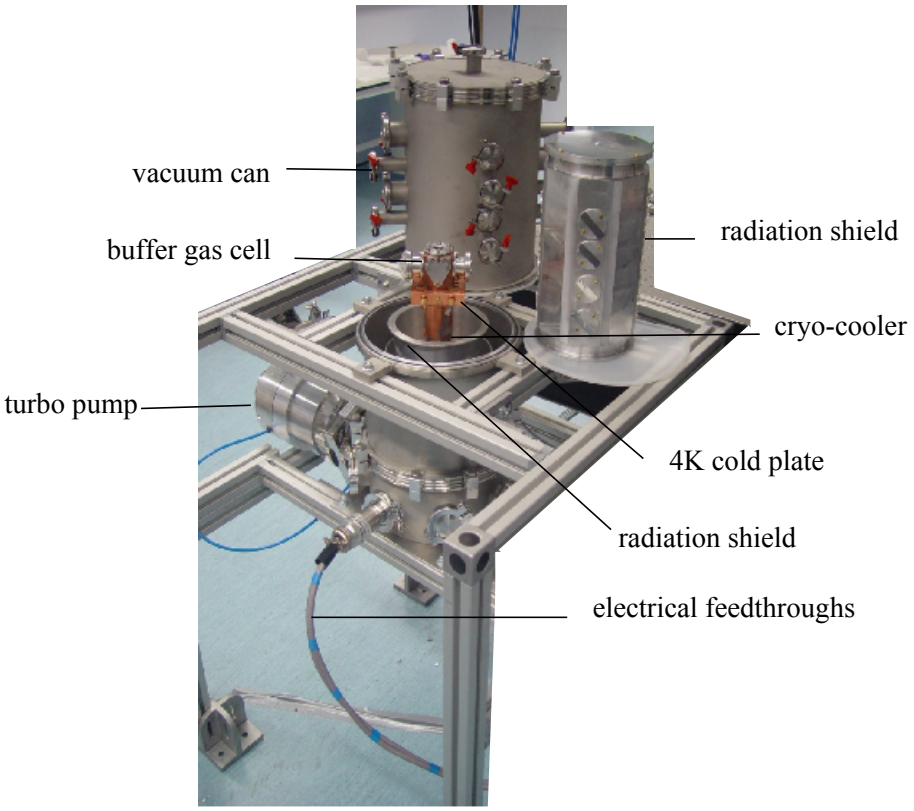


Figure 5.1: Picture of the molecular beam apparatus, indicating some of the important components

40mm window provides optical access through the top of the vacuum chamber.
As blackbody radiation from room temperature surfaces can transfer heat to the 4 K cold stage, a radiation shield is mounted on the 50 K stage of the cryocooler. This is made out of aluminium, which is easy to machine and has relatively good thermal conductivity at low temperatures. It is manufactured in a way to allow no direct line of sight from the outer vacuum can to the cold plate while still leaving enough conductance to ensure the fast pump-out of the cryostat. Its windows are aligned with those of the outer vacuum can and are also appropriately anti-reflection coated.
The radiation shield surrounds the 4 K copper cold plate which is mounted on the 4K cold head and accommodates the experimental set-up. On this plate, the buffer gas cell, the imaging set up and the charcoal sorption pumps are mounted. Thermometers measure the temperatures of the buffer gas cell and cryopumps. Two heaters mounted on the cold head allow a fast warm-up of the cryostat. Two 2 mm diameter gas lines coming in from the outside are made of stainless steel for most of the way. As they reach the 50 K plate,

they are connected to copper pipes that make a few windings and are bolted to the plate with M4 screws. This ensures that most of the heat load from the gas is dumped onto the 50 K plate, which has the higher cooling power. The copper tubing then changes back to stainless steel until the second 4 K cold plate is reached, where it connects to another copper tube that is thermally anchored to the cold plate to ensure thermalisation of the helium gas before it flows into the cell. All wires that enter the cell are also heat sunk to the 50 K plate first to minimise heat conduction onto the 4 K plate.
Computer control described in chapter 2 also serves this apparatus.

5.1.1 The buffer gas cell

The buffer gas cell is made out of copper to ensure good thermal conductivity and is mounted on a 10 mm thick round copper base plate with a diameter of 130 mm, which is itself screwed onto the cold head of the cryocooler. A simple geometry was chosen, to make it easier to model dynamics inside the cell. The main body of the buffer gas cell is a cube of side 50 mm with 10 mm thick walls, giving an internal volume of $30 \times 30 \times 30$ mm^3 (see figure 5.2. It was manufactured by welding a 10 mm thick copper plate onto a

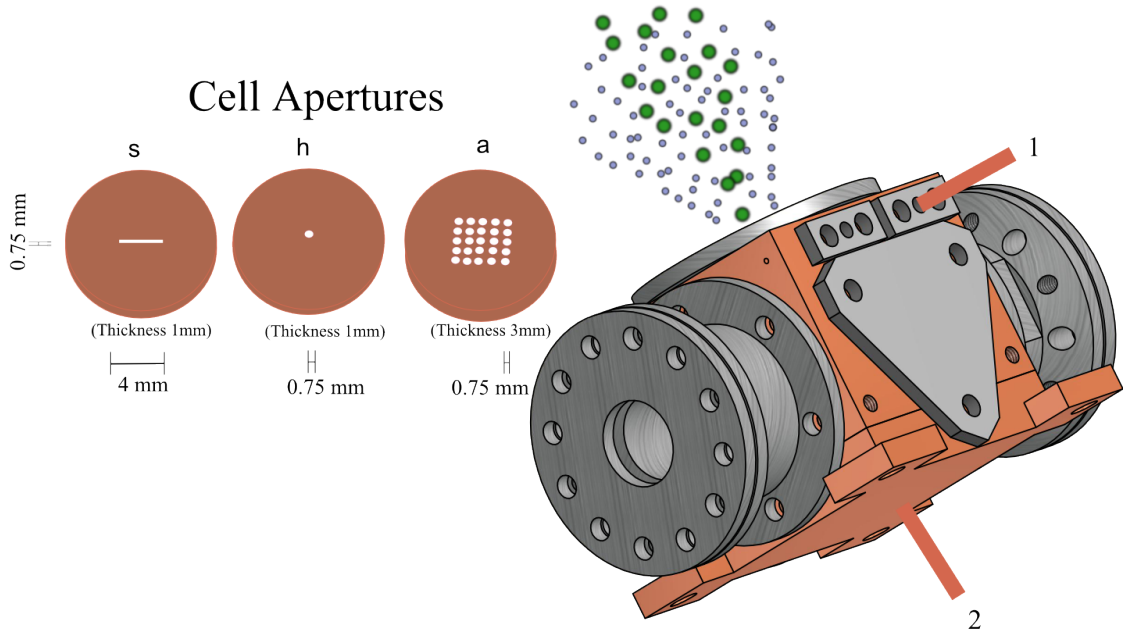


Figure 5.2: Buffer gas cell with different cell apertures and different positions of helium inlet tube are indicated.

cube which was hollowed out. The welded joint was found to be porous and was therefore covered with Stycast 2850FT mixed with 24LV catalyst to ensure that there were no air leaks. Three sides of the buffer gas cell have windows for optical access and the ablation target is attached to one of its sides. As in the other apparatus (see ch. 2), a vacuum-hot-pressed Yb/AlF_3 disk was used as the ablation target. The top side of the cube allows different copper apertures to be inserted for molecular beam extraction. In the apparatus

of chapter 2, the side windows became coated during ablation. This coating attenuated the probe beam and made it necessary to clean the windows after a few weeks of running the experiment. To avoid this problem with the new cell, the two side windows were moved awaf from the cell by 15 mm long window holders made from aluminium. All metal-metal and glass-metal vacuum seals were made using indium wire. A relatively high pressure is required to form a leak tight indium seal between two surfaces. In order to obtain this without applying large forces to the glass windows, we use a technique similar to that described in [116]. Indium wire is pressed between two narrow interlocking metal ridges and forms a seal with the outside edge of the glass window. The cell has three helium inlet tubes. The helium source and a return line can be connected to any of the three inlets. The unconnected inlet is blanked off. Initially both of the gas lines entered the cell just above the target (source line at position 1 in figure 5.2). One of the lines was subsequently moved to enter through the bottom face (position 2 in figure 5.2) of the cell. Having inlets at different places with respect to the ablation target, makes it possible to observe different extraction dynamics as explained in chapter 6. All gas lines have an inner diameter of 2.5 mm, however for the two lines coming in right above the target, the flow is slightly restricted by the 1mm orifices inside the cell to which the two gas lines are connected.

5.1.2 Helium pressure and maintaining good guard vacuum

To maintain a controlled helium flow into the cell, an MKS 1179A flowmeter was installed between the room temperature helium gas reservoir and the vacuum feedthrough. The flow $F(T)$ can be regulated from 0 to 22 sccm (standard cubic centimeters per minute) in steps of 0.02 sccm. Having a fixed mass flow and knowing the cross-sectional area of the aperture A as well as the mean velocity of helium atoms inside the cell $\bar{v}$, makes it possible to estimate the cell pressure. For most of the experiments in this thesis, a slit aperture with dimensions 0.75×4×1 mm ($w \times l \times h$) was chosen (see figure 5.2). The average pressure in the cell for effusive flow at a particular temperature T_{cell} is then given by [1]:

$$p_{\text{cell}} = \left(F[\text{sccm}] \times \frac{10^{-6}}{60} \times \frac{101325}{293\,K}\right) \frac{4}{A\bar{v}} T \tag{5.1}$$

In order to not conduct heat from the radiation shield onto the cold plate, a good guard vacuum has to be maintained. This is achieved by the use of charcoal sorption pumps. They are home made by sticking charcoal grains on copper sheets using a thin layer of Stycast 2850FT with catalyst 24LV. This combination is especially suitable for low temperatures and compared to other epoxies has a good thermal conductivity of 1.0144 W/(mK). The charcoal covered sheets are screwed onto the cold plate and surround the cell and imaging set-up. The side facing the radiation shield is covered with reflective tape. A good thermal link between the sheets and the cold plate is very important to ensure that the charcoal pumps sit at a low temperature. The temperature at which the pumps start

[1] if units are not indicated they are SI-units

adsorbing helium efficiently is estimated to be about 8 K, as measured using ruthenium oxide thermistor while running the experiment. After a few hours of continuous helium flow, the pumps saturate and release enough helium to conduct heat from the radiation shield onto the cold plate. This heats up the charcoal sheets further and all the helium is released from the sorption surfaces and pumped away by the turbopump. After about ten minutes, all the helium has been pumped away, the charcoal sheets cool back down and the experiment is fit to run again. The highest guard vacuum measured on the Penning gauge while the experiment is running is a few 10^{-5} mbar far from the beam region and the sorption pumps.
As the helium flow F into the cell is controlled using a flowmeter and the guard vacuum is measured using a Penning gauge p_{gv}, the pumping speed of the charcoal sorbs S_{charcoal} can be estimated to be around 20000 l/s using

$$S_{\mathrm{charcoal}}[l/s] = \Big(F[\mathrm{sccm}] \times \frac{10^{-3}}{60} \times 101325\Big)\frac{1}{p_{\mathrm{gv}}} \tag{5.2}$$

5.2 The Probe Laser Systems

The probe laser system for the experiments described in this part of the thesis consists of a frequency doubled Koheras Boostik fibre laser, which produces 900 mW at a centre frequency of 1104 nm with a narrow linewidth and high frequency stability. It can be thermally tuned over a range of 111 GHz and can be scanned more than 3 GHz by applying an external voltage to the fibre piezo. This is frequency doubled to produce light at 552 nm. One doubling set-up uses a resonant optical cavity to increase the intensity of the 1104 nm light in the doubling crystal, and hence obtain a large conversion efficiency. The other setup uses a single pass through a periodically poled (PP) crystal. The latter produces less 552 nm light, but has the advantage of better stability and significantly less amplitude noise.

5.2.1 Frequency Doubling

The electric susceptibility χ of a material is a measure of how easy it is to polarise it in an electric field. The polarisation $\mathbf{P}$ of a material with a nonlinear susceptibility subject to an electric field $\mathbf{E}$ can be written as an expansion in powers of the electric field

$$\mathbf{P} = \epsilon_0(\tilde{\chi}^{(1)}\mathbf{E} + \tilde{\chi}^{(2)}\mathbf{E}^2 + \tilde{\chi}^{(3)}\mathbf{E}^3 + ...) \tag{5.3}$$

where $\tilde{\chi}^{(k)}$ is the kth-order susceptibility tensor of rank k+1. Consider a material driven by a field $\mathbf{E} = E_0\cos(\omega t - \mathbf{k}(\omega)\cdot\mathbf{r})$ (with the wave-vector $\mathbf{k}$ and position $\mathbf{r}$) at frequency ω. The oscillating polarisation re-radiates light, which therefore has the same frequency components as the polarisation. Since $\cos^2(\omega t) = \frac{1}{2}(\cos(2\omega t)+1)$, a large $\chi^{(2)}$ can produce a strong second harmonic.

At every point, inside the crystal, energy from the fundamental wave with frequency

ω is transferred into a wave of frequency 2ω with a well defined relative phase. Maximum conversion efficiency requires all the newly generated light to interfere constructively. This requires the wavevectors to satisfy the phase matching condition

$$\Delta k = \mathbf{k}(2\omega) - 2\mathbf{k}(\omega) = 0 \tag{5.4}$$

However due to dispersion within the crystal, which for all optically transparent crystals means that the refractive index increases with frequency, the phase matching condition (eqn. 5.4) is not satisfied, one way to solve this problem is birefringent phase-matching. In that case, the change in refractive index with polarisation can compensate for the dispersion in the crystal. A beam of light incident on a uniaxial crystal experiences birefringence if not propagating along the optical axis. The crystal used in our experiment is negatively birefringent meaning the extraordinary index of refration n_{eo} is smaller than the ordinary one n_{o}. Type I phasematching is used for the laser set-up in this thesis, which means that both ω waves travel as ordinary waves while the 2ω wave propagates as the extraordinary wave with a polarisation perpendicular to the fundamental one. The phase matching condition is now $n_{\mathrm{o}}(\omega) = n_{\mathrm{eo}}(2\omega)$, which is achieved by an angle of incidence of $\Theta = 90^{\circ}$ and by matching the refractive indices for a particular wavelength by setting the temperature of the crystal appropriately.

Conversion Efficiency

The intensity of the second harmonic wave is optimised by tuning the temperature of the crystal to minimise the phase mismatch $\Delta n = n(\omega) - n(2\omega)$. If all microscopic contributions of $\mathrm{d}E(2\omega, z)$ generated by $P(2\omega, z)$ are integrated over an interaction length L, it can be shown that the conversion efficiency of the second harmonic beam depends on the imperfect phase matching Δk as [117]:

$$\eta_c \propto \frac{\sin^2(\Delta k L/2)}{(\Delta k L/2)^2} \tag{5.5}$$

If the length L exceeds the coherence length L_c

$$L_c = \frac{\pi}{\Delta k} = \frac{\lambda}{4(n_{2\omega} - n_{\omega})}, \tag{5.6}$$

the intensity of the second harmonic wave starts decreasing again due to destructive interference. Therefore the difference $n_{2\omega} - n_{\omega}$ has to be sufficiently small to ensure the coherence length is longer than the length of the crystal. The useful length is also limited by the divergence of the fundamental beam. For most crystals unless they are poled, a high intensity of the frequency doubled beams is achieved by putting the crystal in an enhancement cavity, which allows the same light to pass many times through the crystal.

Quasi Phase Matching

Quasi-phase matching is a method of achieving useful interaction lenght far in excess of the coherence length using a periodically poled crystal. These crystals are made by applying an electric field at elevated temperatures which flips the optical axis by π every coherence length. Then the crystal is cooled down and this configuration remains without any need for external fields. This has the effect that the phase difference between fundamental and SH beam is reversed right at the point where destructive interference would start to decrease the frequency-doubled intensity. Quasi phase matching therefore ensures that power will only ever flow from the pump to the second harmonic beam. The output from a periodically poled (PP) crystal of length nL_c, where n is just an integer, is smaller than of a perfectly phase-matched crystal of the same length. However the frequency doubled intensity is much bigger than that of a single crystal with a slight phase mismatch. As the periodically poled crystal can be made a lot longer than a single crystal without losing doubling efficiency, it is possible to use it without the need for a cavity.

5.2.2 Doubling Cavity

Frequency doubled light at 552 nm is made by using a lithium triborate (LBO) crystal in an enhancement cavity. This crystal has a high damage threshold of more than 10^5 Wcm^{-2} and less than 0.1%/cm absorption in the infrared. LBO has a melting point above 800°C and a low susceptibility to water. With a conversion efficiency of about 2.6×10^{-4} [118], it can be estimated that a single pass of 1 W infrared power will give a fraction of 1mW of green light. To enhance the green intensity, the crystal sits between two focussing mirrors in a bow-tie cavity and is Brewster cut so that the cavity only accepts light polarised in the vertical plane .The Hansch and Couillaud locking scheme [119] is used to keep the cavity in resonance with the fibre laser. In this scheme, a slight horizontal polarisation component is introduced to the light via a $\lambda/2$ waveplate before the light enters the cavity to act as a phase reference. When the cavity drifts off resonance, the reflected light becomes elliptically polarised, the degree of which is analysed with a $\lambda/4$ waveplate and two photodiodes. The difference between two photodiodes gives the error signal for the lock and is fed back to a piezo inside the cavity. The maximum conversion efficiency for the frequency doubled light that was experimentally achieved was 20%, which meant that a maximum of 180 mW was available. This system was set up by Dhiren Kara and specific information on technical details of the doubling cavity as well as alignment procedures can be found in his thesis [118].

Although the doubling cavity produces more than enough green light, it is prone to drop outs while scanning the fibre laser frequency. It also sometimes exhibits intensity noise of up to 20% in the audio frequency range.

5.2.3 Periodically poled crystal set-up

In order to improve the stability of the green light intensity, the fibre laser output was doubled in a single-pass through a periodically poled lithium niobate crystal. The crystal has a cross-section of 3 mm×0.5 mm, a length of 25 mm and a poling period of 7.73 μm. The infrared light is focussed to a waist of 24 μm in order to optimise the green output. Considering that the crystal has a refractive index of 2.2, the corresponding beam waist in air is 11 μm. The IR beam 15cm after the optical isolator, had a spot size of 650 μm and was slightly converging. In order to achieve the required small beam diameter at the centre of the crystal, the beam is directed through a telescope arrangment and focused into the crystal as shown in figure 5.3. The first lens was put at the position, where the spot size was 650 μm. A $\frac{\lambda}{2}$ waveplate is used to align the polarisation of the pump beam perpendicular

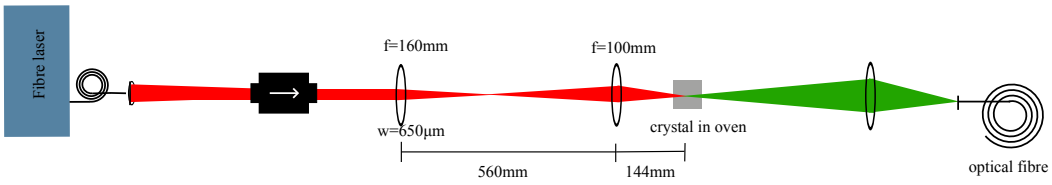


Figure 5.3: Schematic set-up of periodically poled doubling crystal

to the optical axis of the crystal and thereby maximise its conversion efficiency. After setting up the optics, the crystal temperature was varied slowly to optimise the output of the green light. The optimal temperature for our wavelength of 1104nm was found to be 82.1 °C. After establishing the crystal temperature, the frequency doubled output was further increased by changing the position of the lens just before the crystal in order to optimise the beam waist inside the crystal. The optimised lens positions as seen in figure 5.3 then gave a spot size in air of about 14 μm. A frequency doubled beam of 8mW was obtained, using a power of 790 mW in the IR pump beam.

5.3 Absorption Detection and Fluorescence Detection Set-up

A schematic of the detection set-up is shown in fig. 5.4. The probe laser used to address the $X^2\Sigma^+ \rightarrow A^2\Pi_{1/2}$ transitions in YbF at 552 nm is a frequency doubled Koheras Boostik fibre laser. The frequency doubling is done by a doubling cavity or in a single pass through a periodically poled crystal (sec.5.2.2 and sec. 5.2.3). A small amount of the power is split off and coupled into a HighFinesse model WS6 wavemeter with a relative accuracy of $\approx$ 100 MHz and an absolute accuracy of 600 MHz as well as a low finesse confocal Fabry-Perot cavity with a free spectral range of 375 MHz. The cavity is used for scan calibration with a high relative frequency resolution. The main beam is transmitted to the breadboard that sits around the cryostat vie a single mode optical fibre.

On the breadboard, the laser beam is split into four separate beams. One is used to

probe the amount of absorption inside the cell and is directed onto a Thorlabs DET 100A photodiode after leaving the cryostat. The photodiode is used with a homemade amplifier which results in a detection bandwidth of tens of kHz. Two of the beams are reduced to a size of 1.25 mm (diameter) by using a telescope arrangement and enter the cryostat via a periscope at distances of 23 mm and 132 mm from the cell aperture (z=0) (see figure 5.5). They are used to probe the molecular beam by laser-induced fluorescence and have typical intensities of 40 mW/cm^2.

Inside the cryostat, the imaging set-up at these two heights consists of a spherical mirror with a radius of curvature of 25 mm and an aspheric lens with a back focal length of 10.5 mm. The mirror is set up two focal lengths from the centre of the molecular beam, while the lens is set up one focal length from it on the opposite side. After going through the first aspheric lens, the roughly collimated fluorescence exits the vacuum chamber and goes through another aspheric lens to be focused onto a photomultiplier tube (pmt). The two pmts used are a Hamamatsu R760 and Hamamatsu R2228 with a quantum efficiency at 553 nm of 7% and 8% respectively. The fourth beam is used for optical pumping of the YbF molecules and enters the cryostat through a window 82 mm above the aperture. A breadboard on top of the cryostat allows us to direct a beam through the top window of the cryostat and focus it onto the exit of the cell. This beam is counterpropagating to the molecular beam and therefore makes it possible to measure the Doppler shift due to the forward velocity of the molecular beam. The fluorescence of this beam is detected using the pmt installed 23 mm above the cell aperture.
Due to high signal levels, the two pmts are operated in current mode, each of them having a current-voltage converter with 7 different gain settings. To be able to convert from a given current to a photon rate, they both had to be calibrated. This was done by putting them into a blacked-out box with a light-emitting diode (LED) and measuring the amplifier output voltage and the photon count rate for each amplifier gain setting and for various LED currents.

5.3.1 Fluorescence detection efficiency

As the absolute flux of molecules in the beam is an important quantity to measure, the detection efficiency η_{D} has to be calibrated. It is determined using the formula:

$$\eta_{\mathrm{D}} = \frac{\Omega_{\mathrm{lens}}}{4\pi}(1 + R_{\mathrm{m}})T_{\mathrm{lens}}^2 T_{\mathrm{w}}^2 q, \tag{5.7}$$

where $\Omega_{\mathrm{lens}} = 2\pi\left(1 - \frac{1}{\sqrt{1+\left(\frac{r_{\mathrm{lens}}}{f}\right)^2}}\right)$ is the solid angle subtended by the lens with $r_{\mathrm{lens}} =$ 10.7 mm and $f = 10.5$ mm being the radius and focal length of the collection lens. $R_{\mathrm{m}} =$ 0.87 is the efficiency of the mirror, $T_{\mathrm{lens}} \approx T_{\mathrm{w}} \approx 1$ are the transmission of the lens and the window and $q = 0.07(0.08)$ is the quantum efficiency of the lower(upper) detector. This gives an expected detection efficiency of about 2 % for both detectors. To check this

estimate, the detection efficieny was measured using a 0.5 mm×0.5 mm wide emission angle LED and putting it at the focus of the first aspherical lens inside the cryostat. The power was then measured just after the second aspherical lens, where normally the pmt would sit, using a Thorlabs PM100 powermeter. This net fluorescence detection efficiency from this measurement is only 0.5 %. It is not clear why the efficiency determined empirically is less than expected from equation 5.7 but we consider it to be more reliable because it is empirical and this is the efficiency that was used in the next chapter to determine the molecular beam intensities.

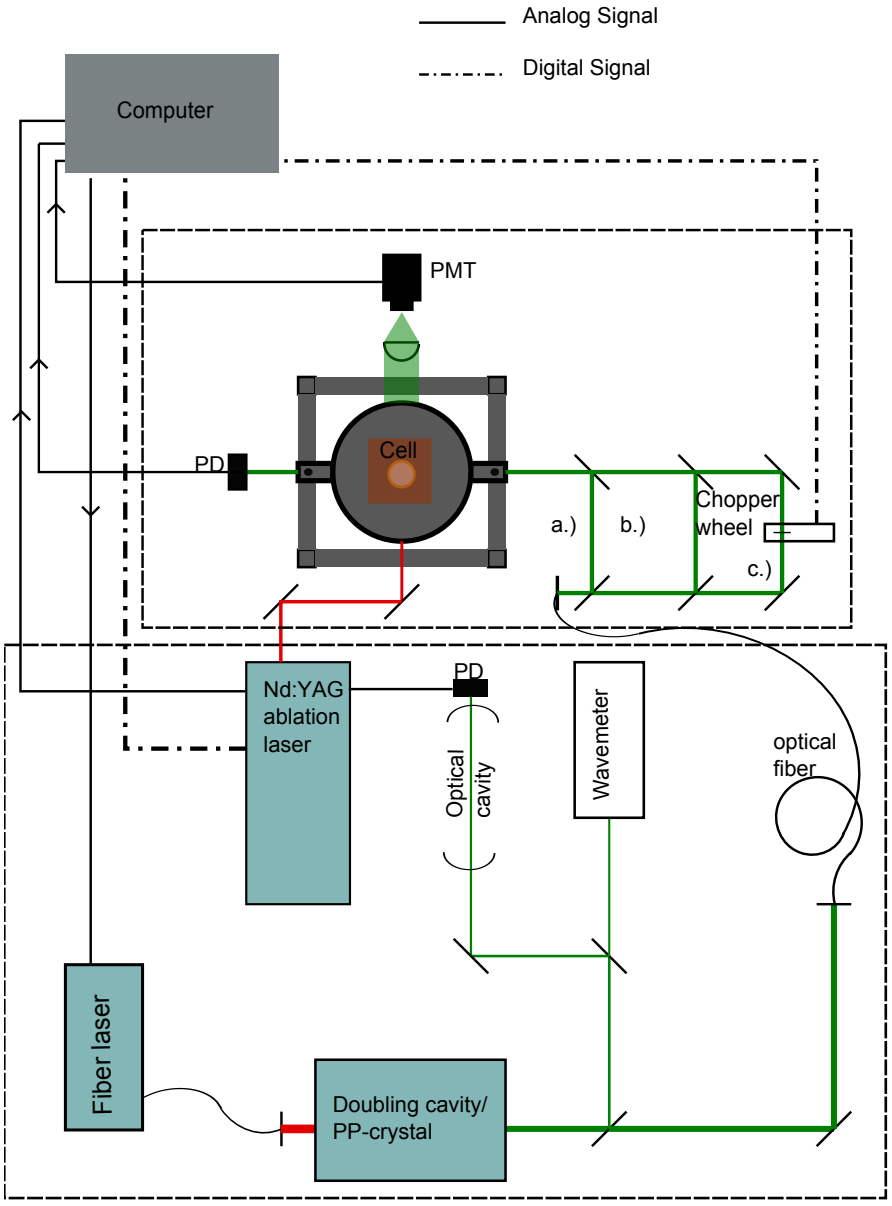


Figure 5.4: Schematic of second experimental set-up

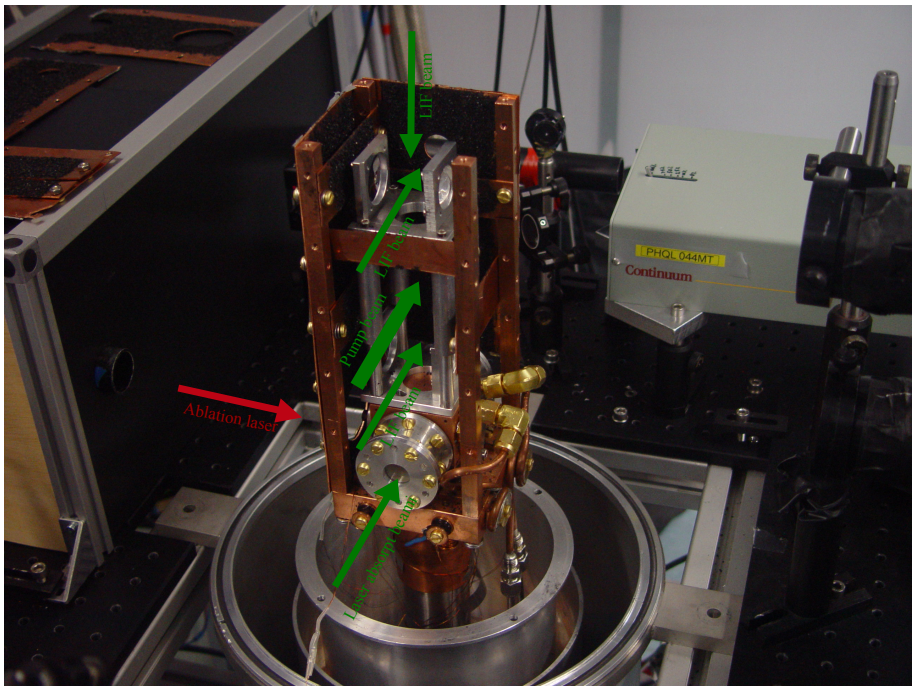


Figure 5.5: Picture showing buffer gas cell with positions of laser absorption and laser induced fluorescence beams indicated

Chapter 6

A cold and slow beam of YbF molecules

6.1 Flow and extraction efficiency of a buffer gas cell

In the experiments described in this chapter, molecules are loaded into a buffer gas cell and then either leave the cell through an aperture, or diffuse to the cell walls, where they stick. Depending on the buffer gas pressure used, the flow regime can be tuned from effusive to supersonic. A detailed description of these flow regimes is given in appendix B. In case of an effusive source, the molecules diffuse to the cell walls and to the exit aperture (area A) on a characteristic time scale given by the diffusion time τ_{D}. This gives an approximate extraction efficiency of

$$\eta_{\mathrm{e}} = \frac{A}{S_{\mathrm{c}}} \tag{6.1}$$

where S_{c} is the inner surface area of the cell. This results in a low extraction efficiency. The cell used in most experiments is shown in figure 5.2 and can be approximated with a cube of a side length of 0.03 m. Various exit apertures were used but for most experiments it was a slit of 0.75 mm width and 4 mm length. The extraction efficiency obtained from eqn. 6.1 is 0.06%. To enhance this efficiency, the pressure in the buffer gas cell is increased so that the molecules are entrained in the flow of helium. Another characteristic time constant, namely the average time a helium atom spends in the cell, can be defined as τ_{p}. This time is given by

$$\tau_{\mathrm{p}} = \frac{nL^3}{F}, \tag{6.2}$$

where F is the flow rate. Introducing a parameter

$$\gamma = \frac{\tau_{\mathrm{D}}}{\tau_{\mathrm{p}}} \tag{6.3}$$

helps to distinguish between different flow regimes. For the effusive flow just described $\gamma \ll 1$ as the time taken for the molecules to diffuse to the walls is far less than the average time a helium atom spends in the cell. It is assumed that there are no collisions inside or

after the aperture and hence the average forward velocity is given by eqn. B.8. Because the YbF molecules are cold and heavy this effusive speed is low. As γ increases, the diffusion time (for a cube given by eqn. 4.12) becomes longer and the two time constants become comparable. At higher density it is possible to extract more molecules entraining them in the helium flow so that they leave the cell, before they have the chance to diffuse to the walls and are lost. Since $\tau_{\mathrm{D}} \propto nL^2$, as discussed in chapter 4, we have $\gamma \propto \frac{F}{L}$.
It is likely that the region of high flow is confined to a certain part of the cell, depending on the cell geometry and the relative positions of inlet tube and exit aperture. The volume occupied by the region of high flow will be referred to as the hydrodynamic volume. If molecules are born in the hydrodynamic volume, they are entrained in the flow and rapidly carried out of the cell. Molecules that are created outside this hydrodynamic volume have to diffuse through the cell to reach it in order to be carried out. As the molecules are entrained in this helium flow, their forward velocity will increase to that of the helium atoms, making it a faster as well as brighter beam. However for moderate pressures, the forward velocity is still less than the supersonic velocity of helium at cryogenic temperatures (see different regimes in section B.2), because there are only a few collisions in and outside of the aperture. Increasing γ further will increase the hydrodynamic volume inside the cell and therefore the extraction efficiency.
Due to the complex flow properties in the cell, it is difficult to assign a length scale to this hydrodynamic volume. However as $\gamma \propto \frac{F}{L}$, this suggest that the extraction efficiency for a fixed throughput F can be improved by reducing the size of the cell. The gradient in density between the hydrodynamic volume inside the cell and the rest of the cell also makes it difficult to assign a Knudsen number, which is the ratio between the mean free path λ and a characteristic dimension L of the flow field (eqn. B.1), to the gas in the cell. The average density in the cell for various set helium flows depends on the flow rate out of the cell. It can be estimated by using eqn. B.10 for effusive flow and by eqn. B.40 for maximum hydrodynamic flow. It is expected that the actual number density lies somewhere between the two. In figure 6.1, the number density assuming effusive and supersonic flow in a cell with a 4 mm$\times$0.75 mm slit aperture, is plotted as a function of the helium flow into the cell. The data points in this figure were obtained by measuring the flow on a flow-meter and the pressure using a Pirani gauge positioned at the room temperature end of a long return tube attached to the cell. Thermal transpiration effects were taken into account using eqn. 2.3. The experimental data lies within the expected regions. A Knudsen number can be assigned to this average helium density by using equation B.1. For the helium flows used in our experiments and the slit aperture, the Knudsen number is shown in figure 6.2(a) (where a helium diffusion cross-section of $(2.863 \times 10^{-10})^2\pi$ m^2 has been used [96]). For helium densities high enough that supersonic velocities are reached outside the cell, the Mach number in the vicinity of the aperture is 1 and therefore the Reynolds number is:

$$R_{\mathrm{e}} = \frac{3}{2}\sqrt{\pi 2\gamma}\frac{1}{K_{\mathrm{n}}}. \tag{6.4}$$

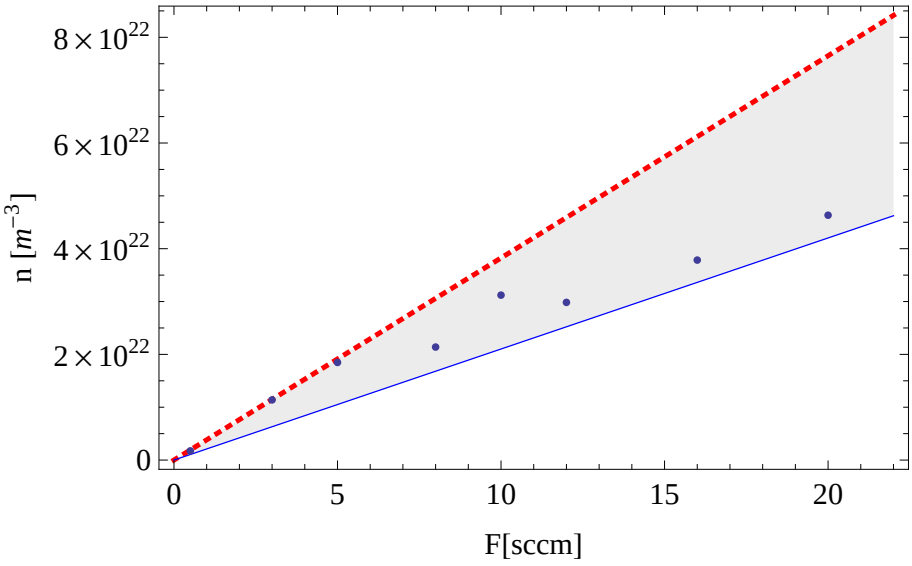
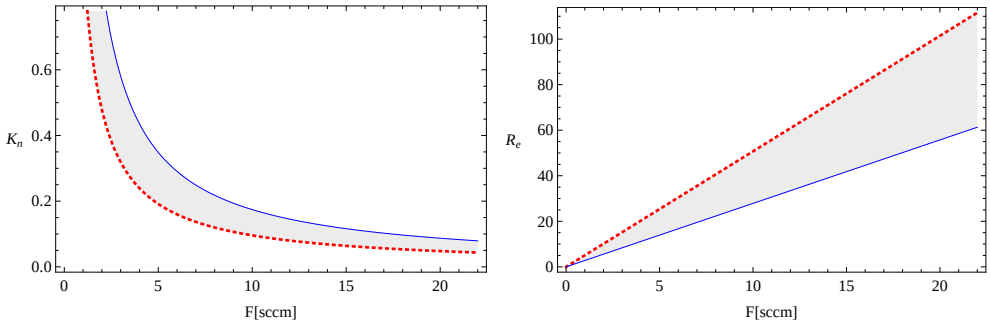


Figure 6.1: Estimated average number density in the cell by assuming an effusive (red, dotted) and maximum hydrodynamic (blue) flow rate out of a slit aperture. Measured datapoints (blue) using a pirani gauge at room temperature to measure the cell pressure agree well with estimated number densities.

The Reynolds numbers for the typical helium flows used are plotted in 6.2 b). At the



(a) Knudsen number as a function of helium flow

(b) Reynolds number at the throat as a function of helium flow

Figure 6.2: Knudsen and Reynolds numbers (at the throat) for typical helium flows used in the experiment and the slit aperture, assuming an effusive (red,dotted) and maxmimum hydrodynamic (blue) flowrate

throat the number of collisions is approximately $1/K_{\mathrm{n}}$, which looking at figure 6.2 amounts to about 20 collisions inside the aperture for the highest flow of 22 sccm used in the experiments of this chapter. As these calculations were made using the average number density in the cell, the number of collisions obtained from it, should be seen as a lower limit. Using the number of collisions estimated from the Knudsen number can also be used to estimate the increase in forward velocity due to a small number of collisions . Every collision in the aperture imparts a momentum of $m_{\mathrm{He}}\bar{v}_{\mathrm{eff}}$ to the molecule. Assuming that this momentum is entirely directed in the forward direction, multiplying $\frac{m_{\mathrm{He}}\bar{v}_{\mathrm{eff}}}{M_{\mathrm{mol}}}$ with

the number of collisions N roughly gives the increase in forward velocity compared to an entirely effusive beam

$$v_{\mathrm{f}} = \bar{v}_{\mathrm{eff}} + \frac{m_{\mathrm{He}}\bar{v}_{\mathrm{eff}}}{M_{\mathrm{mol}}}N \tag{6.5}$$

This equation is only valid for low N, for higher N, the hydrodynamic limit of the velocity for respective stagnation parameters is reached.

6.2 Measuring beam parameters of a YbF buffer gas beam

The geometry of the buffer gas cell used with a continuous flow of helium is described in section 5.1.1. The molecules leave the cell through an aperture situated in the centre of one of the faces of the cubic cell. The experiments in this chapter used three different apertures made out of copper and sealed to the cell body using indium wire. They were a hole of diameter 0.75 mm and depth 1 mm, an array of channels (5×5 channels with d=0.75 mm and a length of 3 mm) and a slit 0.75 mm wide, 4 mm long and 1 mm thick. Whenever convenient these apertures are abbreviated with h, a and s respectively. As this cell is operated with a continuous helium flow, a good cryopump is required to maintain an adequate guard vacuum. As described in chapter 5, the cryopump becomes saturated after a certain time and then regenerates itself. To minimise the helium gas load and therefore maximise the running time between saturation events, the first experiments were performed using the hole aperture. A flow controller gives reliable control over the helium flow into the cell. After having better control over the helium density, the single hole aperture was exchanged by a slit and an array of channels in order to look for improvements in the beam flux and at the differences in temporal and spatial molecular beam shape.
The experiments using different apertures were all done with the helium inlet pipe coming in right above the target, about 2 cm from the cell aperture. As an attempt to try to match this helium flow region better to the inital distribution of molecules in the cell after the ablation pulse, a second helium inlet pipe was mounted at the bottom of the cell, opposite the cell aperture. Being on opposite sides of the cell it was hoped that this would increase the number of molecules being swept out of the cell. The positions of the helium inlet pipe are indicated by 1 for the top and 2 for the bottom for each aperature(as seen in figure 5.2), e.g. s2 means the slit aperture with the helium inlet at the bottom of the cell was used.

6.2.1 Optimisation and measurements of beam flux

The main objective of using a buffer gas source is to obtain a high flux of cold molecules moving at low speed. There are several parameters that can be altered, to maximise the flux, including the buffer gas density in the cell as explained in appendix B, the ablation power and the geometry of the aperture.
The flux is measured by recording the laser induced fluorescence (LIF) signal on two seperate detectors (23 mm and 132 mm from the cell aperture). The two probe lasers are

parallel to one another and intersect the molecular beam at right angles. Both signals are recorded as a function of time with a resolution of a few μs. In order to compare the different apertures and helium inlet configurations, the time-resolved signal is integrated over the whole pulse to give the total number of molecules per ablation shot. Then to obtain the total number of molecules in a particular rotational level, the detection laser frequency is scanned and the signal is integrated over the particular rotational line (including all hyperfine components). Many applications where cold molecular beams are used, such as the YbF EDM experiment [5] or loading the molecules into a trap or Stark decelerator, favour a beam that is narrow in time. For that reason, the peak flux is also given in units of molecules per sr per μs. To obtain the correct number of molecules per steradian, the detection efficiency of the pmt has to be taken into account,as described in section 5.3.1, as well as the solid angle being probed. This solid angle can be estimated from the detection volume consisting of a parabolic mirror and an aspheric lens, which limits it to 1 mm^3 and the distance from the aperture. The solid angle that is subtended by the molecules at the lower and upper pmt is then 1.5×10^{-3} sr and 4.5×10^{-5} sr respectively.
A general procedure was used to maximise the molecular beam flux after starting the experiment. First some signal had to be found. There was usually some signal on the lower pmt as care was taken to align probe and ablation beams while the cryostat was open. Once seen, the signal was optimised by moving the YAG laser on a spot of the target that gave the best signal. Then the helium flow was varied over the whole range of the flowmeter (between 1-22sccm) to obtain the best signal[1]. Then the ablation intensity was varied by altering either the Nd:YAG power or ablation laser spot size.
To be able to maximise the extraction efficiency of the cell, we wanted to investigate the flow region inside the cell. Therefore absorption images of the cell were taken as a function of time after the ablatio pulse for a few different helium flows, just as for the closed cell described in section 4.5.

Results

Figure 6.3 shows a typical LIF signal as recorded on a pmt 23mm from the cell aperture. The ablation laser is fired at t=0, however we usually start recording 500 μs before that in order to record the background for normalisation purposes. The molecular signal usually arrives a few 100 μs after the ablation pulse and has a width of hundreds of μs to a few milliseconds, depending on the helium flow and position of the helium inlet tube. A reason why the absorption profiles are broadened in time is that molecules are either created in the flow region of the cell and swept out rapidly or they are created somewhere else in the cell and have to diffuse to the flow region to be extracted. Ideally we want to suppress the second mechanism. Table 6.2.1 summarizes the measurements of the flux for various configurations of exit aperture and inlet tube location. The table gives the flux of YbF molecules in the ground electronic, vibrational and rotational state, reporting both the peak

[1] best in this case means highest photon rate over shortest amount of time

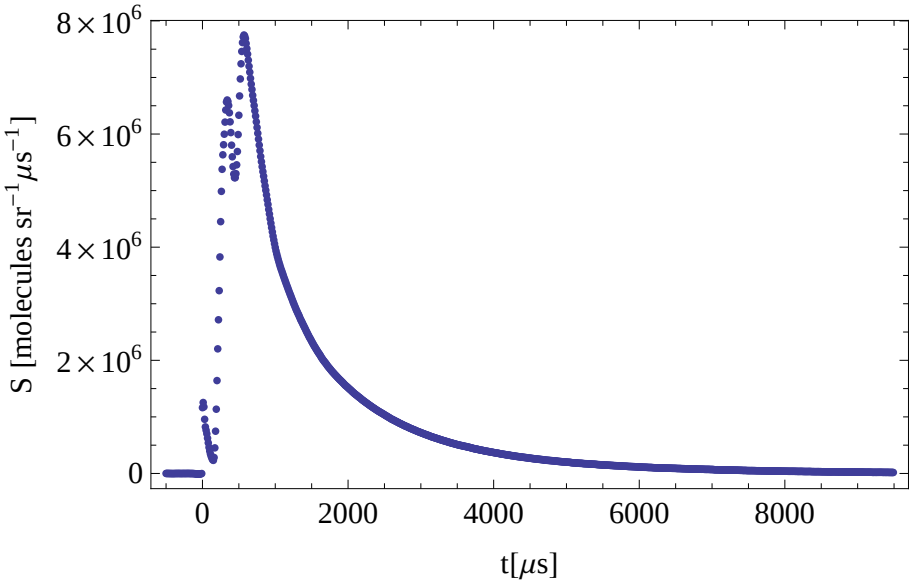


Figure 6.3: Typical LIF signal on pmt 23mm from the cell aperture

flux (molecules sr^{-1} μs^{-1}) and the flux integrated over the whole pulse (molecules sr^{-1} $pulse^{-1}$). The main error on the flux comes from the uncertainty in the calibration of the detection efficiency, which is estimated to be 25% (see section 5.3.1). Not all measurements were taken on the same spectral line, so to get the absolute number of molecules in the rotational ground state, the various linestrengths (sec. A) were taken into account and a rotational temperature of 4K was used. In terms of absolute flux the results show that when any thin aperture was used, the shape of the orifice was not critical, only the array of channels gives a slightly lower flux. However we have noticed that after opening the cryostat to install new apertures or targets, it was not unusual for the molecular fluxes to vary by a factor of two (even for the same aperture), therefore the lower flux for the channel aperture is not seen as significant. For the slit aperture the helium gas line was moved to come in from the bottom of the cell to improve the overlap between the helium flow region in the cell and the region where the molecules are born. Figure 6.4 shows the temporal behaviour of the molecular pulse for the various apertures after adjusting the helium flow for maximum flux. This shows that the peak flux is enhanced when the inlet is at position 2 even though the total number of molecules extracted does not change significantly. This is because a higher fraction of the molecules are created inside the hydrodynamic volume and are swept out rapidly, forming a relatively intense short pulse at early times. In figure 6.5, the total flux of molecules is shown as a function of the helium inlet flow for the s1 configuration. While the flux increases linearly for low flows, it saturates around 10 sccm.

To look at the overall extraction efficiency, absorption images were taken for the cell configuration s2 at a probe laser frequency corresponding to the $X^2\Sigma^+ - A^2\Pi_{1/2}$ (0-0) band-head. The results for a flow of 4 sccm and 20 sccm can be seen in figure 6.6. At the bottom of each image is the inlet for the helium gas, which has a diameter of 2 mm. The slit aperture is located on the top of each image. At the lower helium flow, some flow from the

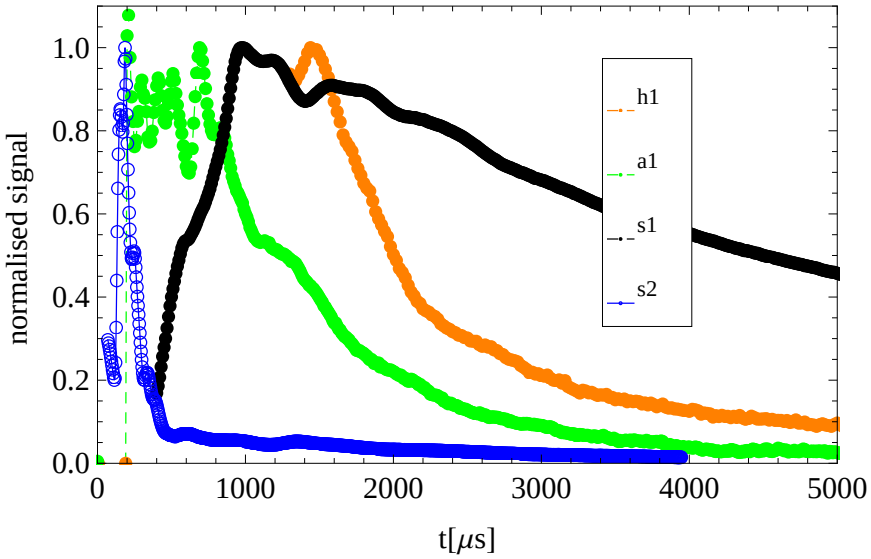


Figure 6.4: Comparison of molecular signals as a function of time after the ablation pulse for different cell configurations

Table 6.1: Maximum flux of molecules for different cell apertures in the lowest rotational state (N=0)

Aperture	Total flux (Moleculessr^{-1}pulse^{-1})	Peak flux(Moleculessr^{-1} μs^{-1})
h1	2.27×10^{10}	2.54×10^{7}
a1	4.15×10^{9}	4.35×10^{6}
s1	7.88×10^{9}	2.17×10^{6}
s2	1.05×10^{10}	3.6×10^{7}

inlet to the outlet can be seen as well as turbulance in the form of eddies which transport the molecules around the cell and back into a lower region of the helium flow. At the higher flow rate, the flow region in the middle of the cell is broadened, however due to the turbulance it is not obvious how the extraction efficiency scales with flow and how to define an effective hydrodynamic volume. The saturation seen in figure 6.5 can possibly be attributed to these occurence of eddies in the cell as shown in the absorption images.
In order to estimate the extraction efficiency, the average absorption in the cell is obtained by integrating over the image taken at a helium flow of 4 sccm 127 μs after the ablation pulse. This gives an average absorption of 30% inside the cell. Using equation 3.27 and assuming that the probe laser intensity was well below the saturation intensity gives a total number of at least 8.7×10^{10} molecules in the rotational ground state inside the cell. As these images were recorded at the bandhead, it is difficult to tell which rotational line between 1-7, the laser addressed. However by assuming the least and most populated line, a lower and upper limit for the extraction efficiency is obtained. A typical flux of molecules per sr per pulse in the rotational ground state observed with this aperture and a flow of 5 sccm is (see table) 1.05×10^{10}. Assuming our buffer gas beam has a similar divergence of 0.21 sr as observed for other buffer gas beams [81] we obtain a total number of 3.1×10^{9}

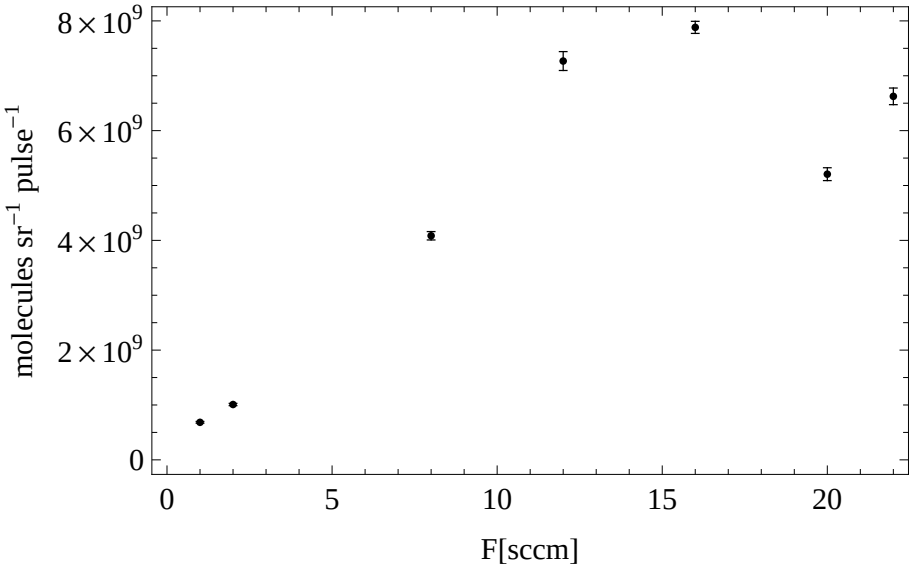


Figure 6.5: Molecular beam flux as a function of helium flow, using the buffer gas cell with the s1 aperture.(The Reynolds number for the s1 cell configuration lies in the range of $(2.8 - 5.1)\times$F[sccm], depending on the flow regime.)

molecules in $N = 0$ extracted from the cell. This gives an extraction efficiency between 0.5% and 3%. Independent, simultaneous laser absorption and LIF measurements on the Q(1) line give an extraction efficiency of 1%.

6.2.2 Centre of mass velocity and translational temperature

An important property of a molecular beam is its centre of mass velocity. Lower forward velocities make it easier to load molecules into a trap and allow longer coherence times for high precision measurements. To measure this, a laser beam was sent counterpropagating to the molecular beam and focused through the cell aperture to avoid excessive background scatter from the cell surface. By recording consecutive LIF spectra using this beam as well as a laser beam perpendicular to the molecular beam, the forward velocity can be inferred from the Doppler shift of a particular spectral line. An example of this is shown in figure 6.7. This data was taken with the cell in configuraion s1 and with a flow of 4 sccm. From the measured Doppler shift we obtain a speed of 157 ms^{-1} in this case. An alternative method is to measure the two LIF time profiles from two laser beams intersecting the molecular beam perpendicularly and determining the velocity from the time of flight. However the temporal profile of the pulses is often complicated and for this reason this method is inferior to using the Doppler shift.

The longitudinal spread of velocities was determined by measuring the Doppler broadening of the LIF signal induced by the probe beam counterpropagating to the molecular beam. The natural linewidth of the YbF $X^2\Sigma^+ \rightarrow A^2\Pi_{1/2}$ transition is 5.7 ± 0.2 MHz [93], which can be neglected compared to the Doppler broadening which gives a FWHM of 56 MHz at

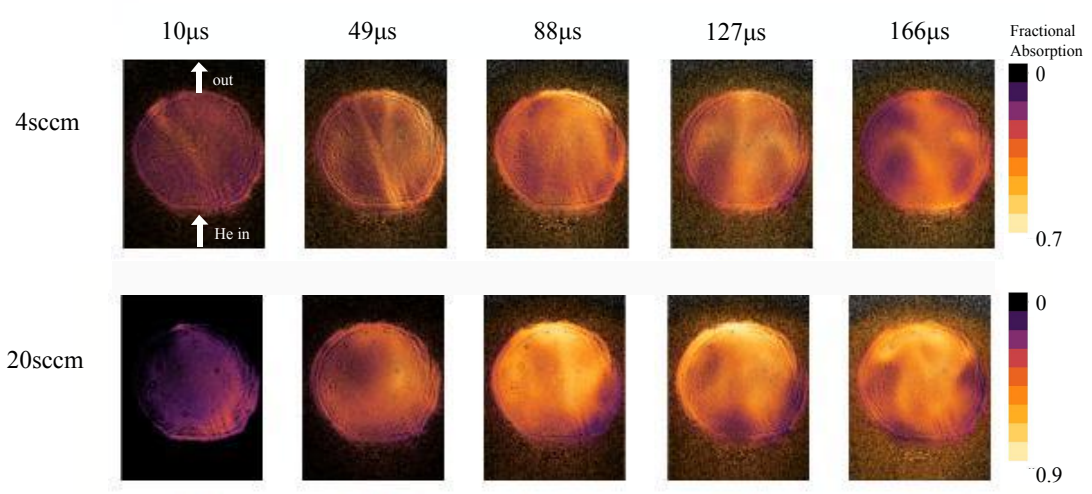


Figure 6.6: Absorption images of the cell with a helium inlet at the bottom and a slit aperture on the top for two different helium flows. The size of the images corresponds to the one inch diameter window, through which the molecules are detected.

4 K. However it is very easy to saturate the transition of the molecules in the beam (sec. 6.2.4), which produces power broadening. To account for this possibility the data were fitted to Voigt profiles with both Lorentzian and Gaussian widths as free parameters in the fit. In case the Voigt fit did not give a result, the spectrum was fitted to a Gaussian and the result for the temperature was seen as an upper limit.

Results

The velocity measurements presented here were performed for the configuration s1. In figure 6.8, the mean forward velocity of the molecular beam is plotted as a function of the helium flow rate. It can be seen that for low flows, the forward velocity of the molecules is close to the forward velocity of an effusive helium beam at 4K. At very low flow rates, we might expect the speed to approach that of an effusive YbF beam at 4K, which is about 23 ms^{-1}. In reality, for all flows where the signal was detectable, the forward velocity was higher than 100 ms $^{-1}$. The YbF molecules created by ablation have to be stopped inside the cell, and must thermalise to low temperatures, and it is possible that the helium density needed to achieve this is too high for the YbF beam to be purely effusive. As the helium flow is increased, the forward velocity of the molecules increases as well until it reaches the hydrodynamic limit. A simple model describing the increase in forward velocity with flow as described by eqn. 6.5 is included in figure 6.8. The velocity is increased as a function of flow as $v_\mathrm{b} = 3.39$ F[sccm]. The estimated functional uncertainty in measuring the forward velocity is 10%. The spectra from the two probe beams were not obtained simultaneously, but rather one after the other. To calibrate the laser scans we measured the transmission of a low finesse cavity with a free spectral range of 375 MHz. Using this

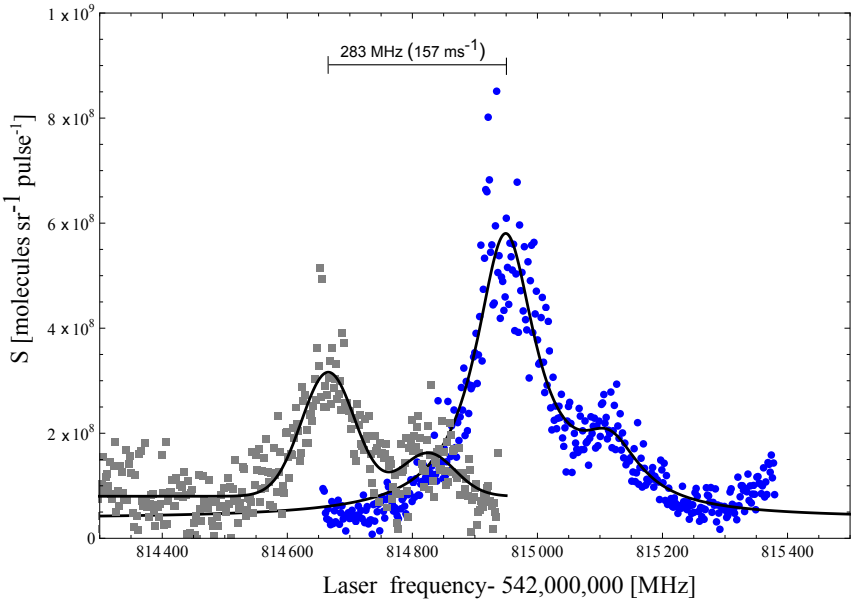


Figure 6.7: LID Spectra of the Q(2) transition in YbF obtained by using a probe laser perpendicular (full circles, fitted to two Lorentzians) and counterpropagating (open circles, fitted to Gaussians) to the molecular beam

data the scans were linearised and aligned, and the error in this procedure results in the 10% error in the velocity measurements. A better procedure would be to switch rapidly between the two probes so that the spectra are obtained nearly simultaneously. The measurements of the translational temperature were performed for the slit configuration with the helium line coming in from the side. For a flow of 16 sccm, the spectrum could be fitted to a Voigt profile (fig. 6.9) and gives results for the gaussian FWHM of 66.2 ± 8.5 MHz and lorentzian component FWHM of 36.9 ± 4.8 MHZ. This gaussian width corresponds to a translational temperature of 5.6 ± 1.4 K. The lorentzian linewidth seems rather large compared to the estimated linewidth of 5.7 MHz, however it is very easy to saturate the transition in a beam and typical saturation intensities are around 0.8 mW/cm (see section 6.2.4). The probe beam used to obtain this data had a power of about 1 mW and was smaller than 1 mm at the detection region, which gives an expected power broadening between 30-40 MHz. For the data obtained for other flows, a Voigt fit was not possible and therefore a gaussian was fitted, keeping in mind that the resulting temperature is then an upper limit. Fitting the spectrum at 16 sccm to a gaussian instead of a Voigt profile yields a translational temperature of 16.7 ± 0.4 K, showing that the temperature obtained this way is indeed overestimated. For other flows of 12 sccm, 20 sccm and 22 sccm, the results from a simple gaussian fit yield $T_{\shortparallel} < 11.4 \pm 0.8$ K, 16.1 ± 0.8 K and 24.6 ± 1.2 K respectively.

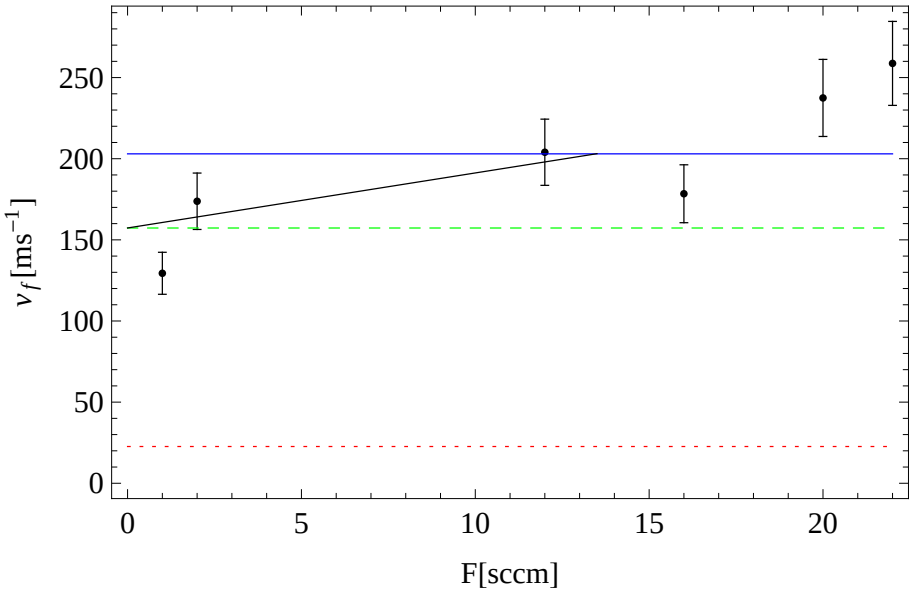


Figure 6.8: Forward velocity (ms^{-1}) of the molecular beam measured using the Doppler shift method, versus the helium flow (sccm). The red dotted line represents the most probable velocity of an effusive YbF beam at 4 K, the green dashed line that of an effusive helium beam at 4 K and the full blue line indicates the maximum attainable velocity with a supersonic expansion. The black line is the model given by eqn. 6.5.(The Reynolds number for the s1 cell configuration lies in the range of $(2.8-5.1)\times$F[sccm], depending on the flow regime.)

6.2.3 Rotational Temperature Measurements

The rotational temperature was determined by looking at the relative populations in different rotational levels. These were derived from the relative strengths of the rotational lines observed in fluorescence with a laser beam perpendicular to the molecular beam. The sampled velocity spread is limited by the optics and therefore the main component of the linewidth probed in this way is lorentzian, most probably arising due to power broadening. To compare the relative populations of different lines, the lines were fitted to lorentzians and the peaks of the two resolved hyperfine components were added together.

Results

In figure 6.10, a LIF spectrum is shown with the source in configuration s1 of YbF at 4K close to the $X^2\Sigma^+ \rightarrow A^2\Pi_{1/2}$ (0-0) bandhead. The different rotational components are labelled and it can be seen that the intensity for lines with rotational number higher than 2 decreases. This already suggests that the molecules have a low rotational temperature. A Boltzmann distribution fitted to the peaks of the resolved hyperfine peaks as shown in figure 6.11, yields a rotational temperature of 3.3 ± 0.4K at the point of maximum signal

Same results were obtained for configurations a1 and s2 as given in table 6.2.

Knowing the rotational temperature of the molecular beam and recalling that the translational degrees of freedom thermalise more rapidly than the rotations, it is expected

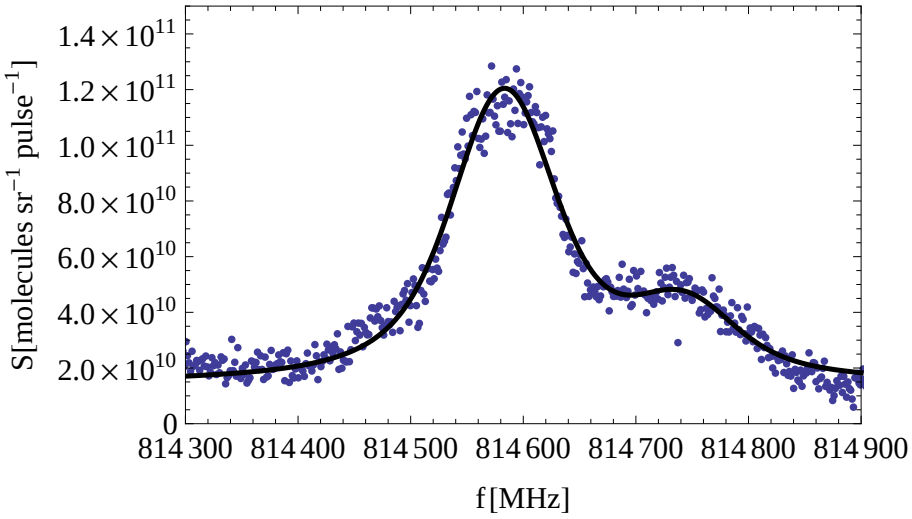


Figure 6.9: LIF Spectrum of the Q(2) transition, taken with a laser beam counterpropagating to the molecular beam. The black line shows a fit to a Voigt profile, which yields a longitudinal temperature of 5.6 K

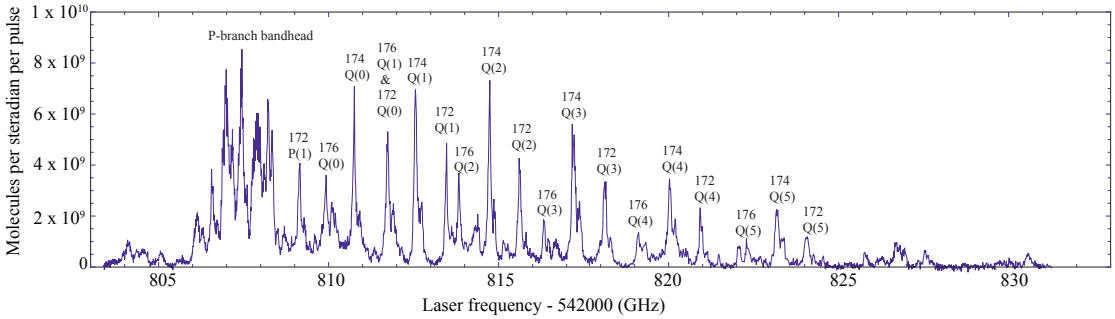


Figure 6.10: LIF spectrum of YbF at 4K close to the $X^2\Sigma^+ \rightarrow A^2\Pi_{1/2}$ (0-0) bandhead, obtained using the cell in configuration s1. The probe laser is perpendicular to eh molecular beam. The labelling identifies the rotational lines and isotopes.

that the translational degrees of freedom have a similar temperature and are well below the upper limit given in section 6.2.2. The rotational temperature was determined as a function of time after the ablation pulse for the s1 and s2 configuration by integrating the LIF spectra within time bins of 100 μs duration. The results are shown in figure 6.12. The data show that for the early part of the molecular pulse, the rotational temperature is slightly higher than for the rest of the pulse. The amplitude of this first slightly hotter part depends strongly on the position of the ablation laser on the target. This suggests that some molecules can leave the cell without too many collisions with the helium gas, perhaps because the ballistic expansion away from the ablation target takes them very close to the aperture where they are then swept out.

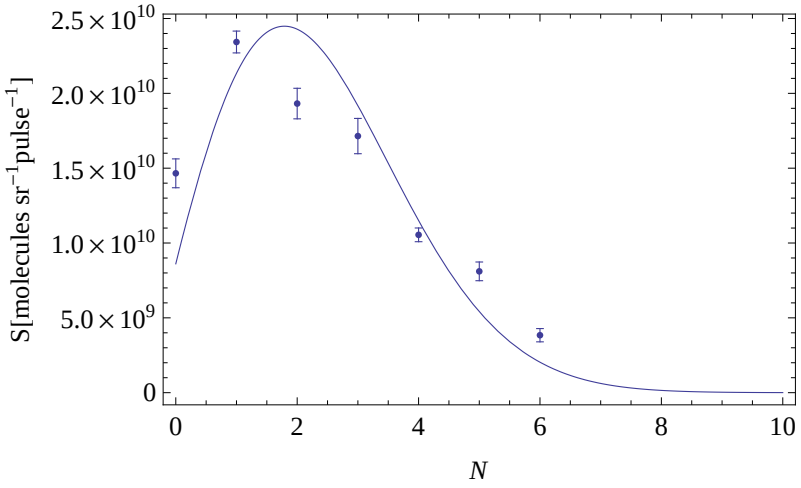


Figure 6.11: Populations in different rotational levels obtained from the LIF spectrum in shown in figure 6.10, fitted to a Boltzmann distribution

Table 6.2: Results for rotational temperature of the molecular beam for different cell apertures and positions of the helium inlet tube

Set-up	T_{rot}[K]
a1	3.1 ± 0.4
s1	3.3 ± 0.4K
s2	3.2 ± 0.2K

6.2.4 Optical pumping measurements

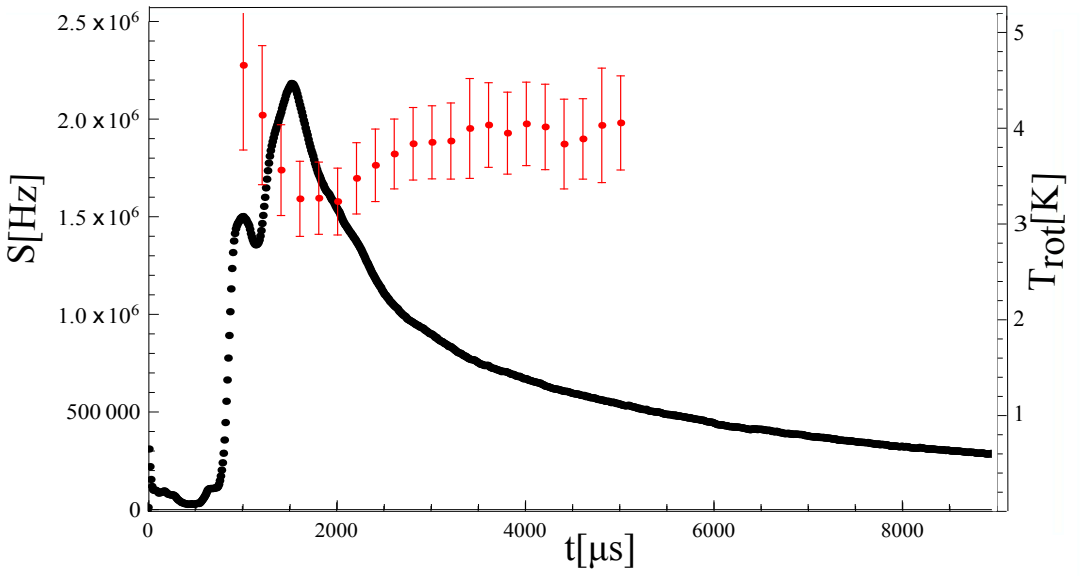
At the exit of the cell, collisions between the molecules and the helium atoms are frequent. As the molecules move away from the cell, the helium density, and hence the collision rate, drops off until at some point there are no further collisions and the molecules form a free molecular beam. It is interesting to measure where this transition to a free beam occurs since for most molecular beam experiments the collisions are undesirable.

To measure how dominant collisions are in the region around the upper detector, which is 132 mm away from the cell aperture, a pump beam was used 50 mm below the upper detector to optically pump a significant fraction of the molecules out of the ground state. The relative signal measured at the upper detector with and without the pump beam is a measure of the degree of optical pumping.

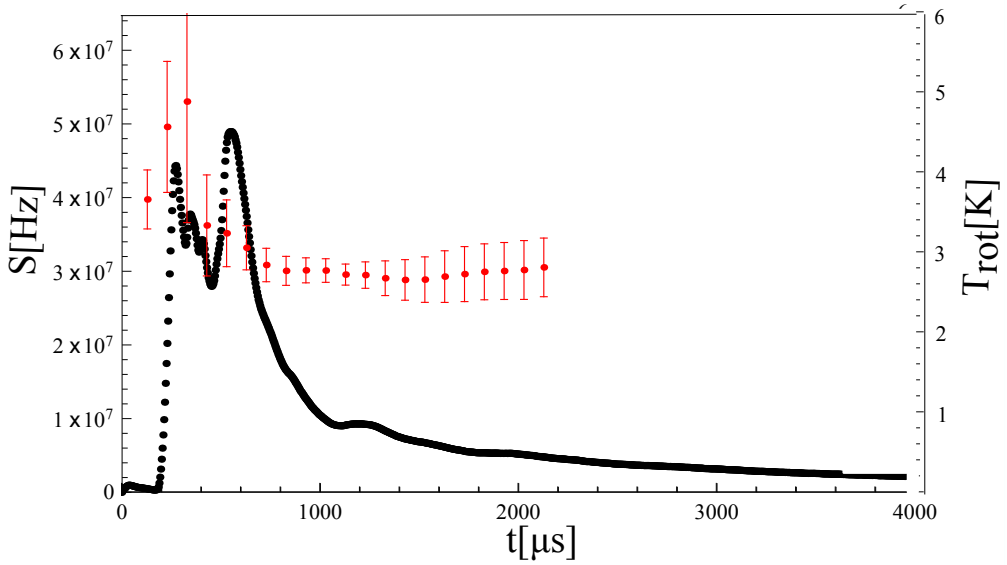
The intensity in the pump beam needed to saturated the transition is very small as it is determined by the transit time t_{T}. If we describe the molecules again by the 3-level model that was introduced in chapter 3 and we assume a low flux ϕ ($\phi \ll (1-r)\Gamma$), then the saturation intensity, for a low pressure and hence a collision rate that is far smaller than ϕ, is given by:

$$I_{\mathrm{sT}} = \frac{\pi h c}{3\lambda^3 r p} \frac{2}{t_{\mathrm{T}}(1-r)} \tag{6.6}$$

For a typical transit time of $t_{\mathrm{T}} = 5\ \mu$s, this gives a saturation intensity of 0.8 mW/cm^2.



(a)



(b)

Figure 6.12: LIF signal (black points) of YbF versus time measured at the lower detector and rotational temperature versus time (red points) for (a)configuration s1 and (b)configuration s2

The pump power used for these measurements was 5.5 mW, therefore we were easily able to saturate. Furthermore as the transit time increases with the beam diameter and hence the required intensity to saturate decreases, expanding the pump beam is a way of being sure to saturate. This is also convenient as it makes it easier to optimise the vertical overlap of the pump and probe beam and hence make sure that they are interacting with the same molecules. To factor out the variation in ablation yield, a shutter wheel was put into the

path of the pump beam and synchronised to the ablation laser, running at a frequency of 5 Hz. This made it possible to have two consecutive shots with and without the presence of the pump beam. After each scan, the average signal with and without the pump beam was taken. This was done for several different helium flows.

Results

The results of these measurements are shown in figure 6.13. The figure shows the ratio of the signal with and without the pump beam as a function of the helium flow. To understand this data, let us once again use a simple three level model to represent the molecule, with the laser connecting levels 1 and 2, and the 3rd level representing all other relevant levels in the molecule. The laser pumps the molecules into level 3. Inelastic collisions can then transfer those molecules back into the ground state. Assuming that the collision energy is insufficient to transfer population from level 1 to level 3, the population in level 3 is depleted by collisions as $\frac{dN_3}{dz} = -n_{\mathrm{He}}\sigma_{31}N_3$ and hence the fraction in level 3 is $f_3(z) = f_3(0)e^{-\sigma_{31}\int_0^z dz' n_{\mathrm{He}}}$, where $f_3(0)$ is the fraction in state 3 immediately following optical pumping. As $f_1 + f_3 = 1$, the fraction f_1 of molecules in state 1 is:

$$f_1(z) = 1 - f_3(0)e^{-\sigma_{31}\int_0^z dz' n_{\mathrm{He}}}, \tag{6.7}$$

The experiment measures $f_1(z_0 = 50\mathrm{mm})$ as a function of flow rate. The helium densities are expected to be proportional to the flow so we can write $\sigma_{31}\int_0^z n_{\mathrm{He}}dz' = kF$, we get $f_1(z_0) = 1 - f_3(0)e^{-kF}$. A fit of the experimental data to this model is shown by the solid line in figure 6.13. The parameters obtained from this fit are $f_3(0) = 0.8 \pm 0.04$ and $k = 0.09 \pm 0.03$. Let us assume that over the short region between pump ($z = 0$) and probe ($z = z_0$) the helium density $n_{\mathrm{He}}(z)$ can be replaced by its average value over this region $\bar{n}_{\mathrm{He}}$. Then, $\bar{n}_{\mathrm{He}} = \frac{k}{\sigma_{31}z_0}F$. We do not know the value of σ_{31}, however in section 3.5, we measured the sum of σ_{31} and σ_{c}, the latter being the cross-section for velocity-changing collisions, and we obtained the result $\sigma_{31} + \sigma_{\mathrm{c}} = (37 \pm 14) \times 10^{-20}\mathrm{m}^2$. We can use this value as an upper limit for σ_{31}. Then we obtain the relationship between the average helium density between 82 mm-132 mm from the source, and the flow rate through the cell as $\bar{n}_{\mathrm{He}}(82\ \mathrm{mm}) = 4.75 \times 10^{18}$ F[sccm] where the constant of proportionality should be taken as an upper limit. A theoretical value for the helium density at a given distance from the aperture and for a given flow can be found by calculating the number density in the cell as described in section 6.1 and then using eqn. B.44 and eqn. B.26 to obtain the density at the centreline as a function of distance from the aperture. In this way we obtain $\bar{n}_{\mathrm{He}}(82\,\mathrm{mm}) = 3.54 \times 10^{18}\,F[\mathrm{sccm}]$, reasonably close to the relationship found above. The two results are shown in figure 6.14. This experiment can be seen as a check that the cross-section is on the same order of magnitude as the velocity changing cross-section. An average helium number density of $4.8{\times}10^{19}$ m^{-3} at a typical flow of 10 sccm at a distance of 82 mm from the cell aperture, gives a mean free path of about 4 cm.

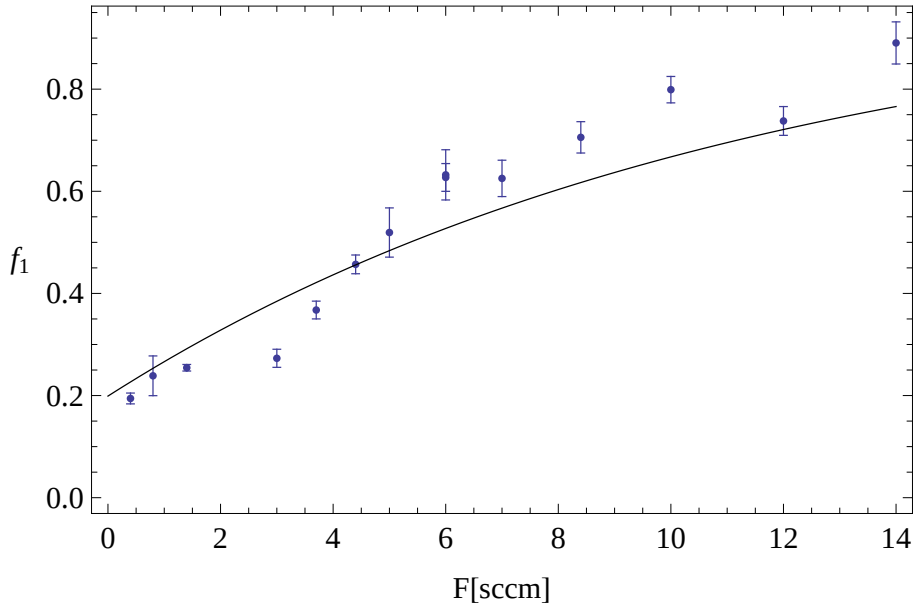


Figure 6.13: Fraction of molecules in state 1, after pump beam has been used, as a function of helium flow. The black line is a fit to the data using equation 6.7

6.2.5 Beam flux with and without a skimmer

To reduce the helium density in the detection region and pick off the coldest, densest part of the beam, a skimmer was introduced. It was mounted on the holder for the optics for the second pmt, leaving its opening about 82 mm above the cell aperture. It is a trumpet shaped 1 mm skimmer that has a length of 30mm and was cut down a bit to have a slightly bigger opening of 2 mm. This isn't ideal as the edges are supposed to be as sharp as possible. The flows were varied to see how the transmitted intensity changed. The flux was measured on the Q(2) line of the ^{174}YbF isotope, both on the lower pmt, which is close to the aperture and on the upper pmt, which is after the skimmer. The ratio between the two fluxes for different helium flow settings was taken to investigate the effect of the skimmer. For comparison, a control experiment was performed without a skimmer, while everything else was kept the same.

Results

The ratio of the total molecular flux measured at the two detectors is shown in 6.15 as a function of the helium flow. Two separate datasets are shown, one with the skimmer and one without. This shows that even for relatively low flows, the molecular flux at the upper detector is reduced if a skimmer is introduced in the beam path. Increasing the helium flow decreases this signal further. This is in agreement with the explanantion of skimmer interference given in section B.2.1. A skimmer is best installed in a region where there are rarely any collisions. As seen from the optical pumping measurements, for a flow of 10 sccm , the mean free path in the region were the skimmer was installed is around 4 cm. The diameter of the skimmer was 2mm, which gives a Knudsen nummer of 20. From section

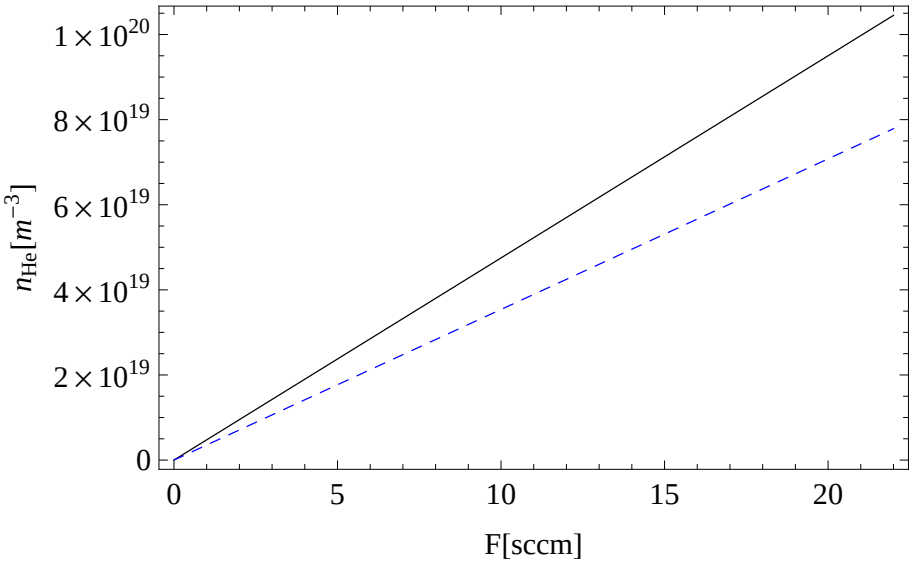
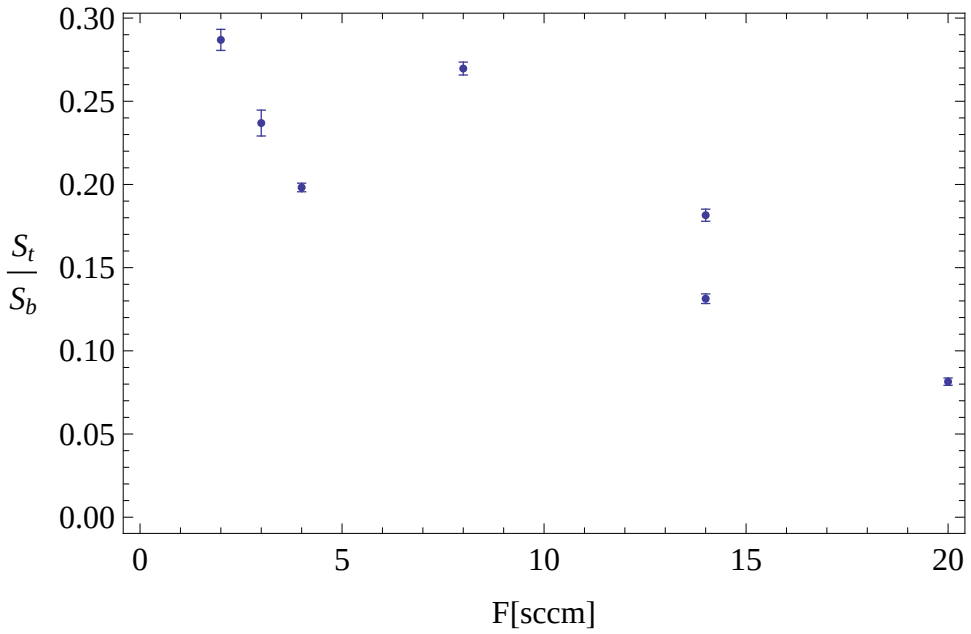


Figure 6.14: Average helium number density 82 mm from the cell aperture as a function of helium flow into the cell, estimated from optical pumping measurments (full line). This result is compared to the theoretical centerline number density at the same position estimated from the helium flow (dashed line)

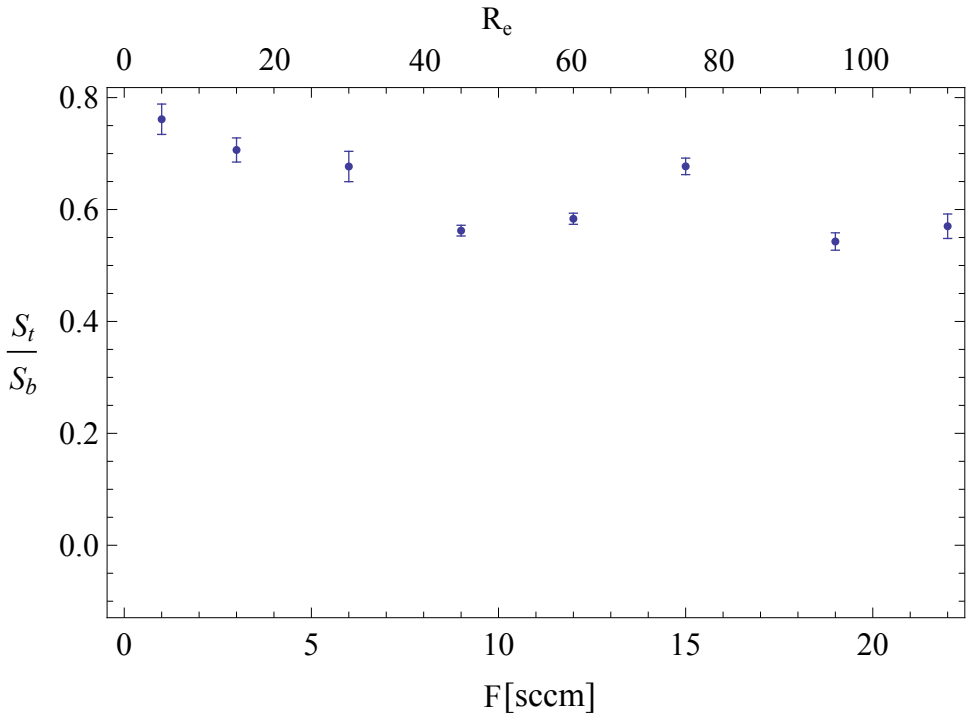
B.2.1, it is known that no skimmer interference is expected for $K_{\mathrm{ns}} > 50$. Hence at the distance the skimmer was introduced, it is expected that a significant number of helium atoms are backscattered from the skimmer surface and the collisions between those and molecules in the beam result in a loss of molecules passing through the skimmer. These effects get worse with higher flow as seen in figure6.15(a).

6.3 Characterising a YbF buffer gas beam with a pulsed helium source

When the helum flow is continuous, the major limit for the running time of the experiment and the maximum helium flow rate, is the saturation of the charcoal sorption pumps. In order to reduce this helium load, a new set-up incorporating a pulsed solenoid valve (General Valve Series 99) was tested. These valves are usually operated at 24 V and have minimum opening times of tens of ms. For our molecular beam experiments significantly faster opening times are desirable. To ensure as quick an opening and closing time of the valve as possible, a short high voltage pulse is applied to the solenoid. The gas from the pulsed valve is delivered to the cell reservoir through another copper tube with an inner diameter of 1 mm. This tube is angled upwards and pointed slightly at the target. The valve sits on the bottom of a copper cold plate that is attached to the cold stage of the cryocooler. The gas line leading into the valve is anchored to this cold stage as well to ensure that the gas is cold when it enters the valve chamber. The idea of this type of set-up is to have a pulse of gas at the moment of ablation, so that the molecules can thermalise with the cold helium gas, and for the helium to then be pumped away as quickly as possible.



(a) Ratio of molecular flux measured before and after a 2 mm skimmer.



(b) Ratio of molecular flux measured at lower and upper detector without a skimmer.

Figure 6.15: Ratio of molecular flux measured at lower and upper detector (a) without and (b) with a skimmer situated between the two detectors.(The Reynolds number for the s1 cell configuration lies in the range of $(2.8 - 5.1)\times$F[sccm], depending on the flow regime.)

The cell in this set-up consists of a copper cylinder wih a radius of 15 mm and 50 mm long, with several 5 mm wide slots running along the cylinder length and with the target

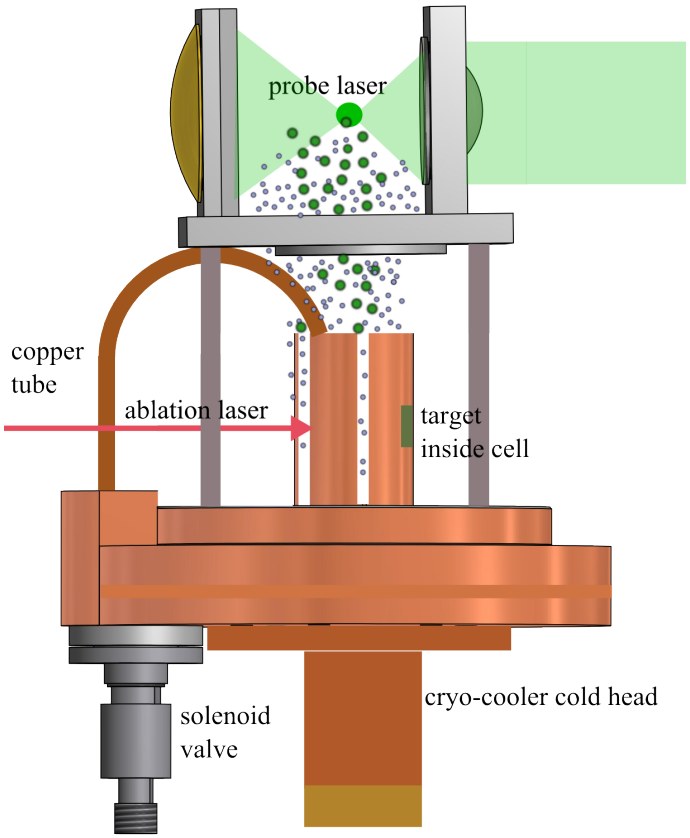


Figure 6.16: Schematic figure of buffer gas cell with pulsed helium flow

placed inside. The slots are used for the probe and ablation laser. The set-up is shown schematically in figure 6.16. Another advantage of this open design is that no windows are needed. The windows were a problem in the continuous helium flow cell, because they became covered with ablation products and after many days of running became so opaque that the ablation laser was ablating the coating from the window rather than the target.

6.3.1 Calibrating the amount of helium emitted by the pulsed valve

To estimate the density of helium delivered to the cell in this set-up, we attached the same solenoid valve to a closed evacuated chamber and measured the pressure rise due to a fixed number of 200 μs long pulses, and for several different voltages. From this pressure rise and the volume of the cell the total number of helium atoms emitted in a single pulse is found. The result is shown in figure 6.17. Using this result, we estimate the peak helium density in the open cell to be on the order of 10^{22} m^{-3}, similar to the number density in the continuous flow set-up.

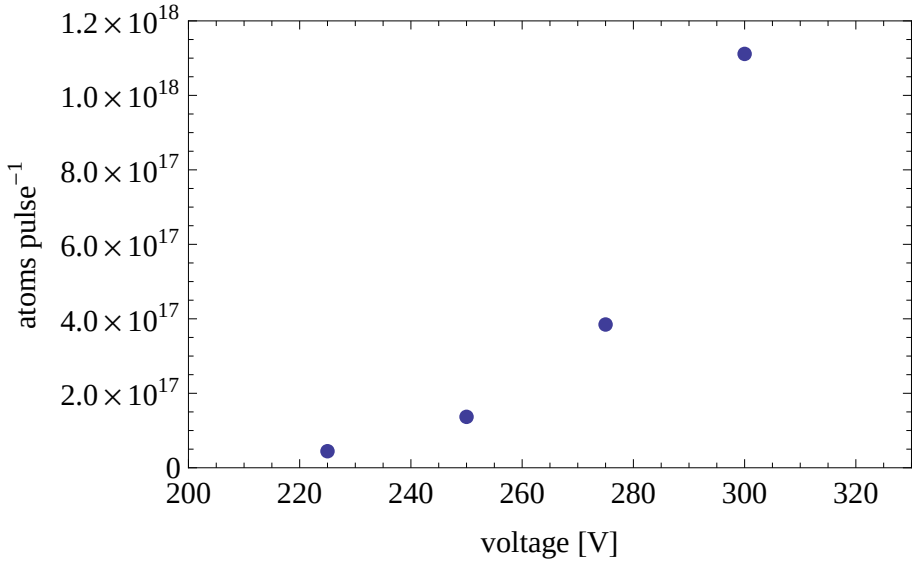


Figure 6.17: Number of helium atoms versus voltage applied to solenoid valve for a 200 μs pulse

6.3.2 Optimising the beam flux

A typical LIF signal using the pulsed set-up can be seen in figure 6.18. The helium was pulsed in for a length of 200 μs and the valve was opened 812 μs before the ablation laser was fired. The decaying signal at early times is due to light from the ablation target whereas the peak arriving after about 180 μs is laser induced fluorescence from the molecules. It

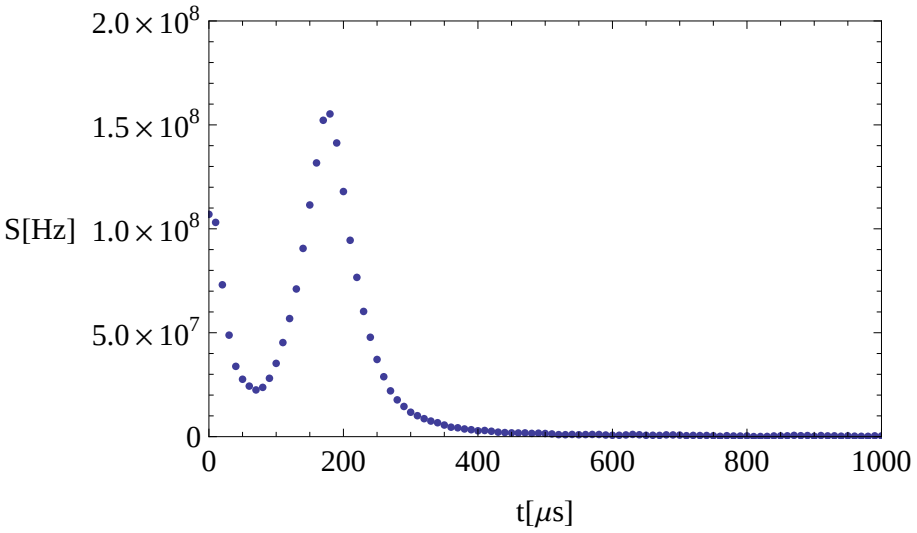


Figure 6.18: LIF signal over time using the buffer gas cell with pulsed helium, using a pulse length of 200 μs and opening the valve 812 μs before firing the ablation laser

is important that the molecular pulse overlaps with the gas pulse. As the valve opening time and pulse length is controlled from ScanMaster, which provides the trigger for the Q-switch of the ablation laser as well, the time between the valve firing and the Q-switch

can be scanned. The minimum pulse length needed for the valve to open is 200 μs. As increasing the valve pulse length did not increase the overall molecular yield and a short pulse is desirable, 200 μs was chosen as the setting for subsequent experiments. Figure 6.19 shows how the molecular pulses change as the time between the opening of the valve and the Q-switch is changed. If the valve is fired too early, there is already some helium density

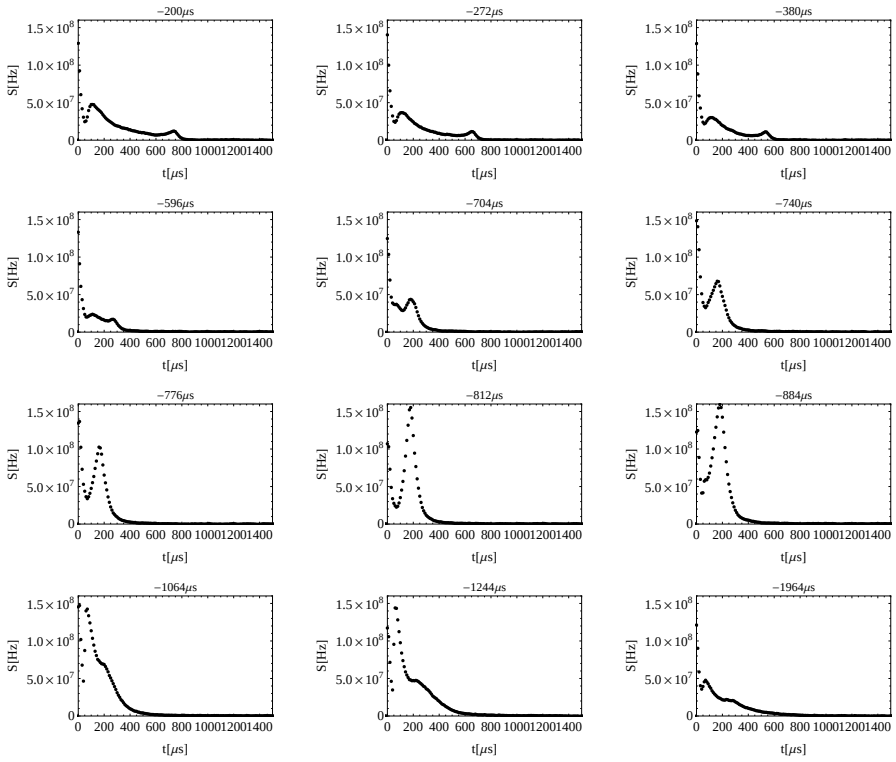


Figure 6.19: Molecular fluorescence signal over time for different valve opening times measured on the lower detector.

in the cylinder as the molecules are ablated into it. Some molecules are initially blasted out of the cylinder with only a few collisions and arrive very quickly at the first pmt. Although the gas pulse has ended when the ablation laser fires, some molecules thermalise with the helium density that is left in the cylinder and diffuse out. When the valve is fired later the helium density in the cylinder at the time of ablation is higher. For relatively low helium density, the forward velocity corresponds to roughly the effusive velocity of a helium beam. As the pressure gradient between the cylinder and the surrounding increases, the forward velocity of the created molecules is increased due to hydrodynamic effects. As the gas and ablation pulses start to overlap, the molecules are accelerated further. When the valve is triggered about 812 μs before the ablation laser is fired, the peak of the gas pulse reaches the target just as the ablation occurs. Then some molecules are picked up by the gas and undergo a supersonic expansion reaching their maximum attainable speed. This timing is mostly dependent on the copper tube which carries the helium from the valve to the cell region and can change a little if changes to the set-up that require slight alterations to this tube have to be made. If the gas pulse is fired too late, the molecules are ablated before the

valve has fired. As there is a pressure gradient between the cylinder and the surrounding due to ablation alone and some helium is expected to have accumulated on the target, which then gets ablated off, a molecular signal can still be seen. Then as the gas from the valve reaches the target, it pushes all the molecules that are still left in the cylinder out in a time span corresponding to the valve pulse length. The normalised molecular flux is plotted as a function of the valve opening time in figure 6.20 (dashed line). As discussed above, by changing the timing of the valve, the forward velocity changes as well. Therefore figure 6.20 also shows the forward velocity as a function of the valve timing. The figure shows that for the opening times of the valve that give a significant signal, the forward velocity varies between 270 ms^{-1} and 360 ms^{-1}. For the peak signal, the measured forward velocity in this dataset is about 273 ± 14 ms^{-1}. This velocity is higher

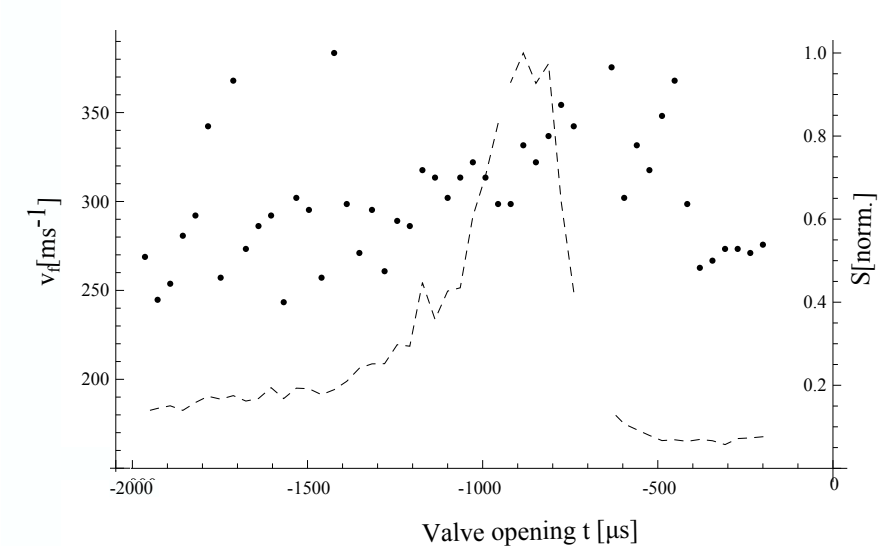


Figure 6.20: Normalised molecular flux (dashed line) as well as forward velocity (datapoints) as a function of valve opening time with respect to the Q-switch (t=0)

than the hydrodynamic limit. This suggests that the buffer gas gets heated up either by the solenoid valve or by the ablation process. From eqn. B.23, it can be estimated that the temperature of the buffer gas is changed for different valve opening times between 7 K and 12.5 K. From equation B.2 we know that to calculate the Reynolds number inside the cell, the density of the helium gas and the flow velocity have to be known. By scanning the time between the opening of the valve and the Q-switch, the density of the helium at the moment of ablation is changed, which influences the forward velocity. The forward velocity was measured in our experiment, however the exact helium number density was not monitored over time, which makes it difficult to assign a Reynolds number. Assuming the gas pulse and molecular pulse are perfectly overlapped, for a gas pulse length of 200 μs and a pressure of 2 bar behind the valve, an upper limit on the Reynolds number of 200 can be estimated.

One thing that was also noticed using this type of set-up was that sometimes a fluorescence

signal could be seen even without the probe laser. It is possible that this fluorescence is due to Yb that is excited to a metastable state during the ablation process and that the fluorescence from the decay of the excited state is observed at the detectors. It was found that this fluorescence seemed to be very dependent on ablation power and fortunately it was possible to set the power to a value where a decent YbF signal is observed but no background fluorescence signal is seen. However it was always very important to check whether the fluorescence disappeared with the probe laser. After optimising the ablation spot, choosing a valve pulse length of 200 μs and firing the valve 1120 μs before the Q-switch, a spectrum of the R(2) transition was taken. From this data a yield of $(9.3 \pm 0.65) \times 10^{10}$ molecules per steradian per pulse in the N=2 state is calculated.
The centre of mass velocity for this particular dataset was measured from the time of flight between the two detectors to be about 313 m/s. This means that the helium gas is most likely heated to about 9.4 K. Considering line strengths and an upper limit of the rotational temperature of 9.4 K, the flux of molecules in the rotational ground state can be calculated to be $(2.4 \pm 0.19) \times 10^{10}$ molecules per sr per pulse and the peak flux is $(1.4 \pm 0.1) \times 10^{8}$ molecules sr^{-1} $\mu\mathrm{s}^{-1}$. This method of producing a cold molecular beam produces pulses that are shorter in time than the buffer gas cell with continuous flow. Therefore with further improvements it could be advantageous for many experiments.

6.4 Conclusion

In this chapter experiments performed using different cell apertures and two different set-ups were discussed. The flux, forward velocity, rotational and translational temperature were measured. The maximum total flux of molecules in the lowest rotational and vibrational state was similar in all the experiments.

However a shorter molecular pulse is advantageous for most applications such as trapping or further deceleration of the molecules. The time profiles of the molecular pulses for different apertures and helium inlet configurations are shown in figure 6.4. The pulses were optimised by varying flow and ablation parameters. This clearly shows that in the cell set-up, a shorter pulse can be achieved if the helium inlet is opposite the cell aperture. This configuration is able to entrain more molecules right after they have been created and thus avoids a broader pulse due to molecules having to diffuse to the flow region in the cell in order to be extracted. The FWHM of the molecular pulse obtained is about 120 μs. A similar short molecular pulse of about 130 μs can be achieved using the pulsed helium set-up. The length of the helium gas pulse can be reduced to 200 μs and if the gas pulse and the ablation pulse are reasonably well overlapped, a narrow molecular pulse is obtained. The result can be seen in figure 6.21, where the molecular signals have been normalised to their individual peak fluxes. An advantage of the open set-up is that the length of the molecular pulse is tuneable in situ. It also foregoes the need for a window for the ablation laser which gets coated by ablated material from the target making it less and less transparent with an increasing number of ablation shots.

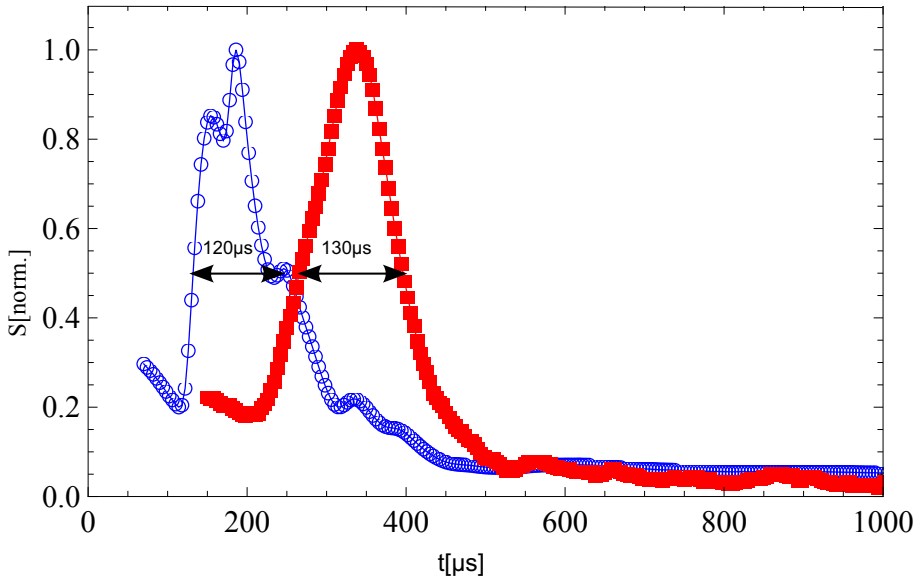


Figure 6.21: Shortest molecular pulses are achieved with the buffer gas cell if the helium line comes in at the bottom (blue, circles) or the open pulsed set-up (red, square)

The rotational temperature was measured for the buffer gas cell set-up. All different apertures showed that the rotational temperature is in equilibrium with the He temperature after the molecules have left the cell. Measurements of the longitudinal translational temperature using a counterpropagating laser beam further confirmed the expected cold translational temperature. The counterpropagating beam made it possible to get a measurement of the forward velocity of the beam as well. These measurements were done for various helium flows and showed an increase of forward velocity with flow and a maximum velocity that was a little higher than the maximum supersonic speed of He at 4 K. For the pulsed helium set-up, the forward velocity was estimated from the time of flight between the two pmt positions. This showed speeds higher than the supersonic speed of helium at 4 K. This suggests that the buffer gas is heated up inside the valve and due to ablation to about 9 K.

Chapter 7

Conclusion and Outlook

This chapter summarises the results presented in this thesis and discusses improvements and variations that can be made to the current set-up. At the end an outlook on future work will be given.

7.1 Measurements inside a closed buffer gas cell

Saturated absorption and absorption spectroscopy was used to detect YbF molecules inside a closed buffer gas cell, which was cooled by a liquid helium cryostat. High resolution spectra were obtained via saturated absorption spectroscopy, and the identification of various rotational lines in the spectrum was aided by changing the temperature of the cell between 293 K and 10 K. The same methods can be applied to any molecule that can be loaded into a buffer gas cell. In our cell this can be done by laser ablation, which requires a solid precursor or if the vapour pressure is high enough at room temperature, the molecules can be transferred into the cell via a gasline that has a poor thermal link to the buffer gas cell [120].

The in-cell dynamics were investigated to obtain better knowledge of the collision and cooling processes of the molecules in the buffer gas cell. The loss time of the molecules in the cell was investigated by looking at laser absorption over time for different helium densities. At low density, this showed a linear increase with density as expected for diffusion, but a levelling off of the time constant at higher densities. This behaviour has been observed by several groups working on buffer gas cooling of atoms and molecules [121, 110]and was explained by possible capture of the molecules or atoms by clusters and impurities produced and ablated during the ablation process. Simulations of the diffusion process in our cell were done using a finite element program and it was found that the levelling off of the time constant can also be explained through diffusion processes alone. As the buffer gas density is increased, the intial distribution of the created molecules changes from being nearly homogeneously spread across the whole cell to being confined to a smaller volume close to the target. As diffusion is driven by a density gradient, the initial decay in peak signal is faster in the latter case. Using the measured loss time constants for lower

helium densities, where a linear increase is observed, a value for the diffusion cross-section of YbF in He was obtained. This is a widely used method for measuring diffusion cross-sections among groups using buffer gas cooling ([111, 8, 112, 113, 110]). In this thesis the possible errors of this technique have been thorougly discussed. To forego the need of a good knowledge of the diffusion dynamics in the cell and the exact helium density inside the cell, it is best to use a reference atom for which the diffusion cross-section is well known. The diffusion cross-section for YbF in He was measured to be $(41 \pm 4) \times 10^{-20}$ m^2 at 293 K. This cross-section can be used to estimate the thermalisation rate of the hot YbF with the cold helium. For a typical buffer gas density of 5×10^{22} m^{-3}, it takes about 10μs to cool the YbF molecules from 2000 K to 293 K. The collision processes were further investigated by looking at the saturation of absorption on the YbF transition used to probe the molecules, as a function of buffer gas density in the cell. A value for the sum of velocity changing collisions and inelastic collisions at 80 K was found to be $(37 \pm 14) \times 10^{-20}$ m^2. The temperature of the molecules was measured and by looking at the translational and rotational temperature over time, it was surmized that the ablation process heats up the buffer gas. The cooling back down to cell temperatures can be characterised by two time constants of about 100 μs and a few 100 μs.

7.2 Producing a cold beam of YbF molecules

A beam of YbF molecules was extracted through an aperture in the cell and the resulting flux, speed and temperature were measured for several configurations of the cell aperture. The position of the helium inlet tube with respect to the aperture of the cell was changed which resulted in altering the time dependence of the molecular signal. Using this set-up, a translationally and rotationally cooled beam with fluxes of 10^{10} molecules sr^{-1} pulse^{-1} was produced. The forward velocity is tunable from about 130-200 ms^{-1} by changing the helium density inside the cell . For the buffer gas densities that give the highest flux, the width in time of the molecular beam can be tuned from a few ms down to about 120 μs by using different apertures and changing the location of the helium inlet line. The shortest signal is achieved by using the helium inlet opposite the cell aperture. Using an optical pumping method the collision rate 82 mm downstream of the aperture was estimated to be 4 collisions per ms. Another set-up was built which consists of a copper cylinder that is open at the top and a pulsed valve which transfers helium gas into this cell via a copper tube. This set-up gave both the highest total flux as well as the highest peak flux. The molecular pulse and the helium gas pulse were overlapped by scanning the timing between the Q-switch of the ablation laser and the opening of the valve. This changes the forward velocity from about 270 ms^{-1} to 360 ms^{-1}. As this is higher than the hydrodynamic limit for the helium at 4 K, this change in velocity is most probably a change in temperature of the beam. This suggests that the buffer gas thermalises to temperatures between 7 K and 12.5 K depending on the delay between valve pulse and ablation pulse. The buffer gas might be heated either by ablation or due to the power dissipation in the solenoid

valve. The latter effect has been reported by Smith et al. [122]. They found that a higher backing pressure of initially cold gas seemed to decrease the heating effect slightly, letting them run their experiment at frequencies up to 10 Hz. However their experiments showed that a solely external cooling of the valve was not enough for running a continuous stable, cryogenic experiment at 10 Hz. Ghazarian et al. [123] found that during operation at a repetition rate of 10 Hz, their valve nozzle was heated up by the firing of the solenoid valve from 4 K to 15 K.
The produced buffer gas cooled source can be compared to a conventional YbF supersonic source [71], which produces a flux of 1.4×10^9 molecules sr^{-1} pulse^{-1} at a translational and rotational temperature of 3.5 K and with a centre of mass velocity of 600 ms^{-1}. With the current set-up, we obtain a flux which is more than an order of magnitude higher and a forward velocity which is at least 3 times lower than the velocity of the room temperature supersonic source.The rotational and translational temperatures are similar.

7.3 Outlook

The cold molecular beam source presented in this thesis is a suitable source for new measurements of the electron's electric dipole moment [5]. In this experiment, the electron EDM is determined by measuring an electric-field induced splitting of two magnetic sublevels, via Ramsey type spin interferometry. In order to increase the sensitivity of this experiment, the product $\sqrt{N}\tau$ has to be increased, where N is the number of molecules that are being probed and τ corresponds to the observation time. The observation time can be increased by using slower molecules. From the above comparison between the buffer gas source and the conventional supersonic source of YbF, it can be seen that this sensitivity can already be increased by an order of magnitude.

7.3.1 Improvements to and variations of the source of cold molecules

Although we are able to make cold beams of YbF molecules, there are some problems with the source, which need to be considered for the next-generation apparatus. The extraction efficiency of the continuous flow buffer gas cell seemed to be very low, it was estimated to be currently only up to 3%. This certainly gives room for improvement. The total flux of cold molecules of about 10^{10}molecules sr^{-1} per shot is comparable to some other buffer gas sources of radicals [76], but it is less than others have reported [109].

The continuous buffer gas source

For the cell with a continuous helium flow, it was seen in measurements of the obtained flux versus the helium flow rate, that the flux went up with increasing helium flow, before stagnating at a certain level. It was suggested that this was due to turbulent flow inside the buffer gas cell that restricted a further increase of extraction efficiency with flow. From

absorption images inside the cell it was further seen that there was a significant density gradient across the cell. To increase the helium number density far above 22 sccm to see if this would increase the molecular flux significantly was not possible due to a limit in pumping speed of the charcoal sorption pumps. To investigate this, a higher surface area of charcoal covered surfaces would be required. The aim to enhance extraction efficiency is to match this flow volume to the size of the cell or the volume occupied by the molecules in the cell, thereby flushing all molecules out of the cell before they get a chance to stick to the walls. A first improvement was made by switching the helium inlet from the same side as the cell aperture to the opposite side. This shows that the overlap between the molecular cloud and the helium flow region was increased as a significantly higher number of molecules was swept out in a shorter time and did not need to diffuse through background gas to reach the flow region. By comparing the diffusion time to the pump out time of helium, one can see that the ratio of the two is inversely proportional to the length of the cell, $\frac{\tau_D}{\tau_p} \propto \frac{F}{L}$, which means that in order to get the highest number of molecules out of the cell before they stick to the walls, it is advantageous to have a smaller cell. The lower limit to the cell length is then given by the thermalisation distance (eqn. 4.2), which for typical densities used in this thesis ranged from 3.22 mm down to 0.21 mm.
Most beams reported in this thesis had forward velocities around the hydrodynamic limit of helium at 4 K. If lower forward velocities are required, the helium flow either needs to be reduced, which also reduces the molecular flux, or alterations to the cell need to be made. A possibility would be a two stage cell, as described in reference [78]. The first cell holds a high enough number density of helium atoms to sufficiently thermalise and extract a high enough number of molecules with a boosted forward velocity into a second cell. This cell is relatively open, to allow a lower helium density. While the second cell still has enough helium to have a few collisions with the molecules, the number of collisions in the extracted beam is small.

The pulsed buffer gas source

The open cell set-up with the pulsed valve, allowed to create a nice narrow molecular pulse shape. However the forward velocity measured corresponded to a higher helium temperature than 4K. This was probably due to a heating of the gas by the solenoid valve. This means that in order for this set-up to achieve lower forward velocities, either alterations to the valve or the cell need to be made. As the cell was very open, and just built of a thin walled copper cylinder to prevent all molecules from being blasted away, the helium gas did not have much chance to rethermalise to the temperature of the copper walls. Making a smaller or more closed cell might help to solve this problem. In section 4.7 it was shown that the time constant for heat conduction decreases with decreasing cell size, therefore a smaller cell leads to quicker rethermalisation of the buffer gas. The energy dumped into the system by ablation has no effect on the copper cell, as even the thin walled cell has enough heat capacity that no significant temperature changes are observed for the

typical ablation powers used. Another way to reduce the gas temperature would be to cool the valve more efficiently. Although the pulsed valve has been mounted with its face onto the cold plate, the inner body of the valve was still heated up by the solenoid. This problem can be solved by making alterations to the valve. A variation to both sources would be the use of a different buffer gas such as neon. It has the advantage that if all other surfaces apart from the cell are kept at 4 K, they act as effective pumps for neon. This would forego the need for charcoal sorption pumps and allow a running time of the experiment that is not limited by that. Furthermore it is shown in [81] that due to this easier pumping of neon, the molecular source seems much more stable and repeatable compared to using helium. Although the cell has to be kept at higher temperatures, due to the higher mass of neon, the forward velocity is not increased too much; at the respective boiling points at 1bar, the hydrodynamic limit of neon at 27 K is 237 ms^{-1} compared to 203 ms^{-1} for helium at 4K. From the Maxwell-Boltzmann distribution a reduction in flux in the N=0 level of 9 times is expected for using neon instead of helium, however in reference [81] it was shown that the flux using neon was very similar to that obtained using helium because of the rotational cooling in the expansion.
Another effect that has the potential to reduce the molecular flux, is the creation of clusters. Although it is difficult to know when clustering becomes a problem, an empirical parameter has been found which predicts the onset of clustering and the cluser size created. It is called the Hagena parameter and is given by [122, 124, 125, 126]:

$$\Gamma^* = \frac{k(d/\tan\alpha)^{0.85}}{T_0^{2.29}} p_0 \tag{7.1}$$

where d is the diameter of the nozzle, T_0 and p_0 are the stagnation parameters and α is the expansion half angle of the source. k is a constant related to bond-formation and a list of these parameters for commonly used gases is given in [122]. While it is 3.85 for helium, it is 185 for neon, which means that the tendency to from clusters is much greater. It is suggested that clustering sets in for a Hagena parameter between 100 and 300. For a typical buffer gas source, where the pressure in the cell is typically less than 1mbar, clustering is not a problem for either species. If a pulsed valve is cooled down to cryogenic temperatures and operated at backing pressures exceeding 1bar (as is usual), clustering can become a problem for helium but much more so for neon. For the respective boiling points, assuming a backing pressure of 1 bar, a valve orifice of 0.5mm and a typical expansion half angle of 32° for a supersonic source, the Hagena parameter is 224 for helium and 1598 for neon.

7.3.2 Guiding and trapping of molecules

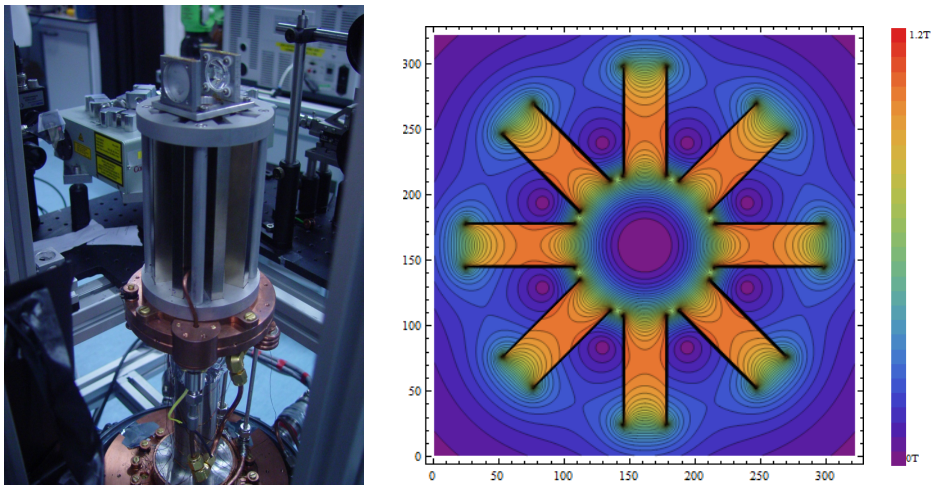
Ground state YbF molecules have a magnetic moment of $1\mu_\mathrm{B}$, which makes them suitable for magnetic trapping. That magnetic trapping and buffer gas cooling work very well together has been shown in references [8],[127],[121],[16],[38], where the buffer gas cell was

placed in the middle of a trapping field created by superconducting magnets. The field created by these magnets was usually between 3 and 4 T, which yields for a species with a magnetic moment of $1\mu_B$, a trap depth of 2 K-2.7 K.
Instead of using superconducting magnets, which are big and require liquid helium, permanent magnets can be used for either traps or guides. Using NdFeBr magnets, trap depths of about 0.6 T can be achieved, which is equivalent to 0.4 K for molecules with a magnetic moment of $1\mu_B$. In order to ensure long trapping lifetimes, a few requirements have to be fulfilled. It is crucial that the helium buffer gas is pumped away from the trap region as quickly as possible to avoid inelastic collisions that flip the spin and thus eject the molecules out of the trap. Ideally the elastic cross-section of the molecule should be a few orders of magnitude higher than the cross-section for spin-flip collisions to ensure efficient thermalisation, while avoiding trap loss through collisions. It is therefore important to create the trap as open as possible to ensure fast helium pump out time. A short, high density pulse of helium could be ejected into the open trap shortly before loading of the molecules by laser ablation.
The field due to a multipole magnetic guide can be dervied from a scalar potential of the form

$$V = \text{const}\, r^n \cos(n\phi) \tag{7.2}$$

where $\mathbf{H} = -\nabla V$, r and ϕ are the usual cylindrical coordinates, and n is 2, 3, 4 for a quadrupole, hexapole, octupole and so on. The magnetic field is proportional to r^{n-1}. This means that for a quadrupole guide the magnetic field grows linearly from the centre to the faces of the magnets. However all these configurations have an area of zero field in the middle. As the force on molecules inside the traps is given by $F = \nabla(\mu \cdot \mathbf{B})$, the orientation of the magnetic moment with respect to the field should be preserved as the molecules move around in the trap. This adiabatic following of the magnetic moment is especially critical where the field is small and hence the energy separation between trappable and untrappable states is small. Let us assume for simplicity a quadrupole trap. To briefly look at the motion inside this trap, stable circular orbits in one plane, can be found by equating $\mu\nabla B = Mv^2/r$. Gradients that can be achieved with permanent magnets for quadrupole traps are typically up to about 50T/m. Assuming that opposite pole faces are a few cm apart, and using the mass of YbF, trappable velocities are a few m/s and molecules in the trap have frequencies of tens of Hz or hundreds of rad/s. In order for the motion to be adiabatic, the Larmor precession rate $\mu B/\hbar$ has to be a lot bigger than the angular trap frequency $\frac{v}{r} = \frac{|dB/dt|}{B}$. We find that the radius of the molecule's orbit has to be greater than a few 10^{-8} m and the velocity has to be greater than about 1cm/s. This shows that the loss volume due to these Majorana transitions is fairly small for a typical quadrupole trap. For higher multipole traps, these losses can become more substantial as there is a bigger region of very small magnetic field in the middle. An example of loading a permanent magentic trap from a Stark decelerator is given in reference [41], where two magnetic ring disks were used to create a quadrupole trapping field. To avoid a zero field

in the middle Tollet et al. [128] have designed a Ioffe-Pritchard equivalent for permanent magnets. This however comes at a cost of very low trap depth which in their case was only 0.01T.



(a) (b)

Figure 7.1: Picture of (a) magnetic octupole guide built from 8 NdFeBr magnets with a remanence field of 1.2T and (b) its calculated magnetic field in radial direction

In order to guide out YbF molecules away from the buffer gas cell and to seperate them from the helium, a magnetic octupole guide was built, shown in figure 7.1. As we wanted to have optical access inside the guide, the magnets were pulled slightly apart from each other, so that there was a gap of about 3mm between adjacent magnets. This reduced the guide depth to about 0.5T, still presenting a depth of 0.34K for YbF molecules.
This guide is ready to be tested. It can then either be loaded by placing it on top of a buffer gas cell or by ablating a target directly inside the guide. In both configurations it may be advantagous to use a pulsed buffer gas source rather than a continuous beam to avoid molecules being kicked out of the guide by inelastic collisions with the background buffer gas. As permanent magnets have the inconvenience of not being able to switch them on and off, it can be difficult to see if molecules are guided when only a straight guide is used, espescially if a few Zeeman components of a certain hyperfine level are guided and a few are not. A possibility to check if the guide is effective is to use a molecule or atom with a convenient hyperfine structure. One example would be ^{7}Li, where at 4K, two hyperfine components of the ground state corresponding to F=1,2 can be resolved. At zero field the hyperfine interval is 800MHZ. When the atom moves adiabatically from zero field into a high field, high enough that the Zeeman splitting is much larger than this hyperfine interval, all but one m_F state of the F=2 state is low-field seeking and can therefore be guided [129]. This means that by looking at the relative heights of the two components at the end of the guide,it should be possible to measure the guide's effectiveness.

Appendix A

Rotational line strengths

In order to evaluate and compare population in different rotational levels,to obtain a rotational temperature, the line strengths of different transitions need to be considered. To compare the intensities of different lines, the whole spectrum of one transition is either integrated over in case of absorption measurements in the cell or the fitted amplitudes of the two resolvable peaks are taken in case of the fluourescence experiments performed on the YbF beam. In any case, in order to compare the strengths of different rotational levels with different quantum number N, the hyperfine structure can be neglected and is therefore not included in the following calculations.
As described in chapter 3, the coupling of the excited $^2\Pi_{1/2}$-state that can be described by Hund's case (a) has a lambda doublet splitting, giving a state with even (e) and a state with odd parity (f) for a particular J' state. In terms of its good quantum numbers $|\Lambda, S, \Sigma, \Omega, J\rangle$,these states are:

$$|e\rangle = \frac{1}{\sqrt{2}}|1, 1/2, -1/2, 1/2, J'\rangle + (-1)^{J'-S}\frac{1}{\sqrt{2}}|-1, 1/2, 1/2, -1/2, J'\rangle \tag{A.1}$$

$$|f\rangle = \frac{1}{\sqrt{2}}|1, 1/2, -1/2, 1/2, J'\rangle - (-1)^{J'-S}\frac{1}{\sqrt{2}}|-1, 1/2, 1/2, -1/2, J'\rangle \tag{A.2}$$

The good quantum numbers to express the ground state, which has Hund's case (b) coupling are $|\Lambda, N, S, J\rangle$, where Λ can be omitted as it is 0. It is possible to express the basis functions of one Hund's case coupling case in terms of those of another one. Therefore the ground state is written in Hund's case (a) basis [130].

$$|N, S, J\rangle = \sum_{\Sigma=-S}^{+S}(-1)^{J-S+\Lambda}(2N+1)^{1/2}\begin{pmatrix} S & N & J \\ -\Sigma & -\Lambda & \Omega \end{pmatrix}|\Lambda, S, \Sigma, J, \Omega\rangle \tag{A.3}$$

This gives for $|S| = 1/2$:

$$|N, 1/2, J\rangle = (-1)^{J-1/2}(2N+1)^{1/2}\begin{pmatrix} 1/2 & N & J \\ 1/2 & 0 & -1/2 \end{pmatrix}|0, 1/2, -1/2, J, -1/2\rangle + (-1)^{J-1/2}(2N+1)^{1/2}\begin{pmatrix} 1/2 & N & J \\ -1/2 & 0 & 1/2 \end{pmatrix}|0, 1/2, 1/2, J, 1/2\rangle \quad \text{(A.4)}$$

This can be further simplified by using equation 5.85 from reference [130] to flip the signs of the projections in the Wigner 3j-symbols and factorise them:

$$|N, J\rangle = (-1)^{J-1/2}(2N+1)^{1/2}\begin{pmatrix} 1/2 & N & J \\ 1/2 & 0 & -1/2 \end{pmatrix} \Big[|0, 1/2, -1/2, J, -1/2\rangle + (-1)^{J+1/2+N}|0, 1/2, 1/2, J, 1/2\rangle\Big] \quad \text{(A.5)}$$

Evaluating the Wigner 3j-symbols with the help of Mathematica for $J = N \pm 1/2$ then gives the final answer

$$|N, N \pm 1/2\rangle = \frac{1}{\sqrt{2}}|0, 1/2, 1/2, J, 1/2\rangle \mp \frac{1}{\sqrt{2}}|0, 1/2, -1/2, J, -1/2\rangle \quad \text{(A.6)}$$

The parity of the ground state changes with N as $(-1)^N$. After having obtained an expression for the ground and excited states in the same basis, the squared matrix elements $\langle \Lambda, S, \Sigma, \Omega, J, m_J|T_p^1(\mathbf{d})|\Lambda', S, \Sigma', \Omega', J', m_{J'}\rangle$ will give the line strenghts of the individual transitions, where $T_p^1(\mathbf{d})$ is the dipole moment operator in the space-fixed cooridnate system. Using the Wigner-Eckhart theorem, the angle dependent part can be factored out as:

$$\langle \Lambda, S, \Sigma, \Omega, J, m_J|\mathbf{T}_p^k(\mathbf{d})|\Lambda', S, \Sigma', \Omega', J', m_{J'}\rangle = (-1)^{J-m_{J'}}\begin{pmatrix} J & k & J' \\ -m_J & p & m_{J'} \end{pmatrix}\langle \Lambda, S, \Sigma, \Omega, J||\mathbf{T}^k(\mathbf{d})||\Lambda', S, \Sigma', \Omega', J'\rangle \quad \text{(A.7)}$$

As we are looking at the decay routes from the upper state, the angular factor can be simplified beacuse the polarisation of the photons is not important. Therefore taking the square and summing over all possible Δm_J transitions gives a prefactor of:

$$\sum_{M_J=M_{J'}-1}^{M'_J+1}\begin{pmatrix} J & 1 & J' \\ -m_J & m_J - m_{J'} & m_{J'} \end{pmatrix}^2 = \frac{1}{2J'+1} \quad \text{(A.8)}$$

A simpler form of the reduced matrix element $\langle \Lambda, S, \Sigma, \Omega, J||\mathbf{T}_p^k(\mathbf{d})||\Lambda', S, \Sigma', \Omega', J'\rangle$ can be obtained by transforming the dipole operator into the molecular fixed coordinate system.

The dipole operator transforms as (eqn. 5.143 [130]):

$$T_p^1(\mathbf{d}) = \sum_p D_{pq}^1 T_q^1(\mathbf{d}), \tag{A.9}$$

where D_{pq} are the elements of the rotation matrix. The dipole moment operator in the molecular fixed frame T_q^1operates on the spatial coordinates of the electrons. Hence with the help of eqn. 5.186 ([130]) the reduced matrix element can be written as:

$$\sum_q \langle \Omega, J | D_{pq}^1 | \Omega', J' \rangle \langle \Lambda, S, \Sigma | T_q^1 | \Lambda', S, \Sigma' \rangle =$$
$$\sum_q (-1)^{J-\Omega} \begin{pmatrix} J & 1 & J' \\ -\Omega & q & \Omega' \end{pmatrix} [(2J+1)(2J'+1)]^{1/2} \langle \Lambda, S, \Sigma | T_q^1 | \Lambda', S, \Sigma' \rangle \tag{A.10}$$

The total electronic angular momentum in the ground state $\Omega = \pm\Sigma = \pm 1/2$. As $\Sigma' = \Sigma$ and the orbital angular momentum of the excited state is $\Lambda = 1$, $\Omega' = \Omega \pm 1$, where we are only considering the transitions to the $|\Omega'| = 1/2$ fine structure state. The matrix elements can be labelled as $m(\Omega', \Omega)$ with $m(1/2, 1/2) = m(-1/2, -1/2) = 0$. For the off-diagonal matrix elements, the Wigner 3j-symbols in equation A.10 will only ever be nonzero for one value of q (-1 or +1) to satisfy $\Omega' = \Omega \pm 1$. The matrix element $m(-1/2, 1/2)$ can again be written in terms of the 3j-symbols of $m(1/2, -1/2)$ using equation 5.85 from [130]. This gives the off-diagonal matrix elements as:

$$m(1/2, -1/2) =$$
$$(-1)^{J'-1/2} \sqrt{(2J+1)(2J'+1)} \begin{pmatrix} J & 1 & J' \\ 1/2 & 1 & 1/2 \end{pmatrix}$$
$$m(-1/2, 1/2) =$$
$$(-1)^{J'+J+1} (-1)^{J'-1/2} \sqrt{(2J+1)(2J'+1)} \begin{pmatrix} J & 1 & J' \\ -1/2 & 1 & -1/2 \end{pmatrix} \tag{A.11}$$

where the last factor in equation A.10 is omitted as it is common for every branch. Using this matrix and the expression for the ground and excited state as given above, the line strengths for all rotational levels can be calculated for all $\Delta J, \Delta N$ values. For N=0-50, the results are shown in figure A.1.

At low N, graph A.1 shows a decrease in linestrengths for the Q_{11} and ${}^{O}P_{12}$ branch and an increase for the ${}^{Q}R_{12}$ branch for increasing N. However at $N = 20$, the line strengths have nearly approached their asymptotic value of 0.5 for the Q_{11} branch and 0.25 for the ${}^{Q}R_{12}$ and ${}^{O}P_{12}$ branch.

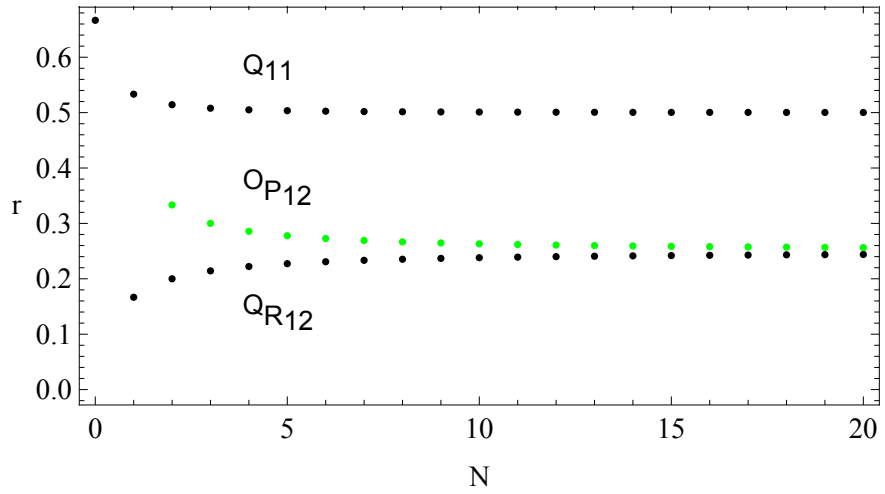


Figure A.1: Linestrengths for the Q_{11}, ${}^{Q}R_{12}$, ${}^{O}P_{12}$ rotational transitions as a function of rotational number N

Appendix B

Flow Regimes

To obtain a cold molecular beam using the buffer gas technique, an orifice is put into one side of the buffer gas cell from where the molecules and the helium can escape. The gradient of buffer gas density between the inside of the cell and the guard vacuum then determines the flow regime. A way to distinguish flow regimes is by using a parameter called the Knudsen number. It is the ratio between the mean free path λ and a characteristic dimension L of the flow field,

$$K_{\mathrm{n}} = \frac{\lambda}{L}. \tag{B.1}$$

If $K_{\mathrm{n}} \ll 1$, the gas is said to be in the continuous flow regime and for $K_{\mathrm{n}} > 3$ in the free molecular flow regime. In the continuous flow regime collisions between molecules or molecules and atoms are dominant, whereas in the latter, the only collisions considered are possible molecule-wall collisions.

Another quantity, which becomes important in the continuous regime is the Reynold's number which is given by:

$$R_{\mathrm{e}} = \frac{u\rho L}{\mu}, \tag{B.2}$$

where u is a characteristic flow velocity, μ is the viscosity and ρ the density of the fluid. It is a measure between inertial and viscous forces, where a high Reynolds number means that viscous forces are negligible. If the Reynolds number goes above a critical value, the flow turns from laminar to turbulent as viscous forces are responsible for the damping of flow instabilities. By taking the viscosity for a gas of hard spheres $\nu = \frac{1}{3}\rho\bar{v}\lambda$ and using the definiton of the Mach number B.14, a relation between Reynolds number and Knudsen number can be found as:

$$K_{\mathrm{n}} = \frac{3}{2}\sqrt{\pi 2\gamma}\frac{M}{R_{\mathrm{e}}}. \tag{B.3}$$

B.1 Effusive Regime

The velocity distribution of the molecules in the cell can be described by the Maxwell Boltzmann distribution as

$$f(v)dv = \frac{4}{\sqrt{\pi}}\Big(\frac{m}{2k_BT}\Big)^{3/2} v^2 e^{-\frac{mv^2}{2k_BT}} dv = \frac{4}{\sqrt{\pi}} x^2 e^{-x^2} dx, \tag{B.4}$$

where $x = \frac{v}{v_\mathrm{p}}$ and $v_\mathrm{p} = \sqrt{\frac{2k_\mathrm{B}T}{m}}$ is the most probable velocity. On one of the sides of the cell is an aperture of a certain area A and thickness L(which is for now assumed to be negligible) from where the molecules and the buffer gas can escape. The pressure inside the cell is kept low enough that the mean free path λ is larger than the diameter and thickness of the orifice and hence molecular flow conditions are ensured. This means that the thermal equilibrium of the particles inside the cell is not appreciably disturbed by the aperture. Collisions inside the aperture can be neglected and in order to estimate the flux coming out of the cell, only the average number of molecules impinging on an area element dA during time dt has to be calculated. Consider those molecules exiting the cell into the solid angle element $\mathrm{d}\omega = \sin(\theta)d\theta d\phi$ with a speed between v and $v + dv$. Only those molecules in the volume $dV = v\cos\Theta dAdt = v_\mathrm{p} x\cos\theta dAdt$ can hit the area element dA during time dt. If the number density in the cell is n, the number of molecules hitting dA during time dt is

$$dN = n\frac{d\omega}{4\pi} f(v)dvdV = n\frac{d\omega}{4\pi} f(v)v\cos\theta dA\, dt\, dv \tag{B.5}$$

Inserting the velocity distribution gives a flux exiting the cell into the solid angle element $d\omega$ of:

$$\frac{dN}{dt} = I(\theta, x)d\omega = \frac{nd\omega}{\pi^{3/2}} v_\mathrm{p} x^3 e^{-x^2} dx\cos\theta dA. \tag{B.6}$$

The speed distribution of the flux is therefore proportional to $x^3e^{-x^2}$, which is the distribution, a flux detector such as a pmt will detect. It shows that the probability for particles to be extracted from the cell scales with the velocity. The most probable velocity and average velocity of the effusive beam is

$$v_\mathrm{p,eff} = 1.22 v_\mathrm{p}, \tag{B.7}$$

and

$$\bar{v}_\mathrm{eff} = 1.33 v_\mathrm{p}. \tag{B.8}$$

To determine the total particle flux into the solid angle element $d\omega$, the average molecular velocity $\bar{v} = \frac{2}{\sqrt{\pi}} v_\mathrm{p}$ is introduced and equation B.5 is integrated over all velocities:

$$I(\theta)d\omega = \frac{n\bar{v}}{4}\frac{d\omega}{\pi}\cos\theta dA. \tag{B.9}$$

It is seen that for an effusive source with an ideal aperture, the angular distribution of molecules follows a cosine law. To calculate the flux close to the aperture, eqn. B.9 has to be integrated over the total area A. For the far-field flux dA can just be replaced with A. The total flux of particles leaving the orifice per unit time is then obtained by integrating over the forward hemisphere,

$$\frac{dN}{dt} = \phi = \frac{n\bar{v}A}{4}. \tag{B.10}$$

In the forward direction, the flux of molecules is (molecules sr^{-1} s^{-1}):

$$\phi(0) = \frac{n\bar{v}}{4\pi}A. \tag{B.11}$$

An important quantity is the brightness of a molecular beam, which is defined as the particle flux per unit area effusing in the forward direction into the unit solid angle. The most common shapes for thin-walled apertures are either circles or slits. Slits are the preferred option, as for a circular orifice the maximum intensity achieveable in the molecular flow regime is obtained for $A = \pi\lambda^2$, which means the maximum forward intensity is inversely proportional to the pressure. However for a slit of height h, $A = h\lambda$, which means that the maximum forward intensity is independent of pressure and increases linearly with the height of the slit.

An option to alter the cosine law, which defines the angular spread of molecules in an effusive source, is to use channels instead of thin apertures. If a channel with length L and radius r is considered, λ has to be bigger than L (Knudsen number $\frac{\lambda}{L} >> 1$) to ensure free molecular flow. In this case only wall collisions and not intermolecular collisions have to be taken into account. To calculate the flow properties of a channel, a knowledge of the wall collision rate is required. This wall collision rate can not be calculated analytically, however the Clausing function published in 1932 [131] can be solved numerically [56], [132]. Having an expression for the collision rate, the angular spread can be determined geometrically. The derivation will not be given here but can be found in reference [132]. Particles that leave the channel exit under an angle θ, where two angular regions can be distinguished. Particles emerging from the exit under an angle $|\theta| < \beta$, where $\beta = \frac{2r}{L}$, have gone straight through the channel without collsions or have had a few wall collisions, whereas particles exiting the channel at angles $|\theta| > \beta$ must have had wall collisions. As the parameter β and hence the dimensions of the channel are varied, one can tune the angular spread of the effusive source from a cosine law ($\beta = \infty$) to a more forward peaked distribution. For $\beta<1$, the angular distribution already shows a peak in the forward direction, however for larger angles broad wings can be seen. If β is then decreased further, the forward peak becomes narrower, the intensity in the wings is reduced and if $\beta \ll 1$ the half width half maximum of the beam profile becomes proportional to β. The intensity in the forward direction compared to the total number of effusing molecules can then be written as a function of the transmission probability W which is inversely proportional to the peaking

factor $k = \frac{1}{W}$:

$$\frac{I(0)}{I} = \frac{1}{\pi W}. \tag{B.12}$$

Solutions to Clausing's equation show that for $\frac{L}{2r} \gg 1$ the transmission probability approaches $W = \frac{8r}{3L}$ [56] and the relative forward intensity therefore increases linearly with $\frac{1}{\beta}$.

For a channel operated in the transparent regime, the modest extraction efficiency of an effusive source is further decreased by the transmission probability factor W. Therefore although the optimum collimation is obtained in the collision free flow, channel sources are often operated at higher pressures to obtain higher peak intensities. For a Knudsen number of $\beta \leq K_\mathrm{n} < 10$, intermolecular collisions have an insignificant effect on the total flow but affect the angular distribution and hence the centreline intensity. If the pressure is increased further hydrodynamic effects become important [56],[132]. The regime of continuous flow as opposed to free molecular flow will be investigated in the next section.

B.2 Supersonic Regime

So far sources were described that could be approximated by a free molecular flow model. Although collimated and slow sources can be achieved in that way, the overall beam intensities are rather modest. In this section, sources will be introduced that work with a higher base pressure. If the pressure gradient between the gas reservoir and the surrounding is high enough, the buffer gas and hence the molecules will be accelerated to supersonic velocities. Supersonic sources operate in the continuous flow regime, which means that collisions between molecules dominate over molecule-wall collisions. The flow can be described by the macroscopic quantities temperature T, pressure p, density ρ and the fluid velocity $\mathbf{u}$. This section will describe how a gas can be accelerated to supersonic velocities and estimate the maximum attainable velocity. The effect of different values of background pressure on the gas flow will be discussed as well as the effect of a skimmer. Having established the main characteristics of such sources, the thermalisation of a polyatomic gas diluted in a buffer gas will be discussed.

The source is principally made of a nozzle connected to a gas reservoir that leads into a evacuated chamber with background pressure p_b. As the dimensions of the gas reservoir are much larger than those of the nozzle, the parameters $p_0, \rho_0, T_0, u = 0$ can be assumed to be constant and are called the stagnation parameters. For simplicity, it is assumed that the gas (compressible flow) is perfect, inviscid and that there is no heat exchange with the surrounding which makes the flow isoentropic, meaning that the entropy is constant along a particular streamline. The flow parameters are assumed to not change over time but only depend on spatial coordinates of the flow field, thereby describing a stationary flow. Furthermore the flow is for now assumed to be axisymmetric with the nozzle axis (x-axis) coinciding with the central streamline.

Before describing supersonic flow, the sonic velocity in a gas needs to be introduced.

$$a = \sqrt{\gamma \frac{k_B T}{m}} \tag{B.13}$$

Knowing the speed of sound for a certain gas, the Mach number is defined as the ratio of the local values of flow speed u and speed of sound a,

$$M = \frac{u}{a}, \tag{B.14}$$

and therefore $M < 1$, $M = 1$ and $M > 1$ corresponds to subsonic, sonic and supersonic flow respectively. To find the maximum attainable velocity u_∞ of the gas for isoentropic flow, we look at the conservation of energy. For an ideal compressible fluid, this is given by the Bernoulli theorem:

$$\frac{u^2}{2} + h + gz = \text{const} \tag{B.15}$$

where h is the enthalpy and g is the gravitational constant. The constant on the right hand side is different for different streamlines, unless the flow is also irrotational ($\nabla \times \mathbf{u} = 0$), which then makes it homoentropic. For infinitesimal variations and ignoring gravity, which plays no significant role in the experiments considered here, this becomes:

$$d\left(\frac{u^2}{2}\right) + dh = d\left(\frac{u^2}{2}\right) + \frac{k_B}{m}\frac{\gamma}{\gamma - 1} dT = 0, \tag{B.16}$$

where $\gamma = 5/3$ for a monoatomic gas and the relation $dh = c_p dT$ was used, c_p being heat capacity per unit mass at a constant pressure:

$$c_p = \frac{k_B}{m}\frac{\gamma}{\gamma - 1}. \tag{B.17}$$

Integrating eqn. B.16 over two specific points of the flow field, where the variables are $(p_0, \rho_0, T_0, \mathbf{u}_0)$ and $(p, \rho, T, \mathbf{u})$ gives:

$$\frac{u^2}{2} - \frac{u_0^2}{2} + \frac{\gamma}{\gamma - 1}\frac{k_B}{m}(T - T_0) = 0 \tag{B.18}$$

Using eqn. B.13, this can be rewritten as

$$\frac{u^2}{2} + \frac{a^2}{\gamma - 1} = \frac{u_0^2}{2} + \frac{a_0^2}{\gamma - 1} = \text{const}, \tag{B.19}$$

and using the Mach numbers $M = u/a$,$M_0 = u_0/a_0$:

$$a^2\left(1 + \frac{\gamma - 1}{2} M^2\right) = a_0^2\left(1 + \frac{\gamma - 1}{2} M_0^2\right). \tag{B.20}$$

When the first point is the stagnation point, $u_0 = 0$ and hence also $M_0 = 0$. This means that the sound velocity anywhere in the flow field can be written as:

$$a = \frac{a_0}{\left(1 + \frac{\gamma-1}{2}M^2\right)^{1/2}}. \tag{B.21}$$

And thus the flow velocity is:

$$u = Ma = \frac{Ma_0}{\left(1 + \frac{\gamma-1}{2}M^2\right)^{1/2}}. \tag{B.22}$$

To obtain the maximum possible flow velocity u_∞ in a perfect isoentropic gas, the limit $M \to \infty$ has to be taken:

$$\lim_{M\to\infty} u = u_\infty = a_0\sqrt{\frac{2}{(\gamma-1)}}. \tag{B.23}$$

The other flow parameters can be determined from eqn. B.21 by using eqn. B.13 and the adiabatic relations $p = p_0\left(\frac{T}{T_0}\right)^{\frac{\gamma}{(\gamma-1)}}$, $\rho = \rho_0\left(\frac{T}{T_0}\right)^{\frac{1}{(\gamma-1)}}$:

$$T = \frac{T_0}{\left(1 + \frac{\gamma-1}{2}M^2\right)}, \tag{B.24}$$

$$p = \frac{p_0}{\left(1 + \frac{\gamma-1}{2}M^2\right)^{\gamma/(\gamma-1)}}, \tag{B.25}$$

$$\rho = \frac{\rho_0}{\left(1 + \frac{\gamma-1}{2}M^2\right)^{1/(\gamma-1)}}. \tag{B.26}$$

Sometimes it is useful to determine the velocity as a function of the pressure at a certain point in the flow field. Using the Bernoulli theorem B.18 $c_pT + \frac{u^2}{2} = c_pT_0$, u can be expressed in terms of temperature. Expressing c_p with eqn. B.17, making use of the adiabatic relation between temperature and pressure and the expression for the speed of sound (eqn. B.13), then leads to the Saint-Venant and Wantzel equation:

$$u = a_0\sqrt{\frac{2\gamma}{\gamma-1}\left(1 - \left(\frac{p}{p_0}\right)\right)^{(\gamma-1)/\gamma}}. \tag{B.27}$$

Although the maximum achievable velocity in an isoentropic flow has been determined, the conditions for obtaining this flow still have to be found.
The gas flow rate crossing the nozzle is described by the continuity equation for stationary

flow $\nabla(\rho\mathbf{u}) = 0$. Integrating this equation over a volume in the nozzle between the two cross-sections with areas $A_1 = A(x_1)$ and $A_2 = A(x_2)$ and applying the divergence theorem gives, where S is the surface enclosing the volume V:

$$\int_V \nabla(\rho\mathbf{u})dV = \int_S \rho\,\mathbf{u}\cdot\mathbf{n}\,dS = \rho_2 A_2 u_2 - \rho_1 A_1 u_1 = 0. \tag{B.28}$$

This shows that the mass flow rate is constant:

$$F = \frac{dm}{dt} = \rho A u = \text{const} \tag{B.29}$$

Logarithmically differentiating eqn. B.29 and using eqn. B.13 gives:

$$\frac{dp}{a^2\rho} + \frac{dA}{A} + \frac{du}{u} = 0. \tag{B.30}$$

Again using the Bernoulli eqn.B.16 with the expression for the specific enthalpy for isoentropic flow $dh = \frac{dp}{\rho}$ gives

$$\frac{dp}{\rho} = -udu = -u^2\frac{du}{u} \tag{B.31}$$

which inserted into B.30 and using the definition of the Mach number yields:

$$\frac{du}{u} = \frac{1}{M^2-1}\frac{dA}{A}. \tag{B.32}$$

To determine the effect of varying cross-section on the other flow parameters, the relation B.31 can be used to obtain the result for p. Logarithmically differentiating the adiabatic relations of p,T and ρ and the equation for the sound velocity B.13 gives then the relations $\frac{dp}{p} = \left(\frac{\gamma}{\gamma-1}\right)\frac{dT}{T}$, $\frac{dp}{p} = \gamma\frac{d\rho}{\rho}$ and $\frac{da}{a} = \frac{1}{2}\frac{dT}{T}$, from which the remaining relations between flow parameters and changing nozzle cross-section dA can be obtained as:

$$\frac{dp}{p} = \frac{1}{(1-M^2)\left[\frac{p}{\rho u^2}\right]}\frac{dA}{A}, \tag{B.33}$$

$$\frac{dT}{T} = \frac{1}{(1-M^2)\left[\frac{\gamma}{\gamma-1}\frac{p}{\rho u^2}\right]}\frac{dA}{A}, \tag{B.34}$$

$$\frac{da}{a} = \frac{1}{(1-M^2)\left[\frac{\gamma}{\gamma-1}\frac{2p}{\rho u^2}\right]}\frac{dA}{A}, \tag{B.35}$$

$$\frac{d\rho}{\rho} = \frac{1}{(1-M^2)\left[\gamma\frac{p}{\rho u^2}\right]}\frac{dA}{A}. \tag{B.36}$$

Equations B.32-B.36 explain how flow parameters change in a converging ($\frac{dA}{A} < 0$) and diverging ($\frac{dA}{A} > 0$) nozzle for subsonic ($M < 1$) and supersonic ($M > 1$) flow. Considering that the expression in square brackets is always positive, it can be seen that for a converging

nozzle and subsonic flow, the flow velocity increases as the area A decreases, while the other flow parameters, such as temperature and pressure decrease. This also means that for subsonic flow, the Mach number increases as the cross-section of the nozzle gets smaller. For a diverging nozzle and subsonic flow, the flow velocity decreases with increasing A, while the other parameters increase. By contrast the flow velocity for supersonic flow decreases for a converging nozzle and increases for a diverging nozzle. All the other parameters such as temperature and pressure increase in the converging nozzle but decrease for a diverging nozzle. This shows that the flow velocity can be accelerated to supersonic values by having a nozzle that is first converging and then diverging. To find the relationship between the Mach number and the cross-section of the nozzle, equations B.26 and B.22 for the density and the flow velocity as a function of M are inserted into the equation for the mass flow rate, which as established above is constant throughout the nozzle. This gives for the ratio of the nozzle cross-sections at two different places:

$$\frac{A}{A_1} = \frac{M_1}{M}\left(\frac{1+\frac{\gamma-1}{2}M^2}{1+\frac{\gamma-1}{2}M_1^2}\right)^{\frac{\gamma+1}{2(\gamma-1)}}. \tag{B.37}$$

Setting A_1 to the critical cross-section $A*$, where $M = 1$ yields

$$\frac{A}{A*} = \frac{1}{M}\left(\frac{1+\frac{\gamma-1}{2}M^2}{\frac{\gamma+1}{2}}\right)^{\frac{\gamma+1}{2(\gamma-1)}}, \tag{B.38}$$

which shows that in a converging-diverging nozzle, the velocity is sonic at the the narrowest part of the nozzle, the throat (figure B.1). Once $A(x)$ is known, $M(x)$ can be calculated.

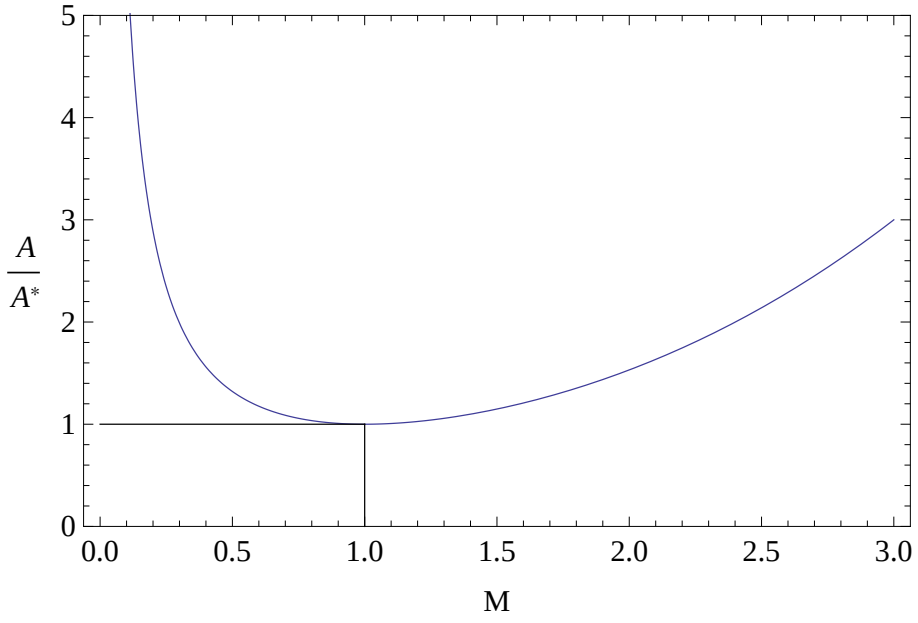


Figure B.1: Relation between nozzle cross-section A normalised to the critical value A^*, and the Mach number M.

As for each $A(x)$ two solutions for $M(x)$ exist, one has to keep in mind whether the nozzle is converging or diverging along the direction of the flow and whether supersonic flow has already been achieved upstream, by a throat in the nozzle. All flow parameters can be expressed in terms of M and by using equations B.22, B.24, B.25, B.26, they can be obtained as well.

To investigate what a change in pressure across the nozzle does to the flow, the mass flow rate B.29 can be written in terms of pressure. This is done by inserting ρ and u as a function of M and then defining M as a function of p as given by equation B.25:

$$F = A\left(\frac{2\gamma p_0\rho_0}{\gamma-1}\left(\frac{p}{p_0}\right)^{2/\gamma}\left[1-\left(\frac{p}{p_0}\right)^{(\gamma-1)/\gamma}\right]\right)^{1/2} \tag{B.39}$$

Differentiating eqn. B.39 with respect to p, the maximum is evaluated to be for p attaining the critical value $p* = \frac{p_0}{\left(\frac{\gamma+1}{2}\right)^{\gamma/(\gamma-1)}}$ (eqn. B.25 for $M = 1$). This happens when the flow velocity becomes sonic. From above it is known that this happens at the throat of the nozzle, hence for $A = A_{\mathrm{th}}$.

$$F_{max} = A_{\mathrm{th}}\sqrt{\gamma p_0\rho_0}\left(\frac{2}{\gamma+1}\right)^{\frac{\gamma+1}{2(\gamma-1)}} \tag{B.40}$$

From this we get the supersonic flux as

$$\phi_{\mathrm{s}} = \frac{dN}{dt} = A_{\mathrm{th}}\sqrt{\frac{2k_{\mathrm{B}}T}{m}}n_0\left(\frac{\gamma}{\gamma+1}\right)^{1/2}\left(\frac{2}{\gamma+1}\right)^{1/(\gamma-1)} \tag{B.41}$$

It has to be noted that this maximum flow rate is an upper limit as it corresponds to that of a perfect gas and real gases are viscous. Usually this is dealt with by introducing a discharge coefficient, which is defined by the ratio of the effective flow rate to the theoretical flow rate.

Equation B.39 is only valid until the critical pressure is reached. If the pressure inside the nozzle becomes even lower than the critical pressure $p < p^*$, the mass flow rate will stay at the maximum value and not as predicted by B.39 decrease again. This is due to the fact that at that point the sonic velocity has been reached and a further reduction of pressure will not effect the distribution of pressure and velocity on the upstream section.

Instead of having a nozzle with a convergent and divergent part, it is possible to only have a convergent nozzle. All above considerations are still valid as the beam can diverge as soon as it exits the nozzle thereby gaining supersonic velocities. This is also called a supersonic free jet and the following discussions will focus on this type of nozzle.

B.2.1 The effect of gas reservoir to background pressure ratio on the flow

From above we know that different flow regimes can be achieved by varying the helium density in the cell with respect to the background density. Furthermore when working in the regime that is best described by continuous flow, the flow structure will change as the background pressure in the discharge chamber is varied with respect to the stagnation pressure p_0.

If the pressure at the exit $p_e < p_0$ but the background pressure $p_b \geq p^*$ then the Mach

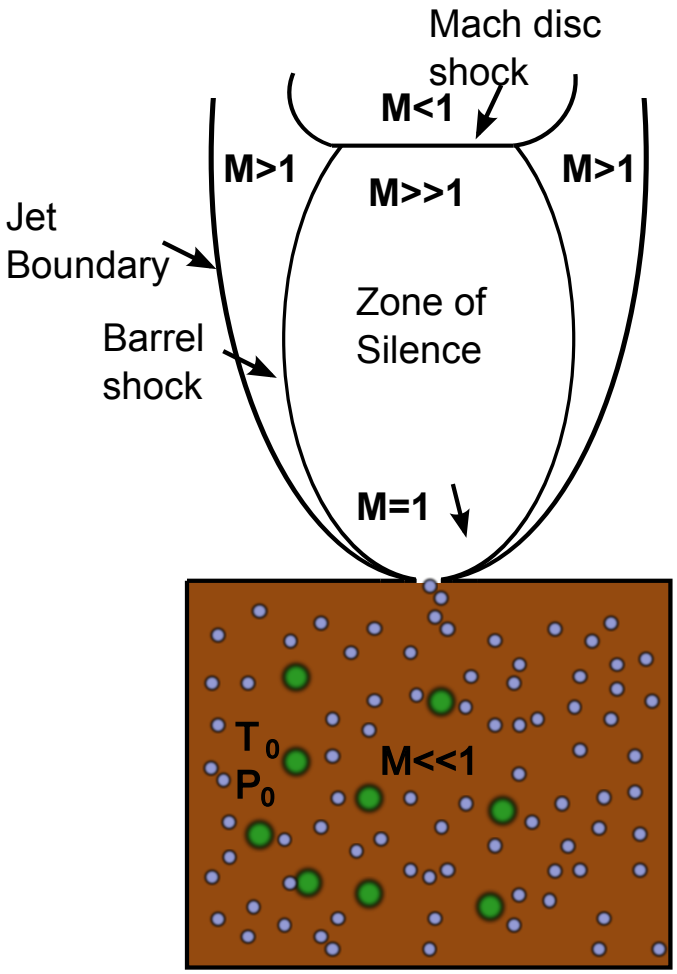


Figure B.2: Shock structure of an underexpanded jet, showing the Mach disk, barrel shock and zone of silence

number is increasing to reach a maximum at the exit. For $p_b > p^*$ the emitted jet will always be subsonic. If p_b is decreased further to the value of the critical pressure, the Mach number will rise to 1 and the flow rate attains a maximum (eqn. B.40). For further decreases of the background pressure, the conditions inside the nozzle will not change anymore. The exit pressure takes the value of p^* and is hence larger than the background pressure and the flow rate stays maximised. As the background pressure is lowered, the

expanding jet develops a shock structure as seen in figure B.2. In the zone of silence the flow is isoentropic and by evaluating M(x,y) numerically, all other flow parameters can be obtained. The ratio p_0/p_b determines the shape and size of the barrel shock and the Mach disc. Experimentally, Ashkenas and Sherman [56] found that

$$\frac{x_\mathrm{M}}{D} = 0.67(p_0/p_b)^{1/2} \tag{B.42}$$

where x_M is the axial coordinate of the Mach disk and D is the diameter of the nozzle. As the background pressure is lowered further, the distance to the Mach disk gets bigger, and the Mach disk and barrel shock region get thicker (diffuse shocks). A further decrease of the background pressure lets the shock structure disappear and the shocks turn into scattering regions between the jet molecules and the background gas. The scattering region is centred around x_M and can be as thick as a few centimetres. Bier and Hagena, Ashkenas and Sherman suggest a Knudsen inequality for which the shock structure disappears [133]:

$$K_M = \frac{\lambda_\mathrm{M}}{D_\mathrm{M}} < (0.1 - 0.3) \tag{B.43}$$

where λ_M is the mean free path behind the Mach disc and D_M is the Mach disk diameter. If condition B.43 is satisfied then a gradual transition from the continuous to the molecular free regime occurs, where collisions are rare and the internal degrees of freedom are frozen out.

Flow parameters in a free supersonic jet

In the isoentropic part of the flow it is enough to know the Mach number as a function of distance from the nozzle in order to determine the other flow variables. They are then found by putting M into equations B.22,B.25,B.26 and B.24. Looking at the variation of flow parameters along the centreline, numerical calculations give solutions for the Mach number for expansions from a hole or a slit, known as axisymmetric and planar expansions respectively. If D is the diameter of the circular orifice or the width of the slit, $X = \frac{x}{D}$ can be defined as the reduced distance from the nozzle. There are two solutions, one for distances $X > 0.5$ and one covering the expansion close to the nozzle being valid in the region $0 < X < 1$.

$$M(X) = X^{\frac{\gamma-1}{\delta}}\left(C_1(\gamma,\delta) + \frac{C_2(\gamma,\delta)}{X} + \frac{C_3(\gamma,\delta)}{X^2} + \frac{C_4(\gamma,\delta)}{X^3}\right) \text{ for } X > 0.5, \tag{B.44}$$

$$M = 1 + A(\gamma,\delta)X^2 + B(\gamma,\delta)X^3 \text{ for } 0 < X < 1. \tag{B.45}$$

As this thesis focuses on the work with helium buffer gas,only the coefficients for $\gamma = 5/3$ relevant to a monoatomic gas are given in table B.1. δ takes the value 1 for an axisymmetric expansion and 2 for a planar expansion.

The calculations that produce the coefficients in table B.1 assume that the slit is infinitely long, For a finite length slit this solution is only adequate when the distance from

Table B.1: Coefficients from MOC calculations to describe the variation of Mach number with distance from the nozzle exit

Coefficients	axisymmetric	planar
$C_1(5/3)$	3.232	3.038
$C_2(5/3)$	-0.7563	-1.6290
$C_3(5/3)$	0.3937	0.9587
$A(5/3)$	3.337	2.339
$B(5/3)$	-1.541	-1.194

the slit is smaller than the slit length. For the experiments described in this thesis, the slit dimensions were 4×0.75mm and therefore the calculations are only valid for $X \leq 5.3$.

Figure B.3 shows how the Mach number and the density change with distance from the nozzle, X, for both axisymmetric and planar expansions. We see that for the axisymmetric case the Mach number increases more rapidly and the density decreases more rapidly with X than for the planar case. This suggests that axisymmetric expansion is favourable for reaching the collision-free regime most rapidly.

The temperature is an important quantity to look at as it is linked to the velocity distribution of the molecules in the jet. As the Mach number increases with the expansion, the temperature decreases as described by equation B.24. The forward velocity distribution of the molecules in the jet can be described with a Maxwell-Boltzmann distribution centred around u:

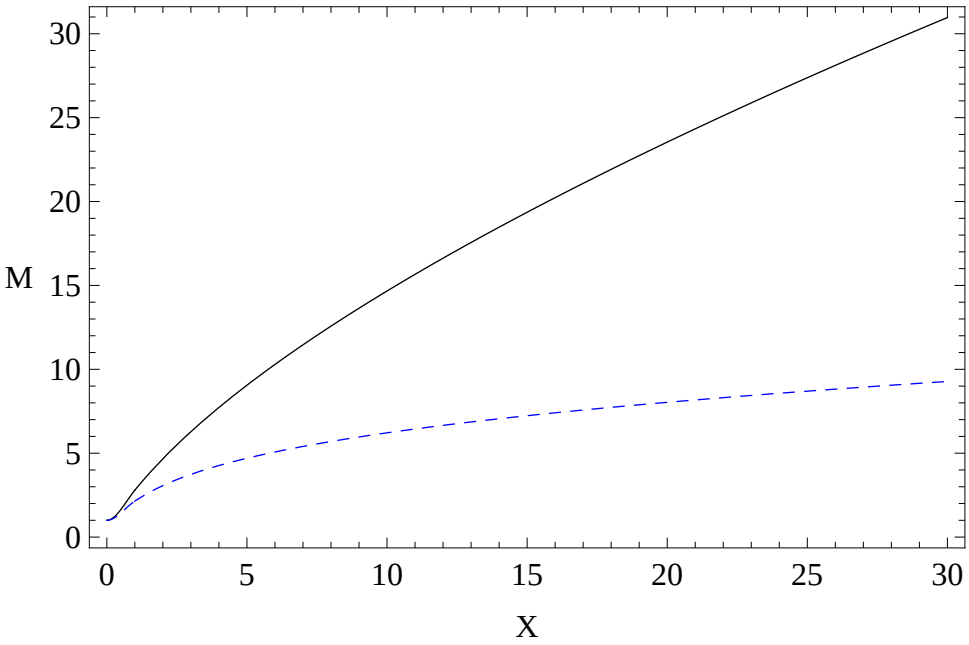
$$f(v) = \left(\frac{M}{2\pi k_B T}\right)^{3/2} e^{-\frac{M}{2k_B T}(v-u)^2} dv^3 \tag{B.46}$$

As the gas expands away from the nozzle temperature meaning that the distribution of speeds around the central speed u becomes narrower.

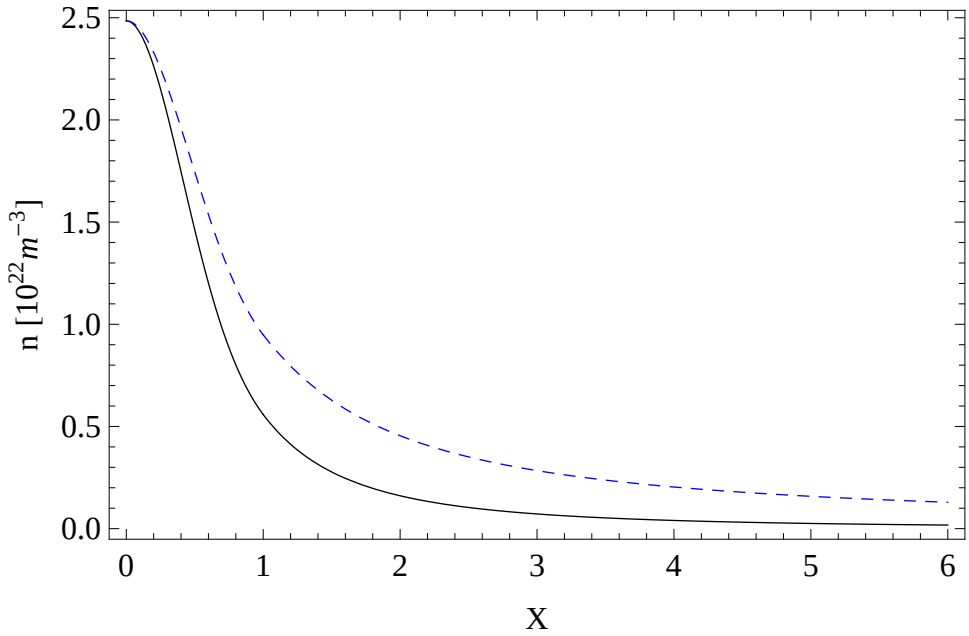
Cooling of a binary mixture in a free jet expansion

It is usual to cool molecules of interest by entraining them in the expanding atomic carrier gas. Then, cooling of the translational, rotational and vibrational degrees of freedom have to be considered. The jet expands and thermal energy is converted into directional kinetic energy making the veloctiy distribution narrower but peaking at a relatively high value u. As the jet expands into the evacuated chamber, the collisons between the molecules and the carrier gas ensure that the beam is nearly monokinetic. As the collisions get rarer, the cooling gets less effective and the temperature reaches its final value. If there are no collisions, atoms with a larger perpendicular velocity $v_\perp$ move away from the jet centre relatively quickly, while those with small values of the perpendicular component stay confined to the axis for larger distances. This has the effect that when considering two apertures of the same size at two different points along the beam line, the one further away from the nozzle will show a narrower transverse velocity distribution.

Thus the width of the longitudinal speed distribution becomes constant ones the collisions have ceased, while the width of the perpendicular speed distribution continuous to



(a) Variation of Mach number with reduced distance from the nozzle exit for axisymmetric (black) and planar (blue, dashed) flow



(b) Decrease of gas density with reduced distance from the nozzle for axisymmetric (Black) and planar (blue, dashed) flow for a helium flow of 10sccm

Figure B.3: Mach number and density as a function of reduced distance from the nozzle for an axisymmetric (black) and a planar(blue, dashed) supersonic expansion

fall.

The rotational degrees of freedom also cool through collisions with the carrier gas and a rotational temperature $T_{\rm rot}$ and relaxation time $\tau_{\rm r}$ can be attributed to them. However the relaxation rate $R_{\rm rot} \propto 1/\tau_{\rm rot}$ is smaller then for translations (see ch. 4) and therefore the rotational temperature freezes out earlier than the translational temperature. For this reason, it is usually found that $T_{\rm rot}$ is somewhat higher than $T_{\shortparallel}$ in a supersonic beam. The rate for vibrational relaxation is usually very much lower than the rates for rotational and translational relaxation, so the vibrational degrees of freedom freeze out first and the vibrational temperature is usually much higher than $T_{\rm rot}$ and $T_{\shortparallel}$. This freezing out of particular degrees of freedom usually occurs gradually, however if it just happens over a short axial distance, the sudden freeze approximation can be made. This means that only two regimes are assumed, the continuous regime and the molecular free one. They are separated by the so-called quitting/freezing surface, at coordinate $X_{\rm F}$, beyond which the flow parameters take the values they have at $X_{\rm F}$ which can be calculated from the equations for the continuous regime (as for the temperature in eqn. B.24). Hence the coordinate $X_{\rm F}$ has to be found.
To estimate where this freezing surface is located, an expression for the collision rate as a function of distance from the nozzle has to be found. For two body collisions, the number of collisions N occuring in the time dt is :

$$dN = \sqrt{2} n \sigma \bar{v} dt. \tag{B.47}$$

Since the flow parameters in the expansion are all a function of the Mach number, of which the spatial dependence is given by equation B.44,n and $\bar{v}$ in eqn.
B.47 become functions of x, the distance from the nozzle. Using equations B.22, B.24 and B.26 and expressing everything in terms of the reduced distance $X = \frac{x}{D}$, where D is the nozzle diameter, the collision rate can be written as:

$$dN = \frac{4}{\sqrt{\pi}} \frac{n_0 \sigma D}{M(X,\delta)\sqrt{\gamma}} \left(1 + \frac{\gamma - 1}{2} M(X,\delta)^2 \right)^{-1/(\gamma-1)} dX \tag{B.48}$$

The number of collisions a molecule has from a point X_0 onwards gives an estimate of the point at which the continuum description breaks down. The number of remaining collisions is found by integrating B.48 from X_0 to infinity, hence:

$$N = \frac{4}{\sqrt{\pi}} \sigma n_0 D F_{\rm hs} \tag{B.49}$$

where the integral $F_{\rm hs}$ for a temperature independent cross-section is given by:

$$F_{\rm hs} = \frac{1}{\sqrt{\gamma}} \int_{X_F}^{\infty} dX' \frac{1}{M(X',\delta)} \Big(1 + \frac{\gamma - 1}{2} M(X',\delta)^2 \Big)^{-1/(\gamma-1)}. \tag{B.50}$$

For a particular value of X_F, equation B.49 evaluates to 1, meaning there is on average only

one collision left for the rest of the expansion. The terminal temperature and flow velocity have been reached and therefore X_F is the coordinate of the freezing surface. For some typical values for an axisymmetric supersonic expansion out of a converging nozzle with a throat of diameter $D = 0.75$ mm, an approximate helium cross-section of $\sigma = 3 \times 10^{-19}\text{m}^2$ [96] and a typical stagnation pressure of 2 bar at room temperature, iteratively solving equation B.49 places the freezing surface about 3 cm from the nozzle.
For many molecular beams, the heavier molecules are immersed in a gas of lighter atoms. This means that the molecules get accelerated to the speed of the lighter species. This is due to the fact that the molecular gas is very dilute meaning that the average mass of the binary mixture approaches that of the more abundant lighter species. Looking at the spatial composition within the jet, it was shown experimentally [134], that the heavier species accumulates more in the centre of the jet. Several mechanisms can be responsible for this behaviour. As the lighter species has a higher thermal velocity, it spreads out more quickly and therefore the heavier species is naturally more confined to the centre [135]. This mechanism applies in the regime of free molecular flow. Another possibility applicable to higher Reynolds numbers is diffusive separation due to the intial pressure gradient in the expansion which draws the heavier molecules more towards the centre [136]. The next section considers the beam intensity and the use of a skimmer in more detail.

Beam intensity and introducing a skimmer in the beam line

A skimmer is a means to separate the molecules from the carrier gas and to filter out the cold, denser part of the beam. It can be introduced anywhere along the jet axis, but it should always be put into the beam before the jet equilibrates with the surrounding gas. If the background pressure is relatively high, the jet equilibrates with the background through a Mach shock (see figure B.2); otherwise it can equilibrate through scattering with the background gas. In the first case, the skimmer should be inserted into the isoentropic flow region of the zone of silence (see figure B.2). The resulting beam is very intense though poorly collimated and the speed ratio $S = \frac{u}{\sqrt{\frac{2k_BT}{m}}}$ is limited [133]. If the background pressure is low enough that there is a gradual transition from the continuous regime to the molecular free regime, the sudden freeze model can be applied to find the position of the freezing surface. The skimmer can be inserted anywhere downstream of the freezing surface, which gives a better speed ratio, better collimation and better cooling of internal degrees of freedom [133]. However this comes with the cost of a reduction in intensity.
The opening angle of a conical skimmer is a compromise between two conflicting requirements. To minimize disturbance of the jet the angle should be small, but to ensure that the gas density inside the skimmer reduces as quickly as possible with increasing distance from the skimmer entrance, the angle should be large. A trumpet shaped skimmer, where the opening angle is small at the apex and large at the tip, is a good way to satisfy both requirements. A short skimmer also helps to reduce scattering of the beam that is transmitted through.

There are several ways a skimmer can influence the jet, depending on the number density at the skimmer entrance. For a particular source this number density can be changed in two main ways: either the distance between nozzle and skimmer x_s is changed, while everything else stays the same, or n_0 is changed while the other stagnation parameters stay the same. A Knudsen number for the skimmer can be defined as $K_{ns} = \frac{\lambda_s}{D_s}$, were λ_s indicates the mean free path in front of the skimmer entrance that has diameter D_s. The effect of the skimmer then depends on the value of K_{ns} as follows:

- For very low densities, where $K_{ns} > 50$, there is quasi-free molecular flow. Although atoms scattering from the back of the skimmer can collide with incoming molecules of the jet, the frequency of these collisions is negligible. In this case the skimming is ideal.
- When K_{ns} approaches unity, the number of atoms reflected by the back surface of the skimmer becomes significant and there is scattering in front of the skimmer. In that case the skimmer is interfering with the jet.
- With a further increase in n (decrease of K_{ns}), there are still collisions between jet molecules as well as molecules reflected back from the skimmer and both contribute to the density in front of the skimmer. Therefore in this case, the flow structure shows similarities to a diffuse shock wave. This is the case, where the intensity of the beam is diminished most.

The beam intensity downstream of the skimmer will also be reduced if the relatively background pressure, is high enough to scatter jet molecules out of the beam between nozzle and skimmer entrance.

Bibliography

[1] W. Ketterle. Nobel lecture: When atoms behave as waves: Bose-Einstein condensation and the atom laser. *Reviews of Modern Physics*, **74**, 1131, (2002).

[2] J. van Veldhoven, J. K¨upper1, H.L. Bethlem, B. Sartakov, A.J.A. van Roij, and G. Meijer. Decelerated molecular beams for high-resolution spectroscopy. *The European Physical Journal D*, **31**, 337–349, (2004).

[3] H. L. Bethlem, M. Kajita, B. Sartakov, G. Meijer, and W. Ubachs. Prospects for precision measurements on ammonia molecules in a fountain. *European Physics Journal Special Topics*, **163**, 55–69, (2008).

[4] M. Kajita. Sensitive measurement of mp/me variance using vibrational transition frequencies of cold molecule. *New Journal of Physics*, **11**, 05501, (2009).

[5] J.J. Hudson, D. M. Kara, I. J. Smallman, B. E. Sauer, M. R. Tarbutt, and E. A. Hinds. Improved measurement of the shape of the electron. *Nature*, **473**, 493–496, (2011).

[6] Daussy, T. Marrel, A. Amy-Klein, C. T. Nguyen, Ch. J. Bordé, and Ch. Chardonnet†. Limit on the Parity Nonconserving Energy Difference between the Enantiomers of a Chiral Molecule by Laser Spectroscopy. *Physical Review Letters*, **83**, 1554–1557, (1999).

[7] D. DeMille, S. B. Cahn, D. Murphree, D. A. Rahmlow, and M. G. Kozlov. Using Molecules to Measure Nuclear Spin-Dependent Parity Violation. *Physical Review Letters*, **100**, 023003, (2008).

[8] J. D. Weinstein, R. deCarvalho, Guillet T, B. Friedrich, and J. M. Doyle. Magnetic trapping of calcium monohydride molecules at millikelvin temperatures. *Nature*, **395**, 148, (1998).

[9] R.deCarvalho, J.M. Doyle, B. Friedrich, T. Guillet, J. Kim, D. Patterson, and J.D. Weinstein. Buffer-gas loaded magnetic traps for atoms and molecules: A primer. *European Physical Journal D*, **7**, 289–309, (1999).

[10] T.Rieger, T. Junglen, S. A. Rangwala, P.W. H. Pinkse, and G. Rempe. Continuous Loading of an Electrostatic Trap for Polar Molecules. *Physics Review Letters*, **95**, 173002, (2005).

[11] H. L. Bethlem, G. Berden, F. M. H. Crompvoets, R. T. Jongma, A. J. A. van Rolj, and G. Meijer. Electrostatic trapping of ammonia molecules. *Nature*, **406**, 491, (2000).

[12] J. van Veldhoven, H. L. Bethlem, and G. Meijer. ac Electric Trap for Ground-State Molecules. *Physica Review Letters*, **94**, 083001, (2005).

[13] T. Rom, T. Best, O. Mandel, A. Widera, M. Greiner, T. W. Haensch, and I. Bloch. State Selective Production of Molecules in Optical Lattices. *Physics Review Letters*, **93**, 073002, (2004).

[14] D. DeMille, D. R. Glenn, and J. Petricksa. Microwave traps for cold polar molecule. *The European Physical Journal D*, **31**, 375–38, (2004).

[15] S. Y. T. van de Meerakker, N. Vanhaecke, M. P. J. van der Loo, G.C. Groenenboom, , and G. Meijer. Deceleration and Electrostatic Trapping of OH molecules. *Physical Review Letters*, **94**, 023004, (2005).

[16] W. C. Campbell, L. W. Buxton, T. J. Balle, M. R. Keenan, and W. H. Flygare. Time-Domain Measurement of Spontaneous Vibrational Decay of Magnetically Trapped NH. *Physical Review Letters*, **100**, 083003, (2008).

[17] S. K. Tokunaga, W. Skomorowski, P. S. Zuchowski, R. Moszynski, J. M. Hutson, E. A. Hinds, and M. R. Tarbutt. Prospects for sympathetic cooling of molecules in electrostatic, ac and microwave traps. *The European Physical Journal D*, **DOI: 10.1140/epjd/e2011-10719-x**, (2011).

[18] M.T. Hummon, W. C. Campbell, H. Lu, E. Tsikata, and Y. Wang adn J. M. Doyle. Magnetic trapping of atomic nitrogen (^{1}4N) and cotrapping of NH ($X^3\Sigma^-$). *Physical Review A.*, **78**, 050702, (2008).

[19] A. V. Avdeenkov. Collisions of bosonic ultracold polar molecules in microwave trap. *New Journal of Physics*, **11**, 055016, (2009).

[20] P. Soldan and J. M. Hutson. Interaction of NH X $3^{\Sigma}-$ Molecules with Rubidium Atoms: Implications for Sympathetic Cooling and the Formation of Extremely Polar Molecules. *Physical Review Letters*, **92**, 163202, (2004).

[21] R. V. Krems. Cold controlled chemistry. *Physical Chemistry Chemical Physics*, **10**, 4079–4092, (2008).

[22] L. Santos, G.V. Shlyapnikov, P. Zoller, and M. Lewenstein. Bose-Einstein Condensation in Trapped Dipolar Gases. *Physical Review Letters*, **28**, 1791, (2000).

[23] M. Baranov, L. Dobrek, K. Goral, L. Santos, and M. Lewenstein. Ultracold dipolar gases- a challenge for experiments and theory. *Physics Scripta T.*, **102**, 74–81, (2002).

[24] D. DeMille. Quantum Computation with Trapped Polar Molecules. *Physical Review Letters*, **88**, 067901, (2002).

[25] A. Andre, D. Demille, J. M. Doyle, M. D. Lukin, S. E. Maxwell, P. Rabl, R. J. Schoelkopf, and P. Zoller. A coherent all-electrical interface between polar molecules and mesoscopic superconducting resonators. *Nature Physics*, **2**, 636, (2006).

[26] B. Friedrich R. V. Krems, W. C. Stwalley (editor). *Cold Molecules- Theory, Experiment, Applications*. CRC Press, 2009.

[27] L. D. Carr, D. DeMille, R. V. Krems, and J. Ye. Cold and ultracold molecules:science, technology and applications. *New Journal of Physics*, **11**, 055049, (2009).

[28] F. Masnou-Seeuws and P.Pillet. Formation of ultracold molecules (T<=200 [mu]K) via photoassociation in a gas of laser-cooled atoms. *Advances In Atomic, Molecular, and Optical Physics*, **47**, 53 – 127, (2001).

[29] D. Kleppner. Professor Feshbach and his resonance. *Physics Today*, (2004).

[30] E. Donley, N. R. Claussen, S. T. Thompson, and C. E. Wieman. Atom–molecule coherence in a Bose–Einstein condensate. *Nature*, **417**, 529–533, (2002).

[31] M. Greiner, C. A. Regal, and D. S. Jin. Emergence of a molecular Bose–Einstein condensate from a Fermi gas. *Nature*, **426**, 537–540, (2003).

[32] S. Jochim, M. Bartenstein, A. Altmeyer, G. Hendl, S. Riedl C. Chin, J. Hecker Denschlag, and R. Grimm. Bose-Einstein Condensation of Molecules. *Science*, **302**, 2101–2103, (2003).

[33] M. W. Zwierlein, C. A. Stan, C. H. Schmuck, S. M. F. Raupach, S. Gupta, Z. Hadzibabic, and W. Ketterle. Observation of Bose-Einstein Condensation of Molecules. *Physics Review Letters*, **91**, 250401, (2003).

[34] J. M. Sage, S. Sainis, T. Bergeman, and D. DeMille. Optical Production of Ultracold Polar Molecules. *Physical Review Letters*, **94**, 203001, (2005).

[35] S. Ospelkaus, A. Peer, K. K. Ni, J. J. Zirbel, B. Neyenhuis, S. Kotochigova, P. S. Julienne, J. Ye, and D. S. Jin. Efficient state transfer in an ultracold dense gas of heteronuclear molecules. *Nature Physics*, **4**, 622, (2008).

[36] J. G. Danzl, E. Haller, M. Gustavsson, M. J. Mark, R. Hart, N. Bouloufa, O. Dulieu, H. Ritsch, and H. C. Naegerl. Quantum Gas of Deeply Bound Ground State Molecules. *Science*, **321**, 1062, (2008).

[37] D. Egorov, T. Lahaya, W. Schoellkopf, B. Friedrich, and J. M. Doyle. Buffer-gas cooling of atomic and molecular beams. *Physical Review A*, **66**, 043401, (2002).

[38] C. I. Hancox, S. C. Doret, M. T. Hummon, L. Luo, and J. M. Doyle. Magnetic trapping of rare-earth atoms at millikelvin temperature. *Nature*, **431**, 281, (2004).

[39] J. G. E. Harris, W.C. Campbell, D. Egorov, S. E. Maxwell, R.A. Michniak, S.V. Nguyen, L.D. van Buuren, and J.M. Doyle. Buffer gas cooling and trapping of atoms with small effective magnetic moment. *Europhysics Letters*, **67**, 198–20, (2004).

[40] H. L. Bethlem. Decelerating Neutral Dipole Molecules. *Physicsal Review Letters*, **83**, 1558, (1999).

[41] B. C. Sawyer. Molecular Beam Collisions with a Magneticalle Trapped Target. *Physical Review Letters*, **101**, 203203, (2008).

[42] Y. Yamakita, S. R. Procter, A. L. Goodgame, and T. P. Softley. Deflection and deceleration of hydrogen Rydberg molecules in inhomogeneous electric fields. *Journal of Chemical Physics*, **121**, 1419, (2004).

[43] E. Narevicius, S T. Bannerman, and M. G Raizen. Towards magnetic slowing of atoms and molecules. *New Journal of Physics*, **96**, 1367–263, (2007).

[44] B. Friedrich. Slowing of supersonically cooled atoms and molecules by time-varying nonresonant induced dipole forces. *Physical Review A.*, **61**, 025403, (2000).

[45] G. Dong, W. Lu, and P. F. Barker. Decelerating and bunching molecules with pulsed traveling optical lattices. *Physical Review A.*, **69**, 013409, (2004).

[46] R. Fulton, A. I. Bishop, M. N. Schneider, and P. F. Barker. Optical Stark deceleration of nitric oxide and benzene molecules using optical lattices. *Journal of Physics B: Atomic, Molecular and Optical Physics*, **39**, S1097–S1109, (2006).

[47] A. I. Bishop, L. Wang, and P. F. Barker. Creating cold stationary molecular gases by optical Stark deceleration. *New Journal of Physics*, **12**, 073028, (2010).

[48] Manish Gupta and Dudley Herschbach. Slowing and Speeding Molecular Beams by Means of a Rapidly Rotating Source. *The Journal of Physcial Chemistry A*, **105**, 1626 – 1637, (2001).

[49] M. S. Elioff, J. J. Valentini, and D. W. Chandler. Subkelvin Cooling NO Molecules via "Billiard-like" Collisions with Argon. *Science*, **302**, 1940, (2003).

[50] T. Junglen, T. Rieger, S.A. Rangwala, P.W.H. Pinksea, and G. Rempe. Slow ammonia molecules in an electrostatic quadrupole guid. *The European Physics Journal D*, **31**, 365–37, (2004).

[51] M. D. Di Rosa. Laser-cooling molecules. *The European Physical Journal D*, **31**, 395–402, (2004).

[52] E. S. Schuman, J. F. Barry, and D. DeMille. Laser cooling of a diatomic molecule. *Nature*, **467**, 820, (2010).

[53] W. Gerlach and O. Stern. Der experimentelle Nachweis der Richtungsquantelung im Magnetfeld. *Zeitschirft fuer Physik A*, **9**, 349–352, (1922).

[54] F. Knauer. Geschwindigkeitsanalyse eines Molekularstrahles durch Laufzeitmessung. *Zeitschrift fiir Physik*, **126**, 319–335, (1949).

[55] R. D. Swenumson and U. Even. Continuous flow reflux oven as the source of an effusive molecular Cs beam. *The Review of Scientific Instruments*, **52**, 4, (1981).

[56] G Scoles et al. *Atomic and Molecular Beam Methods (Volume I)*. Oxford University Press, 1988.

[57] A. Kantrowitz and J. Grey. A High Intensity Source for the Molecular Beam. Part I. Theoretical. *Review of Scientific Instruments*, **22**, 329, (1951).

[58] G. B. Kistiakowsky and W. P. Slichter. A high intensity source for the molecular beam. Part II. Experimental. *The Review of Scientific Instruments*, **22**, 333, (1951).

[59] E. W. Becker, K. Bier, and und W. Henkes. Strahlen aus kondensierten Atomen und Molekuelen im Hochvakuum. *Zeitschrift fiir Physik*, **146**, 333–338, (1956).

[60] J. Deckers and J. B. Fenn. High intensity molecular beam apparatus. *The Review of Scientific Instruments*, **34**, 96, (1963).

[61] B. Gorowitz, K. Moses, and P. Gloersen. Magnetically Driven Fast-Acting Valve for Gas Injection into High Vacua. *The Review of Scientific Instruments*, **31**, 146, (1960).

[62] D. M. Wetstone. Fast-Acting Gas Valve. *The Review of Scientific Instruments*, **32**, 1209, (1961).

[63] E. L. Leasure, C. R. Mueller, and T. Y. Ridley. "Hot," metastable atom, molecular beam source. *The Review of Scientific Instruments*, **46**, 635, (1975).

[64] J. Q. Searcy. A supersonic molecular beam metastable atom source initiated by direct discharge. *The Review of Scientific Instruments*, **45**, 589, (1974).

[65] R. A. Larsen, S. K. Neoh, and D. R. Herschbach. Seeded supersonic alkali atom beams. *The Review of Scientific Instruments*, **45**, 1511, (1974).

[66] L. Bewig, U. Buck, Ch. Mehlmann, and M. Winter. Seeded supersonic alkali cluster beam source with refilling system. *The Review of Scientific Instruments*, **63**, 3936, (1992).

[67] J. J. Valentini, M. J. Coggiola, and Y. T. Lee. Supersonic atomic and molecular halogen nozzle beam source. *The Review of Scientific Instruments*, **48**, 58, (1977).

[68] R. W. Bickes, Jr. K. R. Newton, J. M. Herrmann, and R. B. Bernstein. Utilization of an arc-heated jet for production of supersonic seeded beams of atomic nitrogen. *The Journal of Chemical Physics*, **64**, 3648, (1976).

[69] J. A. Silver, A. Freedman, and C. E. Kolb. Supersonic nozzle beam source of atomic oxygen produced by electric discharge heating. *The Review of Scientific Instruments*, **53**, 1714, (1982).

[70] L. Li and D. M. Lubman. Pulsed laser desorption method for volatilizing thermally labile molecules for supersonic jet spectroscopy. *The Review of Scientific Instruments*, **59**, 557–561, (1988).

[71] M.R. Tarbutt, J. J. Hudson, B. E. Sauer, E A. Hinds, V. A. Ryzhov, V. L. Ryabov, and V. F. Ezhov. A jet beam source of cold YbF radicals. *Journal of Physics B: Atomic, Molecular and Optical Physics*, **35**, 5013, (2002).

[72] S. M. Skoff, R J Hendricks, C D J Sinclair, M R Tarbutt, J J Hudson, D M Segal, B E Sauer, and E A Hinds. Doppler-free laser spectroscopy of buffer-gas-cooled molecular radicals. *New Journal of Physics*, **11**, 12302, (2009).

[73] K. Kern, R. David, and G. Comsa. Low-energy helium nozzle beam. *The Review of Scientific Instruments*, **56**, 369, (1985).

[74] A. Auerbach and R. McDiarmid. Modified pulsed valve for supersonic jet applications. *The Review of Scientific Instruments*, **51**, 1273, (1980).

[75] J. P. Bucher, D. C Douglas, P. Xia, and L. A. Bloomfield. A pulsed supersonic expansion with a source temperature below 100 K. *The Review of Scientific Instruments*, **61**, 2374, (1990).

[76] S.E. Maxwell, N. Brahms, R. deCarvalho, D. R. Glenn, J. S. Helton, S.V. Nguyen, D. Patterson, J. Petricka, D. DeMille, and J. M. Doyle. High-Flux Beam Source for Cold, Slow Atoms or Molecules. *Physics Review Letters*, **95**, 173201, (2005).

[77] D. Patterson and J. M. Doyle. Bright, guided molecular beam with hydrodynamic enhancement. *The Journal of Chemical Physics*, **126**, 154307, (2007).

[78] H. Lu, J. Rasmussen, M. J. Wright, D. Patterson, and J. M. Doyle. Cold and Slow Molecular Beam. *arXiv:1104.3901v1*, (2011).

[79] L. D. Buuren, C. Sommer, M. Motsch, S. Pohle, M. Schenk, J. Bayerl, et al. Electrostatic Extraction of Cold Molecules from a Cryogenic Reservoir. *Physical Review Letters*, **102**, 033001, (2009).

[80] D. Patterson, J. Rasmussen, and J. M. Doyle. Intense atomic and molecular beams via neon buffer-gas cooling. *New Journal of Physics*, **11**, 055018, (2009).

[81] N. R. Hutzler, M. Parsons, Y. V. Gurevich, P. W. Hess, E. Petrik B. Spaun, A.C. Vutha, D. DeMille, G. Gabrielse, and John M. Doyle. A cryogenic beam of refractory, chemically reactive molecules with expansion cooling. *arXiv:1101.4217v1*, (2011).

[82] D. Patterson, E. Tsikata, and J. M. Doyle. Cooling and collisions of large gas phase molecules. *Physical Chemistry Chemical Physics*, **12**, 9736–9741, (2010).

[83] G Miller and Jr. R. L. Buice. On the Knudsen Limiting Law of Thermal Transpiration. *The Journal of Physical Chemistry*, **70**, 3874–3880, (1996).

[84] T. R. Roberts and S.G. Sydoriak. Thermomolecular pressure ratios for He^3 and He^4. *Physical Review*, **102**, 304–308, (1956).

[85] T Takaishi and Y. Sensui. Thermal Transpiration Effect of Hydrogen, Rare gases and Methane. *Transactions of the Faraday Society*, **59**, 2503–2514, (1963).

[86] D L Clark, M. E. Cage, D. A. Lewis, and G. W. Greenlees. Optical isotopic shifts and hyperfine splittings in Yb. *Physical Review A.*, **20**, 239–253, (1979).

[87] J. Wang. Laser andd Radiofrequency spectroscopy of Ytterbium Fluoride Ground State. *PhD Thesis, Yale University*, (1996).

[88] B.E. Sauer, J. Wang, and E. A. Hinds. Laser-rf double resonance spectroscopy of ^{174}YbF in the X^{2}Sigma $^+$state: Spin-rotation, hyperfine interactions. *The Journal of Chemical Physics*, **105**, 7412–7420, (1996).

[89] K.L. Dunfield, C. Linton, T. E. Clarke, J. McBride, A. G Adam, and J. R. D. Peerst. Laser Spectroscopy of the Lanthanide Monofluorides: Analysis of the A$^2\Pi$–X $^2\Sigma$ Transition of Ytterbium Monofluorid. *Journal of Molecular Spectroscopy*, **174**, 433–445, (1995).

[90] T.C. Steimle and T. Ma. The hyperfine interaction in the $A^2\Pi_{1/2}$ and $X^2\Sigma^+$ states of ytterbium monofluoride. *The Journal of Chemical Physics*, **127**, 23431, (2007).

[91] R. Loudon. *The quantum theory of light.* Oxford University Press, third edition, 2003.

[92] C.J. Foot. *Atomic Physics.* Oxford University Press, first edition, 2005.

[93] X. Zhuang, A. Le, T. C. Steimle, N. E. Bulleid, I. J. Smallman, R. J. Hendricks, S. M. Skoff, J. J. Hudson, B. E. Sauer, E. A. Hinds, and M. R. Tarbutt. Franck-Condon Factors and Radiative Lifetime of the $A^2\Pi_{1/2}$ - $X^2\Sigma$+ Transition of Ytterbium Monoflouride, YbF. *Physical Chemistry Chemical Physics*, **DOI: 10.1039/C1CP21585J**, (2011).

[94] S. M. Skoff, R. J. Hendricks, C. D. J. Sinclair, J. J. Hudson, D. M. Segal, B. E. Sauer, E. A. Hinds, and M. R. Tarbutt. Diffusion, thermalization, and optical pumping of YbF molecules in a cold buffer-gas cell. *Physical Review A*, **83**, 023418, (2011).

[95] B.E. Sauer, J. Wang, and E. A. Hinds. Anomalous spin-rotation coupling in the X^2Sigma $^+$state of YbF. *Physical Review Letters*, **74**, 1554–1557, (1995).

[96] Hasted. *Physics of Atomic Collisions*. Butterworths, second edition, 1972.

[97] SG Redsun and RJ Knize. Measurement of atomic-hydrogen diffusion in helium. *Physical Review A*, **37**, 737, (1988).

[98] RF Barrow and AH Chojniki. Analysis of the optical spectrum of gaseous ytterbium monofluoride. *Journal of the Chemical Society, Faraday Transactions 2*, **71**, 728–735, (1975).

[99] GA Bird. *Molecular Gas Dynamics and the Direct Simulation of Gas Flows*. Oxford Science Publications, third edition, 1998.

[100] S Chapman. The Kinetic Theory of Simple and Composite Monoatomic Gases: Viscosity, Thermal Conduction, and Diffusion. *Proceedings of the Royal Society of London*, **93**, 1–20, (1916).

[101] EA Mason and TR Marrero. The Diffusion of Atoms and Molecules. *Advances in Atomic and Molecular Physics*, **6**, 155–232, (1970).

[102] R.C. Reid, J.M. Prausnitz, and B.E. Poling. *The Properties of Gases and Liquids*. Mc Graw-Hill, fourth edition, 1986.

[103] E Czuchaj, F. Rebentrost, H. Stoll, and H. Preuss. Pseudopotential calculations for the potential energies of LiHe and BaHe. *Chemical Physics*, **196**, 37–64, (1995).

[104] SH Patil. Adiabatic potentials for alkali-inert gas systems in the ground state. *The Journal of Chemical Physics*, **94**, 8089–8095, (1991).

[105] W. A. Hamel, J. E. M. Haverkort, H. G. C. Werij, and J P Woerdman. Calculation of alkali-noble gas diffusion cross sections relevant to light induced drift. *Journal of Physics B*, **19**, 4127–4135, (1986).

[106] TV Tscherbul, J. Klos, L. Rajchel, and R. V. Krems. Fine and hyperfine interactions in cold YbF-He collisions in electromagnetic fields. *Physical Review A*, **75**, 033416, (2007).

[107] H.D. Baehr and K. Stephan. *Heat and Mass Transfer*. Springer, translated from second edition edition, 1998.

[108] N. B. Vargaftik and L. V. Yakush. Temperature Dependence of thermal conductivity of helium. *Zhurnal*, **32**, 822–824, (1977).

[109] JF Barry, E.S. Shuman, and D. DeMille. A Bright, Slow Cryogenic Molecular Beam Source for Free Radicals. *arXiv:1101.4229v1*, (2011).

[110] AO Sushkov and D. Budker. Production of long-lived atomic vapor inside high-density buffer gas. *Physical Review A*, **77**, 042707, (2008).

[111] D Egorov, W.C. Campbell, B. Friedricha, S.E. Maxwell, E. Tsikata, L.D. van Buuren, and J.M. Doyleb. Buffer-gas cooling of NH via the beam loaded buffer-gas method. *European Physical Journal D*, **31**, 307–311, (2004).

[112] MJ Lu, K. S. Hardman, and J. D. Weinstein*. Fine-structure-changing collisions in atomic titanium. *Physical Review A*, **77**, 060701, (1970).

[113] MJ Lu and J. D. Weinstein. Cold TiO(X $^3\Delta$)–He collisions. *New Journal of Physics*, **11**, 055015, (2009).

[114] A Briggs. Characterization of some chip resistors at low temperatures. *Cryogenics*, **31**, 932–935, (1991).

[115] F Pobell. *Matter and methods at low temperatures*. Springer, third edition, 2007.

[116] CC Lim. Indium seals for low-temperature and moderate-pressure applications. *Review of Scientific Instruments*, **57**, 114, (1986).

[117] PN Butcher and D Cotter. *The Elements of Nonlinear Optics*. Cambridge University Press, first edition, 1990.

[118] D.M. Kara. Toward an electron electric dipole moment measurement using Ytterbium Fluoride. *PhD Thesis, Imperial College London*, (2010).

[119] TW Hansch and B Couillaud. Laser frequency stabilization by polarization spectroscopy of a reflecting reference cavity. *Optics Communications*, **35**, 441–444, (1980).

[120] C. Sommer, L. D. van Buuren, M. Motsch, S. Pohle, J. Bayerl, P. W. H. Pinkse, and G. Rempe. Continuous guided beams of slow and internally cold polar molecules. *Faraday Discuss.*, **142**, 203–220, (2009).

[121] J. D. Weinstein, K. Amar R. deCarvalho, B. C. Odom A. Boca, B. Friedrich, and J. M. Doyle. Spectroscopy of buffer-gas cooled vanadium monoxide in a magnetic trapping field. *The Journal of Chemical Physics*, **109**, 2656, (1998).

[122] R.A. Smith, T. Ditmire, and J. W. G. Tisch. Characterization of a cryogenically cooled high-pressure gas jet for laser/cluster interaction experiments. *The Review of Scientific Instruments*, **69**, 3798–3804, (1998).

[123] V. Ghazarian, J. Eloranta, and V. A. Apkarian. Universal molecule injector in liquid helium: Pulsed cryogenic doped helium droplet source. *The Review of Scientific Instruments*, **73**, 3606–3613, (2002).

[124] J. Wormer, V. Guzielski, J. Stapelfeldt, and T. Moeller. Fluorescence excitation spectroscopy of xenon clusters in the VUV. *Chemical Physics Letters*, **159**, 321–326, (1989).

[125] O.F. Hagena. Condensation in Free Jets: Comparison of Rare Gases and Metals. *Zeitschrift fuer Physik D*, **4**, 291–299, (1987).

[126] O.F. Hagena and W.Obert. Cluster Formation in Expanding Supersonic Jets: Effect of Pressure, Temperature, Nozzle Size, and Test Gas. *Chemical Physics Letters*, **56**, 1793, (1972).

[127] J. Kim, B. Friedrich, D.P. Katz, D. Patterson, J. D. Weinstein, R. DeCarvalho, and J. M. Doyle. Buffer-Gas Loading and Magnetic Trapping of Atomic Europium. *Physical Review Letters*, **78**, 3665, (1997).

[128] J. J. Tollett, C. C. Bradley, C. A. Sackett, and R. G. Hulet. Permanent magnetic trap for cold atoms. *Physical Review A*, **51**, 22, (1995).

[129] S. E. Maxwell. *Buffer gas cooled atoms and molecules: production, collisional studies, and applications*. PhD thesis, Harvard University, 2007.

[130] J. Brown and A. Carrington. *Rotational Spectroscopy of diatomic molecules*. Cambridge, first edition, 2003.

[131] P. Clausing. Eine Bemerkung zur Molekularstroemung. *Annalen der Physik*, **406**, 129–133, (1932).

[132] H Pauly. *Atom, Molecule and Cluster Beams I*. Springer, 2000.

[133] G Sanna and G Tomassetti. *Introduction to Molecular Beams Gas Dynamics*. Imperial College Press, first edition, 2005.

[134] J. B. Anderson. Separation of Gas Mixtures in Free Jets. *AIChE*, **13**, 1188, (1976).

[135] H. Dun, B. L. Mattes, and D. A. Stevenson. The Gas Dynamics of conical nozzle molecular beam sampling system. *Chemical Physics*, **38**, 161–172, (1979).

[136] J. B. Anderson. Separation of Gas Mixtures. *AIChE*, **13**, 1188, (1967).

List of Figures

2.1 Sketch of HD3 cryostat (dimensions are given in mm) 17
2.2 Buffer gas cell 18
2.3 Sketch of the gas handling system (not to scale) 19
2.4 Pressure (in mbar) measured at the cell versus pressure measured at the inlet tube,blue: pumped on cell over night, red: during ablation, black: pressure settled after ablation, errors are expected to be 0.5% of the reading 20
2.5 Pressure (P_2[mbar]) inside the cell(T_2=10K) as a function of input pressure (P_1[mbar], T_2=295K) for hydrodynamic regime ($P_1 \approx P_2$), intermediate regime (eqn. 2.4) and Knudsen regime(eqn. 2.2)(reservoirs are connected via 2.5 mm diameter tube) 21
2.6 Schematic of the experimental set-up 23
2.7 Spectrum of the $^1S_0 \rightarrow ^3P_1$ transition in Yb used to measure the fsr of the long Fabry-Perot cavity. The different lines correspond to different isotopes of Yb as indicated. Multiple hyperfine-split lines exist for the odd isotopes. 25

3.1 Allowed rotational transitions between the $X^2\Sigma+$ and $A^2\Pi_{1/2}$ states in YbF(left) and the hyperfine splitting of the Q-branch (right). 28
3.2 Fractional absorption signal of YbF molecules in a buffer gas cell as a function of time 33
3.3 Doppler limited (top) and doppler free spectrum (bottom) of the Q(13) transition showing the three most abundant isotopes and the four hyperfine components 34
3.4 Saturated absorption spectra recorded with a buffer gas cell temperature of 80 K (upper trace) and 10 K (lower trace) 35
3.5 Measured frequency intervals of several $Q(N)$ transitions with fits to the eigenvalues of the effective Hamiltonian 3.7 36
3.6 Fractional absorption A as a function of intensity at centre of probe beam for three different values of helium buffer gas density, given in atoms per m^3 40
3.7 Saturation intensity I'_s as a function of helium buffer gas number density in the cell 41
3.8 Ablation yield as a function of number of ablation shots, normalised to the highest yield in that scan 42

4.1 Elastic scattering problem of two particles simplified to the centre of mass frame and one particle of reduced mass that is deflected from a fixed scattering centre (after [99]) 48
4.2 The cosine of the scattering angle χ as a function of impact parameter b in units of Bohr radii for Li-He collisions(full red line:293 K, dashed blue line:20 K) 50
4.3 Potential energy curve for an angle Θ of 0°(black) and 180°(blue,dashed) . . 52
4.4 Laser absorption profiles as a function of time for both lithium (red) and YbF(blue) for helium density of $2.2 \times 10^{22}\mathrm{m}^{-3}$ and a cell temperature of 293K 53
4.5 Measured diffusion time constants versus buffer gas density for Li(open circles) and YbF(full circles) at 293 K, 80 K, 20 K 55
4.6 Absorption images as a function of time after the ablation pulse for three different buffer gas densities at a cell temperature of 20K. For a helium density of $0.9 \times 10^{22}\mathrm{m}^{-3}$, the size of the observed molecular cloud is limited by the one inch diameter window used for detection. 57
4.7 Simulated diffusion images for a diffusion constant of 0.005 $\mathrm{m}^2\ \mathrm{s}^{-1}$. This corresponds to a cell temperature of 20 K, a diffusion cross-section of 80×10^{-20} m^2 and a helium density of 3×10^{22} m^{-3}. a) uniform molecule distribution at t=0. b) localised molecule distribution near the target at t=0, (the image size corresponds to the size of a one inch diameter window, as used in the experiments) 58
4.8 Variation with time of YbF density (integrated along a line through the cell) at several distances from the target. 59
4.9 Absorption spectrum of the Q(7) line obtained 200μs (red) and 2000μs(blue) after the ablation pulse (above) fitted to Voigt profiles and a saturated absorption spectrum recorded simultaneously showing its hyperfine components (below).The cell temperature is approximately 20K 62
4.10 Relative populations of Q-branch transitions from different rotational levels N at 400μs after ablation (filled points) and 2000μs after ablation(open points) fitted to Boltzmann distributions with the rotational temperature as a free parameter. The cell temperature is approximately 20K and a helium density of $0.9 \times 10^{22}\mathrm{m}^{-3}$ is used 63
4.11 Translational (blue squares) and rotational (red circles) temperature versus time after the ablation pulse for a buffer gas density of $0.9 \times 10^{22}\mathrm{m}^{-3}$ and a cell temperature of 20 K as measured with thermometers on the cold plate . 64
4.12 Population in rotational levels N=3-6 as a function of time [in ms] normalised to the population in these levels at t=0 considering rotational cooling and diffusion through the buffer gas. The three fits are single exponential decays starting 0.5 ms(red,dotted), 1 ms(green,dashed) and 2 ms(black, through line) after the ablation pulse 67

5.1 Picture of the molecular beam apparatus, indicating some of the important components . . . 71
5.2 Buffer gas cell with different cell apertures and different positions of helium inlet tube are indicated. . . . 72
5.3 Schematic set-up of periodically poled doubling crystal . . . 77
5.4 Schematic of second experimental set-up . . . 80
5.5 Picture showing buffer gas cell with positions of laser absorption and laser induced fluorescence beams indicated . . . 81

6.1 Estimated average number density in the cell by assuming an effusive (red, dotted) and maximum hydrodynamic (blue) flow rate out of a slit aperture. Measured datapoints (blue) using a pirani gauge at room temperature to measure the cell pressure agree well with estimated number densities. . . . 84
6.2 Knudsen and Reynolds numbers (at the throat) for typical helium flows used in the experiment and the slit aperture, assuming an effusive (red,dotted) and maxmimum hydrodynamic (blue) flowrate . . . 84
6.3 Typical LIF signal on pmt 23mm from the cell aperture . . . 87
6.4 Comparison of molecular signals as a function of time after the ablation pulse for different cell configurations . . . 88
6.5 Molecular beam flux as a function of helium flow, using the buffer gas cell with the s1 aperture.(The Reynolds number for the s1 cell configuration lies in the range of $(2.8 - 5.1)\times$F[sccm], depending on the flow regime.) . . . 89
6.6 Absorption images of the cell with a helium inlet at the bottom and a slit aperture on the top for two different helium flows. The size of the images corresponds to the one inch diameter window, through which the molecules are detected. . . . 90
6.7 LID Spectra of the Q(2) transition in YbF obtained by using a probe laser perpendicular (full circles, fitted to two Lorentzians) and counterpropagating (open circles, fitted to Gaussians) to the molecular beam . . . 91
6.8 . . . 92
6.9 LIF Spectrum of the Q(2) transition, taken with a laser beam counterpropagating to the molecular beam. The black line shows a fit to a Voigt profile, which yields a longitudinal temperature of 5.6 K . . . 93
6.10 LIF spectrum of YbF at 4K close to the $X^2\Sigma^+ \rightarrow A^2\Pi_{1/2}$ (0-0) bandhead, obtained using the cell in configuration s1. The probe laser is perpendicular to eh molecular beam. The labelling identifies the rotational lines and isotopes. 93
6.11 Populations in different rotational levels obtained from the LIF spectrum in shown in figure 6.10, fitted to a Boltzmann distribution . . . 94
6.12 LIF signal (black points) of YbF versus time measured at the lower detector and rotational temperature versus time (red points) for (a)configuration s1 and (b)configuration s2 . . . 95

6.13 Fraction of molecules in state 1, after pump beam has been used, as a function of helium flow. The black line is a fit to the data using equation 6.7 97
6.14 Average helium number density 82 mm from the cell aperture as a function of helium flow into the cell, estimated from optical pumping measurments (full line). This result is compared to the theoretical centerline number density at the same position estimated from the helium flow (dashed line) . 98
6.15 Ratio of molecular flux measured at lower and upper detector (a) without and (b) with a skimmer situated between the two detectors.(The Reynolds number for the s1 cell configuration lies in the range of $(2.8-5.1)\times$F[sccm], depending on the flow regime.) 99
6.16 Schematic figure of buffer gas cell with pulsed helium flow 100
6.17 Number of helium atoms versus voltage applied to solenoid valve for a 200 μs pulse 101
6.18 LIF signal over time using the buffer gas cell with pulsed helium, using a pulse length of 200 μs and opening the valve 812 μs before firing the ablation laser 101
6.19 Molecular fluorescence signal over time for different valve opening times measured on the lower detector. 102
6.20 Normalised molecular flux (dashed line) as well as forward velocity (data-points) as a function of valve opening time with respect to the Q-switch (t=0) 103
6.21 Shortest molecular pulses are achieved with the buffer gas cell if the helium line comes in at the bottom (blue, circles) or the open pulsed set-up (red, square) 105

7.1 Picture of (a) magnetic octupole guide built from 8 NdFeBr magnets with a remanence field of 1.2T and (b) its calculated magnetic field in radial direction 112

A.1 Linestrengths for the Q_{11}, ${}^{Q}R_{12}$, ${}^{O}P_{12}$ rotational transitions as a function of rotational number N 116

B.1 Relation between nozzle cross-section A normalised to the critical value A^*, and the Mach number M. 124
B.2 Shock structure of an underexpanded jet, showing the Mach disk, barrel shock and zone of silence 126
B.3 Mach number and density as a function of reduced distance from the nozzle for an axisymmetric (black) and a planar(blue, dashed) supersonic expansion 129

List of Tables

4.1 Results for fitting translational and rotational temperatures as a function of time using eqn. 4.33 with eqn. 4.32 64
4.2 Results for fitting translational as well as rotational temperature as a function of time using eqn 4.34 66
4.3 Comparison of theoretical and experimental results for diffusion cross-sections for Li and YbF and diffusion time constants for Li 69

6.1 Maximum flux of molecules for different cell apertures in the lowest rotational state (N=0) 88
6.2 Results for rotational temperature of the molecular beam for different cell apertures and positions of the helium inlet tube 94

B.1 Coefficients from MOC calculations to describe the variation of Mach number with distance from the nozzle exit 128